

UNIVERSITY OF TURIN

MASTER THESIS

NUCLEAR AND SUBNUCLEAR PHYSICS

Search for $Y(10753) \rightarrow \pi\pi h_b(1P)$ at
Belle II

Author:

F. TESTA

Supervisors:

Prof. S. SPATARO

Dr. U. TAMPONI

Contents

1	Introduction	3
1.1	Physical picture	3
	Quarkonium spectrum	5
	Quarkonium Production at e^+e^- colliders	8
1.2	Theoretical models	10
	1.2.1 Potential Model	10
	1.2.2 Lattice QCD	11
	1.2.3 Non Relativistic Effective Field Theory	12
	1.2.4 Exotic states	12
1.3	$Z_b^\pm(10610)$ and $Z_b^\pm(10650)$ at Belle	14
	Interpretation of the Z_b states	16
1.4	Y(10753)	17
2	The Belle II Experiment	23
2.1	The SuperKEKB facility	23
2.2	The Belle II detector	25
	2.2.1 Vertex Detector (VXD)	26
	2.2.2 Central Drift Chamber (CDC))	27
	2.2.3 PID systems: ARICH and TOP	28
	2.2.4 Electromagnetic Calorimeter (ECL)	30
	2.2.5 K_L - Muon detector (KLM)	31
	2.2.6 Trigger system	31
2.3	Software	33
	2.3.1 basf2	33
	2.3.2 Monte Carlo simulation	34
	2.3.3 Reconstruction	35
	Clustering	35
	Tracking	36
	Particle Identification	37
3	Analysis outline	39
3.1	Monte Carlo samples	40
3.2	Selection of tracks	42
3.3	Continuum Suppression	42
3.4	Fit on signal	43
4	Studies on Monte Carlo	45
4.1	Signal shape	45
	4.1.1 Study of the signal for the phase space transition	45
	4.1.2 Study of the signal for the Z_b mediated transition	49

4.2	tracks selection	53
4.2.1	Comparison between data and MC	53
4.2.2	cuts selection	54
4.2.3	Efficiency on signal	56
5	Validation on control sample	57
5.1	Reconstruction of the D^{*+}	58
5.1.1	Analysis of $D_0 \rightarrow K\pi$ channel	59
5.1.2	Analysis the $D_0 \rightarrow K\pi\pi_0$ channel	60
5.2	Validating Efficiency	62
5.2.1	Measuring efficiency on data	63
5.2.2	Results	67
6	Efficiency as a function of p_t and $\cos\theta$	69
6.1	Efficiency estimation on generic MC	69
6.2	Weighting the candidates	72
6.2.1	Correlation on the signal	72
7	Events Kinematics and Continuum Suppression	75
7.1	Energy and Number of tracks	75
7.2	Continuum Suppression	77
7.3	Multivariate analysis with SGBDT	77
7.4	Training the BDT and applying the classifier	78
7.5	Optimizing the cut	80
8	Fitting strategy	83
9	Conclusion	91
	Bibliography	93
A	Results of the simultaneous fits for the $D_0 \rightarrow K^-\pi^+\pi^0$ channel	99
B	Results of the simultaneous fits for the $D_0 \rightarrow K^-\pi^+$ channel	107

List of Figures

1.1	Static $Q\bar{Q}$ potential as a function of $Q\bar{Q}$ distance, in comparison to typical quarkonia radii (blue arrows).	3
1.2	Feynman diagram of quarkonium annihilation from [1].	4
1.3	Spectra of charmonium (a) and bottomonium (b) states.	5
1.4	Application of the OZI rules in regard of the decay of the Φ meson; the decay into charged kaons requires a connected diagram (a), has $BR(\phi \rightarrow K^+K^-) \approx 49\%$, while the BR for the process with disconnected lines (b) has upper limits of around 6×10^{-4} [8]. . .	7
1.5	Coupling of $b\bar{b}$ states to the $B\bar{B}$ mesons loop.	7
1.6	Production of charmonium via B decays, Initial State Radiation, double charmonium production and photon-photon scattering. . .	9
1.7	Overview of the bottomonium spectrum and the involved transitions. 10	
1.8	Lattice spectra of bottomonium states below the threshold from [13], compared to experimental measurements (red lines).	12
1.9	Spectrum of the dipion recoil mass ($M_{miss}(\pi\pi)$) at the $Y(5S)$ as reported in [18].	14
1.10	Cascade decays involved in the $\Upsilon(5S)$ to the $h_b(1P)$ state.	15
1.11	Distributions of $M_{miss}(\pi\pi)$ for $h_b(1P)$ (a) and $h_b(2P)$ (b) events. Points with error bars are data, blue lines are the fit results [20]. .	16
1.12	Energy dependence of the $e^+e^- \rightarrow \pi\pi\Upsilon(nS)$ cross sections [29]. Black points with error bars are data from the energy scan, red lines are the result of the simultaneous fit to these distributions, blue dots with error bars are the cross section values estimated with ISR from $\Upsilon(10860)$	18
1.13	Fit of the $e^+e^- \rightarrow b\bar{b}$ cross section with coherent sum of continuum amplitude and three Breit-Wigner functions.	19
1.14	(a) Invariant mass of $\pi^+\pi^-J/\psi$ as measured by BaBar [31] with the peak of the $Y(4260)$; (b) $R = \sigma(e^+e^- \rightarrow hadrons)/\sigma(e^+e^- \rightarrow \mu^+\mu^-)$ from [32].	20
1.15	Normalized resonant distribution [34] for $M(\pi\pi)$ (GeV) in the $e^+e^- \rightarrow Y(10753) \rightarrow \pi\pi\Upsilon(1S)$. Colored lines are the separate contributions for the scalar $f_0(500)$ $f_0(980)$ (red line) and the tensor $f_2(1270)$ (black line) involved in the model.	21
1.16	Plot of the luminosity at each energy point of the scan of Belle II around the $Y(10753)$ (green); the blue histogram corresponds to the energy that Belle already measured.	22
2.1	Schematic view of the nanobeam scheme adopted in SuperKEKB (blue lines) in comparison with KEK (black lines).	24

2.2	Schematic view of the SuperKEKB facility. The electron and the positron beams collision point is located in the Tsukuba section, where the Belle II detector is located.	25
2.3	Belle II Top view.	26
2.4	Schematic view of the Belle II VXD.	27
2.5	Schematic view of the Belle II CDC.	28
2.6	Working principle of the ARICH detector.	29
2.7	Conceptual view of TOP counter. This is only a schematic presentation of the operation, since the TOP installed in Belle II has the photodetector in the backward region and a focusing mirror in the forward region	30
2.8	Side view of the TOP counter with the internal reflection of the Cherenkov photons visualized	30
2.9	Schematic view of the ECL detector.	31
2.10	Scheme of the Belle II L1 Trigger [43].	32
2.11	Schematic view of the processing flow in the Belle II Software. . .	34
2.12	Simple example of 2D clustering in the PXD detector.	36
2.13	Schematic representation of the track trajectory in the $x - y$ (left), $z - y$ (middle) and $z - s$ (right) projections. Dimensions are in cm. The definition of the variables is reported in the text. The radius of the track R is the inverse of the absolute value of the track curvature ω	36
3.1	Decay of the $Y(10753) \rightarrow \pi\pi h_b(1P)$	40
3.2	Topology for jet and central events.	42
4.1	Two dimensional distribution of the signal pion momenta in the laboratory frame, at different energy points.	46
4.2	Distribution of dipion momenta for events without ISR.	46
4.3	Distribution of $M_{miss}(\pi\pi)$ with the different pion pair combinations. The narrow distribution in black come from the signal events. Large distribution in gray comes from background tracks, namely from the decay of the h_b or from beam background. Blue and purple lines represent the distributions of candidates in which one of the pion comes from the signal and the other from the background.	47
4.4	Distribution of $M_{miss}(\pi\pi)$ weighted by luminosity, for each energy point. The signal peak is located at the $h_b(1P)$ mass region ($9.9 \text{ GeV}/c^2$).	48
4.5	Acceptance of the dipion from $e^+e^- \rightarrow \pi\pi h_b$ at the four energies. .	49
4.6	Decay chain of $e^+e^-(\sqrt{s} = 10805) \rightarrow \pi Z_b(10610)/(Z_b(10650)) \rightarrow \pi\pi h_b(1P)$	50
4.7	Distribution of the momentum of the signal pions from the $Z_b(10610)$ mediated transition.	51

4.8	(a) Distribution of the $M_{miss}(\pi\pi)$ for the $Z_b(10610)$ transition. (b) Distribution of the different contributions: grey distribution for both tracks coming from background, either beam background or $h_b(1P)$ decay; black line for both signal tracks correctly reconstructed; blue line for candidates with the hard pion reconstructed and the soft pion coming from background; purple line for events with soft pion correctly reconstructed and hard pion from background.	52
4.9	Distributions of dz and dr for data (black) and MC (red), normalized to one.	54
4.10	Distribution of nSVDHits for data (black) and MC(red), normalized to one.	54
4.11	Distributions of dr (a), dz (b) (both normalized to one) and $nSVDiHits$ vs p , for signal (c) and background (d) tracks.	55
5.1	Scheme of the decays used for validation of the tracks selection.	57
5.2	Distribution of the p_t from $e^+e^- \rightarrow \pi\pi h_b(1P)$ (purple) and $D^* \rightarrow \pi^+D^0$ (black and red) pions.	58
5.3	Distribution of $M(K\pi\pi)$ and $M(K\pi)$ for data and MC. MC events are scaled down by a factor of four.	59
5.4	Distribution of $M(K\pi\pi) - M(K\pi)$ for $D_0 \rightarrow K\pi$ channel for data and MC (simulated events are scaled down by a factor of four).	60
5.5	Distribution of $M(K\pi\pi)$ and $M(K\pi)$ for data and MC (scaled down by a factor of four).	61
5.6	Distribution of $M(K\pi\pi) - M(K\pi)$ for $D_0 \rightarrow K\pi\pi_0$ channel.	62
5.7	Distribution of p_t of the π from $D^{*+} \rightarrow D_0$ in the MC sample. Purple lines represent the bins used in this study.	63
5.8	Distribution of ΔM for MC $D^{*+} \rightarrow K^+\pi^+\pi^+$ signal events that pass (a) and do not pass (b) the track selection cuts in the $0.1 < p_t < 0.15$ GeV/c bin. Grey histogram represents the MC points, blue solid line is the signal fit function.	64
5.9	Distribution of ΔM for DATA events that pass (a) and do not pass (b) the track selection cuts in the $0.1 < p_t < 0.15$ GeV/c bin. Grey histogram represents the data points, green solid line is the combined fit function, blue dotted line is the signal fit function, orange dotted line is the background fit function.	66
5.10	Distributions of efficiency in MC and data vs p_t of the soft pion, for both $K^-\pi^+$ (a) and $K^-\pi^+\pi_0$ (b) channels.	67
5.11	Distribution of R as a function of pt	67
6.1	Distribution of the efficiency for positive and negative tracks, in bins of p_t and $\cos\theta$	70
6.2	Distributions of $\cos\theta$ and p_t for generic MC tracks, weighting each track to account for the efficiency of tracks selection and reconstruction	71
6.3	Ratio of efficiencies in bins of p_t of the two pion tracks.	73

7.1	Distributions of visible energy in the center of mass and number of good tracks, for data and for different MC samples.	76
7.2	Distribution of n_good_tot vs E_{vis} , where the continuous distribution refers to the data events and the black points are the MC signal events.	77
7.3	Scheme of the operation of a DT [57]: a data event, with no signal/background label, will travel the tree from top to bottom, reaching the final node. The probability of the event to be signal is given from the signal to background ratio in the node.	78
7.4	Distribution of the BDT_{prob} for the different kinds of MC events (filled), for data (red), and for signal (black).	80
7.5	Figure of merit for the cut on BDT_{prob}	81
8.1	Results of the fits on the $M_{miss}(\pi\pi)$ (GeV/c^2) in the signal region for $e^+e^- \rightarrow \pi\pi h_b(1P)$ events, for the 10657 MeV (a) and 10706 MeV (b) energy points, after applying CS and track selection cuts and weighting the events to account for efficiency of reconstruction and track selection. Points with error bars are MC events, the blue line represents the fit function.	84
8.2	Results of the fits on the $M_{miss}(\pi\pi)$ (GeV/c^2) in the signal region for $e^+e^- \rightarrow \pi\pi h_b(1P)$ events, for the 10745 MeV (a) and 10805 MeV (b) energy points, after applying CS and track selection cuts and weighting the events to account for efficiency of reconstruction and tracks selection. Points with error barr are the MC events, the blue line represents the fit function.	85
8.3	Results of the fits on the $M_{miss}(\pi\pi)$ (GeV/c^2) in the signal region for combined signal and background events, for the 10657 MeV (a) and 10706 MeV (b) energy points, after applying CS and track selection cuts and weighting the events to account for efficiency of reconstruction and tracks selection. Points with error bars are the MC events, blue line represents the fit function.	87
8.4	Results of the fits on the $M_{miss}(\pi\pi)$ (GeV/c^2) in the signal region for combined signal and background events, for the 10745 MeV (a) and 10805 MeV (b) energy points, after applying CS and track selection cuts and weighting the events to account for efficiency of reconstruction and tracks selection. Points with error bars are the MC events, blue line represents the fit function.	88
A.1	Distribution of ΔM for data events that pass (a) and do not pass (b) the track selection cuts. grey histogram represents the data points, green solid line is the combined fit function, blue dotted line s the signal fit function, orange dotted line is the background fit function. Corresponding interval of p_t is shown above the plot.	99

A.2	Parameters of function from the simultaneous fit in the ($0.1 \leq p_t < 0.15\text{GeV}/c$) bin. Functions have their parameters labelled as "pass" or "not pass" depending the data the function describes, [a, b, c, d, e] are the parameters of the "pass background function"; [ka, ki, ku, ke, ko] are the parameters of the "not pass" background function.	100
A.3	Distribution of ΔM for data events that pass (a) and do not pass (b) the track selection cuts. grey histogram represents the data points, green solid line is the combined fit function, blue dotted line s the signal fit function, orange dotted line is the background fit function. Corresponding interval of p_t is shown above the plot.	101
A.4	Parameters of function from the simultaneous fit in the ($0.15 \leq p_t < 0.2\text{GeV}/c$) bin. Functions have their parameters labelled as "pass" or "not pass" depending the data the function describes, [a, b, c, d, e] are the parameters of the "pass background function"; [ka, ki, ku, ke, ko] are the parameters of the "not pass" background function.	102
A.5	Distribution of ΔM for data events that pass (a) and do not pass (b) the track selection cuts. grey histogram represents the data points, green solid line is the combined fit function, blue dotted line s the signal fit function, orange dotted line is the background fit function. Corresponding interval of p_t is shown above the plot.	103
A.6	Parameters of function from the simultaneous fit in the ($0.2 \leq p_t < 0.25\text{GeV}/c$) bin. Functions have their parameters labelled as "pass" or "not pass" depending the data the function describes, [a, b, c, d, e] are the parameters of the "pass background function"; [ka, ki, ku, ke, ko] are the parameters of the "not pass" background function.	104
A.7	Distribution of ΔM for data events that pass (a) and do not pass (b) the track selection cuts. grey histogram represents the data points, green solid line is the combined fit function, blue dotted line s the signal fit function, orange dotted line is the background fit function. Corresponding interval of p_t is shown above the plot.	105
A.8	Parameters of function from the simultaneous fit in the ($p_t > 0.25\text{GeV}/c$) bin. Functions have their parameters labelled as "pass" or "not pass" depending the data the function describes, [a, b, c, d, e] are the parameters of the "pass background function"; [ka, ki, ku, ke, ko] are the parameters of the "not pass" background function.	106
B.1	Distribution of ΔM for data events that pass (a) and do not pass (b) the track selection cuts. grey histogram represents the data points, green solid line is the combined fit function, blue dotted line s the signal fit function, orange dotted line is the background fit function. Corresponding interval of p_t is shown above the plot.	107
B.2	Parameters of function from the simultaneous fit in the ($p_t < 0.1\text{GeV}/c$) bin. Functions have their parameters labelled as "pass" or "not pass" depending the data the function describes.	108

B.3	Distribution of ΔM for data events that pass (a) and do not pass (b) the track selection cuts. grey histogram represents the data points, green solid line is the combined fit function, blue dotted line s the signal fit function, orange dotted line is the background fit function. Corresponding interval of p_t is shown above the plot.	108
B.4	Parameters of function from the simultaneous fit in the ($0.1 \leq p_t < 0.15\text{GeV}/c$) bin. Functions have their parameters labelled as "pass" or "not pass" depending the data the function describes, [a, b, c, d, e] are the parameters of the "pass background function"; [ka, ki, ku, ke, ko] are the parameters of the "not pass" background function.	109
B.5	Distribution of ΔM for data events that pass (a) and do not pass (b) the track selection cuts. grey histogram represents the data points, green solid line is the combined fit function, blue dotted line s the signal fit function, orange dotted line is the background fit function. Corresponding interval of p_t is shown above the plot.	110
B.6	Parameters of function from the simultaneous fit in the ($0.15 \leq p_t < 0.2\text{GeV}/c$) bin. Functions have their parameters labelled as "pass" or "not pass" depending the data the function describes, [a, b, c, d, e] are the parameters of the "pass background function"; [ka, ki, ku, ke, ko] are the parameters of the "not pass" background function.	111
B.7	Distribution of ΔM for data events that pass (a) and do not pass (b) the track selection cuts. grey histogram represents the data points, green solid line is the combined fit function, blue dotted line s the signal fit function, orange dotted line is the background fit function. Corresponding interval of p_t is shown above the plot.	112
B.8	Parameters of function from the simultaneous fit in the ($0.2 \leq p_t < 0.25\text{GeV}/c$) bin. Functions have their parameters labelled as "pass" or "not pass" depending the data the function describes, [a, b, c, d, e] are the parameters of the "pass background function"; [ka, ki, ku, ke, ko] are the parameters of the "not pass" background function.	113

List of Tables

1.1	Summary of the integrated luminosity of Belle.	14
1.2	Predictions of $Y(10753)$ branching ratios under different interpretations as reported in [34][35][36][37][38][39][40]	21
3.1	Number of $e^+e^- \rightarrow \pi\pi h_b(1P)$ events produced in the signal sample, for each energy.	41
3.2	Luminosity for each process of the BG.	41
4.1	Acceptance of the dipion from $e^+e^- \rightarrow \pi\pi h_b(1P)$ at the four energies.	49
4.2	Acceptance for $e^+e^- \rightarrow \pi Z_b(10610) \rightarrow \pi\pi h_b(1P)$ at $\sqrt{s} = 10805$ MeV.	52
5.1	Fit results on both MC samples.	65
5.2	Fit results on data samples; sample parameters are different between the two sample, while common parameters are shared.	66
5.3	Values of $R = eff_{Data}/eff_{MC}$ for the different bin of p_t in $D^0 \rightarrow K^-\pi^+$ and $D^0 \rightarrow K^-\pi^+\pi_0$	68
6.1	Yields for the generated $e^+e^- \rightarrow \pi\pi h_b(1P)$ signal events (first column), and the weighted values after the reconstruction and the tracks selection.	73

Abstract

During the scan of the energies above the $\Upsilon(4S)$, the Belle experiment found a resonance structure at around 10753 MeV in the cross section of $e^+e^- \rightarrow \pi\pi\Upsilon(nS)$, with $n = 1, 2, 3$. This structure was identified as an exotic state and it was named $Y(10753)$; since it was produced directly in the e^+e^- collisions, the quantum numbers $J^{PC} = 1^{--}$ were assigned. In November 2021 Belle II took new data with increased luminosity at four energies around the $Y(10753)$, between the energy points already inspected by Belle.

In this work it is presented a blind analysis aimed to measure the $Y(10753) \rightarrow \pi\pi h_b(1P)$ cross section via the inclusive reconstruction of the $h_b(1P)$. This measurement will help to investigate the nature of the $Y(10753)$, and to study if transitions to intermediate exotic states do occur, which should lead to an increase in the production cross section. The analysis will be performed by studying the $M_{miss}(\pi\pi)$ spectrum in search of a peak in the $h_b(1P)$ mass region and measuring the yield of the signal events. The yields will be measured for four energy points (10657, 10706, 10745, 10805 MeV) to study the behaviour of the cross section around the $Y(10753)$. The tracks selection for the pion candidates have been performed by Monte Carlo simulations of $e^+e^- \rightarrow \pi\pi h_b(1P)$ and background events. The efficiency for the obtained cuts has been validated on two control channels, $D^{*+} \rightarrow \pi^+ D_0 \rightarrow \pi^+ K^- \pi^+$ and $D^{*+} \rightarrow \pi^+ D_0 \rightarrow \pi^+ K^- \pi^+ \pi_0$, with the data collected by Belle II at the four points of the scan. A strategy to correct the eventual data-simulation discrepancy for the track selection is developed, according to the values of p_t of the tracks. A multi variate analysis is performed in order to reject continuum events from $e^+e^- \rightarrow q\bar{q}$ process, using a stochastic gradient boosted decision tree (SGBDT) already trained for the $\Upsilon(4S) \rightarrow \eta h_b(1P)$ analysis.

In chapter 1 the phenomenological and theoretical aspects of the heavy quarkonium systems are discussed, alongside a presentation of some experimental results in regard of the exotic $Z_b(10610)$ and $Z_b(10650)$ charged state in the bottomonium and the $Y(10753)$ state. In chapter 2 an overview of the Belle II detector and the SuperKEKB collider is given, together with a presentation of the software for the event reconstruction and MC simulation. Chapter 3 gives an outline of the structure of the analysis, in chapter 4 the study on the MC samples is presented and the cuts for the tracks selection are reported. Chapter 5 presents the validation of the efficiency for the tracks selection on the two control channels. The strategy to correct for tracks selection and reconstruction is presented in chapter 6. Suppression of continuum events $e^+e^- \rightarrow q\bar{q}$ using a multivariate analysis is presented in chapter 7. An introductory study of the signal and background shape for the fit is presented in chapter 8. In chapter 9 a summary of the results of this analysis will be drawn.

Abstract

Durante lo scan di energie sopra la $\Upsilon(4S)$, Belle ha trovato una struttura riso-
nante nella sezione d'urto $e^+e^- \rightarrow \pi\pi\Upsilon(nS)$, con $n = 1, 2, 3$, intorno a 10753 MeV.
Questa struttura è stata identificata come uno stato esotico e chiamata $Y(10753)$;
essendo prodotta direttamente nella collisione tra e^+e^- , sono stati assegnati i nu-
meri quantici $J^{PC} = 1^{--}$. A novembre 2021 Belle II ha acquisito nuovi dati con
maggiore luminosità rispetto a Belle a quattro energie attorno alla $Y(10753)$.

In questo lavoro viene presentata una analisi con lo scopo di misurare la sezione
d'urto del processo $e^+e^- \rightarrow \pi\pi h_b(1P)$ attraverso la ricostruzione inclusiva del
mesone $h_b(1P)$. Questa misura aiuta a capire meglio la natura della $Y(10753)$,
e permette di verificare se è presente la transizione sullo stato carico intermedio
 $Z_b(10610)$ tra $Y(10753)$ e $h_b(1P)$, transizione che comporterebbe un aumento della
sezione d'urto. Questa analisi sarà effettuata attraverso lo studio dello spettro
della massa di rinculo della coppia di pioni $M_{miss}(\pi\pi)$, alla ricerca di un picco nella
regione di massa della $h_b(1P)$, allo scopo di misurare la resa del segnale. La resa
verrà misurata alle quattro energie attorno alla $Y(10753)$ (10657, 10706, 10745,
1805 MeV) con i dati presi da Belle II. La selezione delle tracce dei pioni è stata
effettuata attraverso simulazioni Monte Carlo (MC) di eventi $e^+e^- \rightarrow \pi\pi h_b(1P)$
e di eventi di fondo. L'efficienza per questi tagli è stata validata su due canali
di controllo, $D^{*+} \rightarrow \pi^+ D_0 \rightarrow \pi^+ K^- \pi^+$ and $D^{*+} \rightarrow \pi^+ D_0 \rightarrow \pi^+ K^- \pi^+ \pi_0$, con i
dati acquisiti da Belle II ai quattro punti dello scan, ed è stata sviluppata una
strategia per correggere una eventuale discrepanza tra dati e MC per la selezione
delle tracce, in base al momento trasverso di ogni traccia. È stata effettuata una
analisi multivariata allo scopo di rimuovere gli eventi di "continuo" provenienti dai
processi $e^+e^- \rightarrow q\bar{q}$, attraverso l'utilizzo del metodo "stochastic gradient boosted
decision tree" (SGBDT) già utilizzato per l'analisi del decadimento $\Upsilon(4S) \rightarrow$
 $\eta h_b(1P)$.

Nel capitolo 1 vengono discussi gli aspetti teorici e fenomenologici del quarko-
nio, insieme ad una presentazione di alcuni risultati sperimentali a riguardo degli
stati esotici carichi $Z_b(10610)$ e $Z_b(10650)$ nel bottomonio e della $Y(10753)$. Nel
capitolo 2 viene data una panoramica del rivelatore Belle II e dell'acceleratore
SuperKEKB, assieme ad una presentazione del software per la ricostruzione e la
simulazione Monte Carlo. Nel capitolo 3 viene delineata la struttura dell'analisi,
nel capitolo 4 viene presentato lo studio dei campioni MC e vengono riportati i
tagli per la selezione delle tracce. Nel capitolo 5 viene presentata la validazione
dell'efficienza per la selezione delle tracce, attraverso i due canali di controllo. La
strategia per correggere gli effetti di selezione e ricostruzione viene presentata nel
capitolo 6. Nel capitolo 7 viene presentata la rimozione degli eventi di continuo
 $e^+e^- \rightarrow q\bar{q}$ attraverso una analisi multivariata. Uno studio introduttivo del seg-
nale e del fondo è presentato nel capitolo 8, e le conclusioni vengono tratte nel
capitolo 9.

Chapter 1

Introduction

1.1 Physical picture

In high energy physics, Quarkonium is defined as the bound state of a heavy quark and its own anti-quark, usually indicated as $Q\bar{Q}$; *charm* and *beauty* quarks can give rise to quarkonium states, while *top* quarks decay weakly before a proper bound state can be formed. The Quantum Chromo Dynamics (QCD) is the theory which describe the strong interaction, thus the interaction the quarks undergo. Historically, the strong interaction between quarks in quarkonium states has been described with a potential model (see Fig. 1.1); nowadays, thanks to the advances in Lattice QCD and non relativistic effective field theory (NR EFT), theoretical and phenomenological models reached new levels of predictivity. Hence, the study of quarkonium continues to be relevant thanks to the discoveries of new states, measurements of new processes and increased statistics accumulated in various experiments.

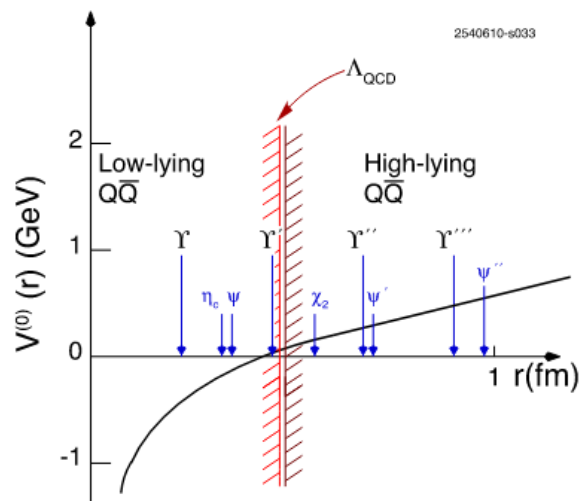


Figure 1.1: Static $Q\bar{Q}$ potential as a function of $Q\bar{Q}$ distance, in comparison to typical quarkonia radii (blue arrows).

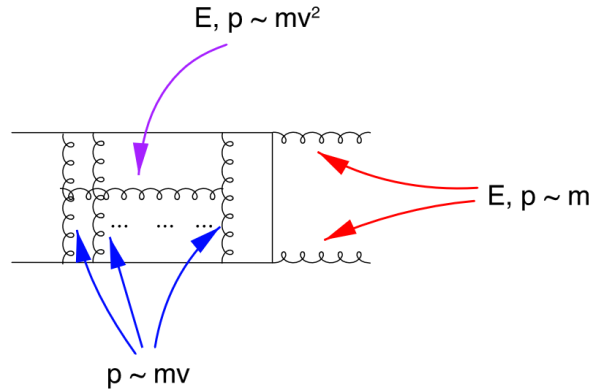


Figure 1.2: Feynman diagram of quarkonium annihilation from [1].

Due to the large mass of the heavy quarks, the relative velocity v between the $Q\bar{Q}$ pair is small ($v \sim 0.3$ for $c\bar{c}$, $v \sim 0.1$ for $b\bar{b}$ with energy $E = mv^2$ 500 GeV); this results in a hierarchy of different energy scales for the gluons exchanged between the two heavy quarks: the hard scale, at around the quark mass m , the soft scale at $p \sim mv$ and the ultrasoft scale at $E \sim mv^2$. Annihilation and production take place at the scale m , binding takes place at scale mv while processes involving soft gluons or light quarks are sensitive to scale mv^2 . This multiple scales are represented as example in the the Feynman diagram of quarkonium annihilation in fig. 1.2 The existence of this hierarchy of scale complicate the calculation, since in perturbative calculation of loop-diagrams the different scales become entangled, thus making the high-order calculations much more challenging [1]

The scale m is also above the Λ_{QCD} threshold, *i.e.* the energy scale below which the QCD processes cannot be treated perturbatively; this approximation is not always valid for the radial excited states: since the radial distance between the two heavy quarks (which is related to $1/p$) becomes larger, the QCD interaction between the two quarks becomes stronger as is shown in Fig. 1.1. Indeed, this behaviour is related to the fact the the coupling constant of the strong force α_s is dependant on the energy scale of the interaction. At sufficiently short distance, which means an higher energy of the gluon exchanged, α_s is sufficiently small to be treated perturbatively. This regime is referred as "asymptotic freedom", since the quarks and gluons do not "feel" the QCD interaction. For higher distance, or lower energy, α_s grows larger, that means that the further one could stretch two quarks, the stronger will be the QCD interaction between them, at the point that instead of separating them, a new *quarkonium* pair is formed in between. Indeed, in nature quarks can't be observed alone, but are always confined in barions and meson, for that the lower energy regime is called "confinement" or "infrared slavery". The Λ_{QCD} scale is energy threshold between this two opposite behaviours of the QCD interaction, while it doesn't assume an exact value, is often assumed to be in the range of few hundreds MeV. Quarkonia states with typical radius smaller than the inverse of Λ_{QCD} are named 'low lying' quarkonia, while states above this threshold, where non-perturbative effects become dominant, are called 'high lying' quarkonia. While the existence of multiple scales makes the QCD calculation difficult, this rich structure make the heavy quarkonium an ideal

laboratory to study the interplay between perturbative and non perturbative QCD in a controlled environment [2].

Quarkonium spectrum

Both charmonium and bottomonium states form a spectrum that it is shown in Fig. 1.3. Each state is defined by three quantum numbers: the total momentum (J), the parity (P) and the charge coniugation C . Total momentum is obtained as the sum of the orbital and spin momenta ($\vec{J} = \vec{L} + \vec{S}$), where \vec{S} and \vec{L} are respectively angular momentum and the total spin of the $Q\bar{Q}$. The value of L determines the parity (P) = $(-1)^{L+1}$, while L and S combined concur to the charge coniugation $C = (-1)^{L+S}$. An additional quantum number n_r is related to the radial excitation of the $Q\bar{Q}$ couple.

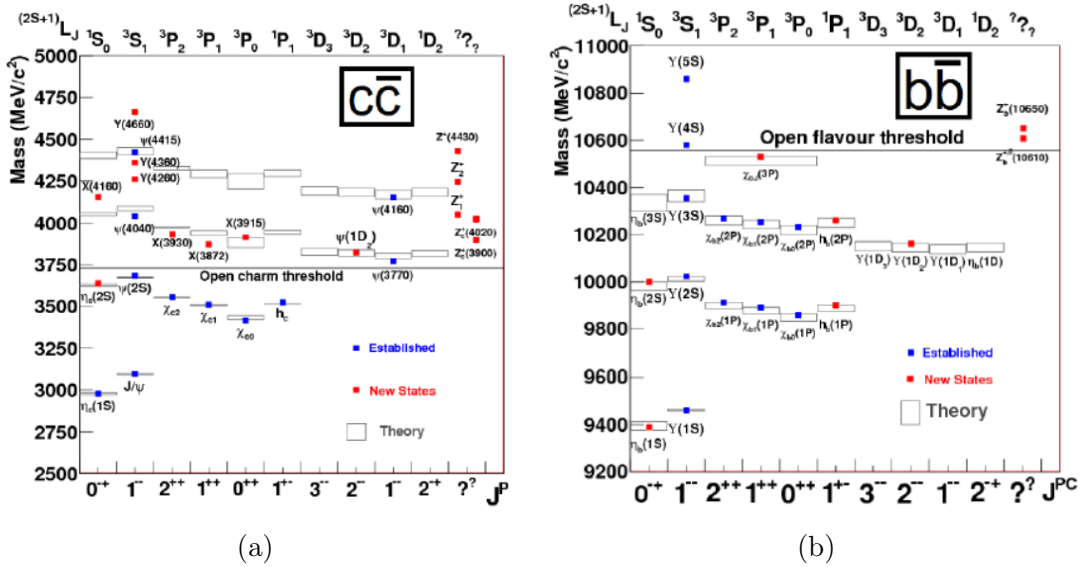


Figure 1.3: Spectra of charmonium (a) and bottomonium (b) states.

The spectrum of both conventional charmonium and bottomonium is well predicted by theory, however in the past decades a number of exotic states has been experimentally observed in various region of mass quite far from predictions of conventional states. Starting from the $X(3872)$ [3] in the charmonium, discovered by the Belle collaboration in 2003, both neutral and charged exotic states have been observed.

Being the first discovered exotic state, the $X(3872)$ has been extensively studied, due to its large number of final states and production techniques in which has been observed. Indeed, the $X(3872)$ has been established in e^+e^- collision at the charmonium energy, in B -meson decays from the B-factories, in pp collision at LHC and $p\bar{p}$ at Tevatron. Hadronic transitions from $X(3872)$ with final states $\pi\pi J/\psi$, $\pi\pi\pi J/\psi$ [4] have been observed with similar branching ratio. Radiative $\gamma J/\psi$ transition has been observed by Belle [5] and LHCb [6] and evidences of $\gamma\psi(2S)$ final state have been reported by BaBar [7] and LHCb [6] with significance of respectively 3.5σ and 4.4σ , while Belle did not observe such transition [5].

Despite the huge amount of experimental data about $X(3872)$, so far there is no general agreement about the nature of this state.

Charged states are particularly interesting: since pure $Q\bar{Q}$ states must be neutral, the charged bound state must contain other components than the heavy quark pair. Since theory predictions for conventional states are quite precise and their widths are naturally narrow, "exotic" states must be ascribed to other contributions over the *pure quarkonium* interpretation (*i.e.* states made only by a pair of $Q\bar{Q}$). While theoretical models will be described in section 1.2.4, hereby the standard nomenclature used in literature to describe these exotic states is presented:

- Y states are exotic neutral states, with quantum numbers $J^{PC} = 1^{--}$. They can be directly produced in e^+e^- collisions.
- Z states are exotic charged states, observed in decays into a quarkonium state and a light hadron. Experimental results lead to an isotriplet interpretation, *i.e.* groups of three particles (Z^+, Z^-, Z^0) with similar mass but different values of isospin.
- X states are all the exotic neutral states with $J^{PC} \neq 1^{--}$.

For both $c\bar{c}$ and $b\bar{b}$ states a threshold can be introduced to distinguish the states that are kinematically allowed to decay into pairs of open flavour mesons, *i.e.* composed by a heavy quark and a light quark. States above the threshold have larger widths compared to the ones below, since the latter can decay only via electromagnetic processes or hadronic decays suppressed by the Okubo-Zweig-Iizuka (OZI) rule. More specifically, the OZI rule states that strong processes whose Feynman diagram is disconnected, *i.e.* it can be cut by trimming the gluon lines, are suppressed. The reason can be traced to the larger number of gluons emitted in comparison to connected processes, leading to a suppression of at least one order of α_s . An example is reported in Fig. 1.4

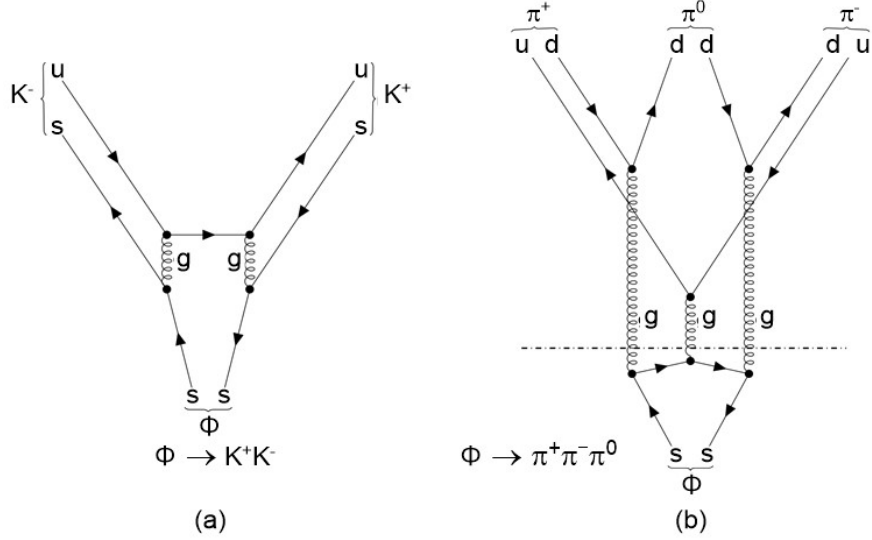


Figure 1.4: Application of the OZI rules in regard of the decay of the Φ meson; the decay into charged kaons requires a connected diagram (a), has $BR(\phi \rightarrow K^+K^-) \approx 49\%$, while the BR for the process with disconnected lines (b) has upper limits of around 6×10^{-4} [8].

Another effect that becomes relevant above the threshold is the coupling of the quarkonium states to the "continuum" contribution of heavy mesons: in fact, above the threshold, the decay coupling of $Q\bar{Q}$ states to $D\bar{D}$ (for charmonium) or $B\bar{B}$ (for bottomonium) is large [9], therefore hadronic loops such as in Fig. 1.5 should become relevant above the threshold.

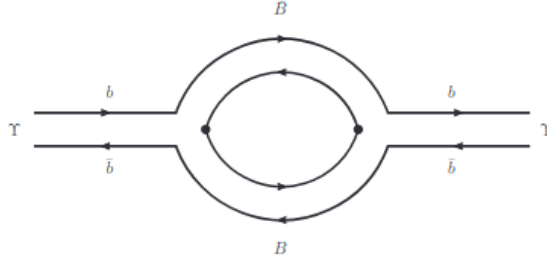


Figure 1.5: Coupling of $b\bar{b}$ states to the $B\bar{B}$ mesons loop.

To study the effects of the hadronic coupling, one can describe the full hadronic state $|\Psi\rangle$ as a linear combination of $|\psi_q\rangle$ (for the confined quarkonium states) and $|\phi_Q\phi_{\bar{Q}}\rangle$ (for the two heavy mesons). The wave function $|\Psi\rangle$ obeys the equation:

$$\mathcal{H}|\Psi\rangle = M|\Psi\rangle, \quad \mathcal{H} = \begin{pmatrix} H_0 & H_I \\ H_I & H_{Q\bar{Q}} \end{pmatrix} \quad (1.1)$$

where H_0 is the hamiltonian for the $Q\bar{Q}$ system, with eigenstate determined by $H_0|\psi_q\rangle = M_q|\psi_q\rangle$. The hamiltonian $H_{Q\bar{Q}}$ acts on the heavy meson, neglecting interaction between them, in the following way:

$$H_{Q\bar{Q}} |\phi_Q \phi_{\bar{Q}}\rangle = (E_Q + E_{\bar{Q}}) |\phi_Q \phi_{\bar{Q}}\rangle \approx (M_Q + M_{\bar{Q}} + \frac{\mathbf{p}^2}{2\mu_{Q\bar{Q}}}) |\phi_Q \phi_{\bar{Q}}\rangle \quad (1.2)$$

where $\mu_{Q\bar{Q}} = \frac{M_Q M_{\bar{Q}}}{M_Q + M_{\bar{Q}}}$ is the reduced mass of the two mesons.

The interaction hamiltonian H_1 couples the $Q\bar{Q}$ states to the heavy hadrons and is described following the P_0 [10] model. In this model, the mixing between the bare quarkonium state ($c\bar{c}$ or $b\bar{b}$) and their open flavour meson pair ($c\bar{q}$ and $q\bar{c}$ or $b\bar{q}$ and $q\bar{b}$) is described via the creation from the vacuum of a $q\bar{q}$ pair with $J^{PC} = 0^{++}$. This leads to the definition [9]:

$$H_1 = g \sum_q \int dx^3 \bar{\psi}_q \psi_q \quad (1.3)$$

where g is the coupling constant and ψ_q is the quark Dirac field.

The open flavour coupling results in predicted mass shift in the order of 200 MeV/c² for charmonium [11] and 100 MeV/c² for bottomonium [9], suggesting that the hadronic loops are much more relevant in the charmonium sector.

Quarkonium Production at e^+e^- colliders

In this section it will be briefly discussed how quarkonium states can be produced at colliders, more specifically in e^+e^- colliders, since this is the type of events Belle II works with.

The electromagnetic current e^+e^- has $J^{PC} = 1^{--}$; since the electromagnetic interaction conserve the quantum numbers, the only possible states that can be produced directly in the e^+e^- collisions are the ψ states at the charmonium energies, the Υ states at the bottomonium energies, and the exotic Y states. The states can be produced at resonance, *i.e.* when \sqrt{s} (the total center of mass energy of the collision) is close to the mass of the state, or at higher energy in collisions with Initial State Radiation (ISR). In the latter case a photon is emitted by the electron or the positron before the collision, thus lowering the available energy of the final states. This means that resonance at lower masses can be produced even at higher \sqrt{s} . Charmonium states can also be obtained via decays of B -mesons, double charmonium production (*i.e.* direct production of two charmonium states together) or photon-photon scattering. Double charmonium production was observed at B-factories in $e^+e^- \rightarrow J/\psi X$, where X is $\eta_c, \chi_{c0}, \eta_c(2S)$ by Belle with cross section larger than the theoretical predictions [12]. Photon-photon scattering is studied via the process $e^+e^- \gamma^* \gamma^* \rightarrow e^+e^- R$, giving access to J even states with positive C . Production via B-meson decay involves the weak decay of the b quark inside the meson to a c , the products of the W boson decay combines with the newly produced c quark and with the light quark in the B-meson to form a light meson and a charmonium state.

An illustration of these mechanisms is reported in Fig. 1.6.

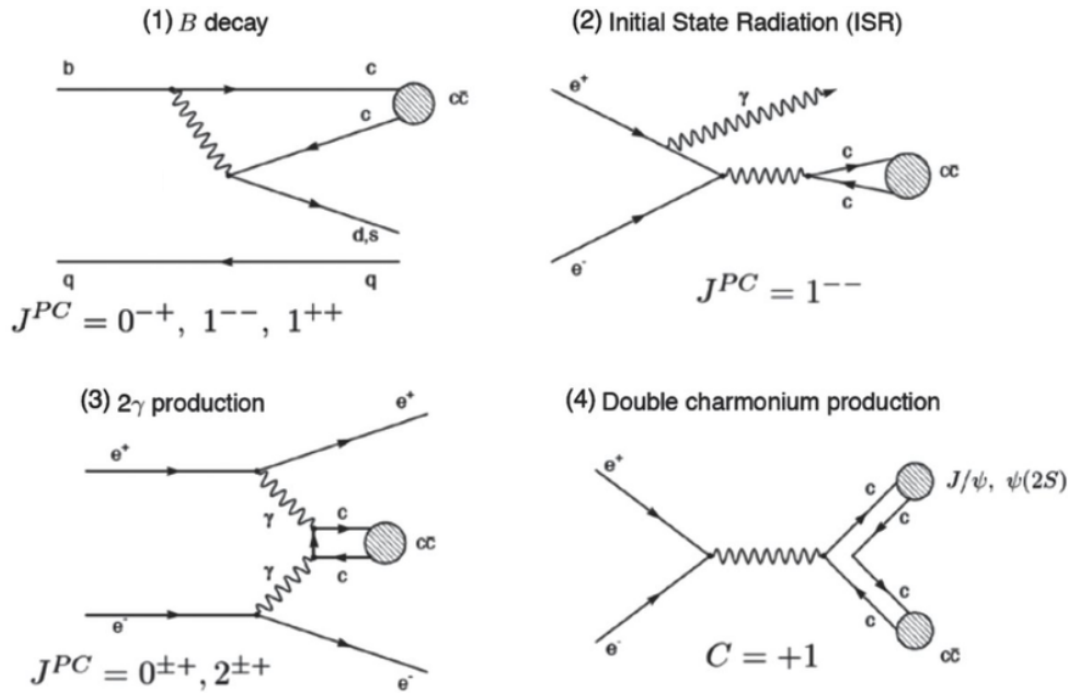


Figure 1.6: Production of charmonium via *B* decays, Initial State Radiation, double charmonium production and photon-photon scattering.

Direct production of bottomonium states is confined to 1^{--} structures, that can be produced both on resonance or via ISR from higher energy. Other states can still be reached via radiative or hadronic transitions, such as involving γ , η , η' , ρ , $\pi\pi$ and KK couples, and so forth.

An overview of the established bottomonium spectrum alongside the possible transitions between all the states is reported in Fig. 1.7.

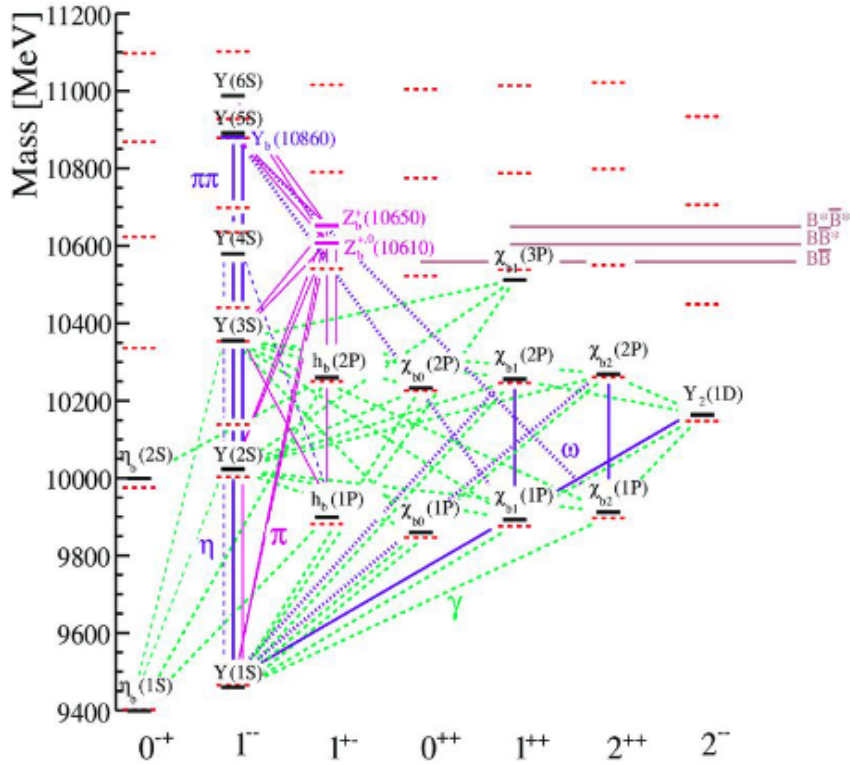


Figure 1.7: Overview of the bottomonium spectrum and the involved transitions.

1.2 Theoretical models

The first widely used approach to study the quarkonium states was to consider the system in analogy to the positronium (*i.e.* the bound state of e^+e^-), and resolve the Schrödinger equation in a non relativistic limit, introducing a potential $V(r)$ as a function of the distance r between the two heavy quarks. Corrections up to the order $\frac{v^2}{c^2}$ are treated as a perturbation due to relativistic terms in the potential and in the kinetic energy. However, more advanced models to study quarkonium have been developed in the years: lattice QCD and non relativistic effective fields theory (NREFT). Lattice QCD takes advantage of the non perturbative regime to perform numerical path integration on a discrete Euclidean space. Using the hierarchy of scales one can instead use simpler NREFTs to substitute QCD and integrate out contributions from higher energy not relevant for the process under study [2]. A brief outline of the three models is presented below.

1.2.1 Potential Model

The shape of the potential at short distance is obtained via perturbative QCD; since at the lowest perturbative order the QCD interaction is analogous to the QED, one can use the Coulomb-like potential:

$$V_0(r) = -\frac{4}{3} \frac{\alpha_s}{r} \quad (1.4)$$

where α_s is the QCD coupling constant. Taking into account the dependence of the coupling on the scale, α_s is substituted with the running coupling α_r . However, perturbative QCD is applicable only at distances shorter than the average size of the quarkonium states, while for intermediate and long distances one has to use models for the interaction between quarks. This is done by describing the confinement with a rising potential at long distance, usually using a linearly growing potential. One of the most used is the Cornell potential, which starts from the simplest potential, built as a sum of a Coulomb-like and a linear contribution:

$$V(r) = -\frac{k}{r} + \frac{r}{a} \quad (1.5)$$

Effects such as fine splitting (between states with same L and S but different J) and hyperfine splitting (between spin-triplet and spin-singlet state) are the result of the relativistic terms. The coupling with a pair of heavy hadrons for quarkonium above the threshold is also introduced, since it would be ignored in a pure potential model with confining conditions.

1.2.2 Lattice QCD

Lattice QCD allows to compute expectation values of a physical quantity C (e.g. a decay width), by performing a numerical path integration:

$$\int \mathcal{D}G \mathcal{D}q_i \mathcal{D}\bar{q}_i e^{-S_{QCD}} C \quad (1.6)$$

on a discrete and Euclidean phase space. G, q_i, \bar{q}_i are the quantum fields for gluons and quarks, which are transcribed on the lattice preserving Gauge invariance. Since the field configurations can be in principle infinite, they are generated via Monte Carlo (MC) methods. Path integration is performed via MC integration, therefore lattice calculations have both systematic (from the discrete space-time integration) and statistical uncertainties.

The parameters of the lattice action are the masses of the quarks and the coupling α_s . States below the open flavour threshold can be treated in a perturbative approximation. A comparison between experimental measurements and models from [13] is presented in Fig. 1.8

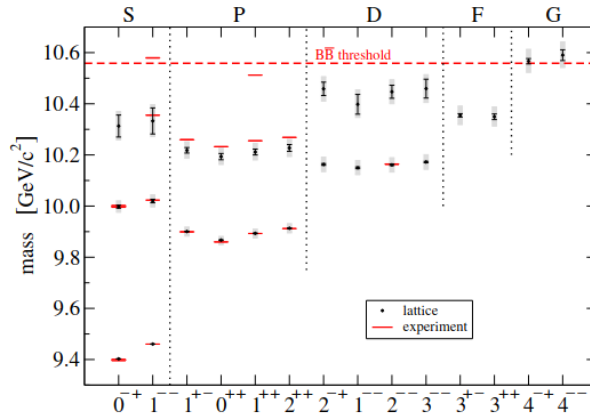


Figure 1.8: Lattice spectra of bottomonium states below the threshold from [13], compared to experimental measurements (red lines).

Extra caution is needed when treating states above the threshold, since the perturbative approximation is not valid for radial excited states and the coupling with heavy mesons has to be taken into account. There are various approaches in order to solve lattice calculations in this environment, but they are beyond the scope of this thesis and will not be discussed here.

1.2.3 Non Relativistic Effective Field Theory

Non Relativistic Effective Field Theory (NREFT) is the result of integrating out the degrees of freedom related to scale m , thus obtaining a Lagrangian in the form of:

$$\mathcal{L}_{NRQCD} = \sum_n \frac{c_n(\alpha_s, \mu)}{m^n} \times O_n(\mu, mv, mv^2, \dots) \quad (1.7)$$

where O_n are operators of non relativistic QCD relevant at the mv and mv^2 scales, μ is the NRQCD factorization term and c_n are the coefficients that encode the contribution from the scale m . The low-operators O_n are constructed out of two or four heavy quarks/antiquark fields and gluons. While NRQCD can be used for spectroscopy calculations on lattice, it has been also used to study quarkonium and double quarkonium production [14] [15].

1.2.4 Exotic states

A number of models has been proposed by theorist to explain the exotic states that has been observed in both quarkonium and charmonium spectra, with the majority of them introducing other degrees of freedom in addition to the two quarks.

A non-exhaustive list is briefly presented in [2].

Tetraquark In this description there is a contribution from light quarks in addition to the heavy ones, specifically the light and heavy quarks as well as

the antiquarks are paired together to form compact diquarks and anti-diquarks substructure. These states are very compact and have narrow decay widths.

Hadronic molecules Quarks and anti-quarks are paired in a couple of loosely bound open-flavour mesons. These states are larger than tetraquarks, and have large decay widths.

Hadroquarkonium In this model the heavy quark and anti-quark are coupled together and surrounded by light quarks and anti-quarks.

Hybrids In these states, beyond the two quarks, also gluons act as active degrees of freedom[16].

Glueballs Buond states of gluons with no valence quarks involved. Lattice calculation led to mass up to $5 \text{ GeV}/c^2$ [17].

A detailed overview of all the so far discovered exotic states will not be presented here. However, a brief outlook of two specific states, the $Z_b^\pm(10610)$ and the $Z_b^\pm(10650)$, will be reported in the following section, since they could play a role in this analysis. The discovery of the $Y(10753)$ will be also discussed, as this thesis focus on this resonance.

1.3 $Z_b^\pm(10610)$ and $Z_b^\pm(10650)$ at Belle

The Belle physics program was mainly focused on the study of flavour physics at the $Y(4S)$ energy; although, data taking campaigns were also performed at different energies (Table 1.1). Among others, one aim was to perform spectroscopy studies above the open flavor threshold.

Resonance	On-peak luminosity (fb^{-1})	Off-peak luminosity (fb^{-1})
$\Upsilon(1S)$	5.7	1.8
$\Upsilon(2S)$	24.9	1.7
$\Upsilon(3S)$	2.9	0.3
$\Upsilon(4S)$	711	89.4
$\Upsilon(5S)$	121.4	1.7
<i>Scan</i>	0.716	27.6

Table 1.1: Summary of the integrated luminosity of Belle.

A large number of $h_b(1P)$ and $h_b(2P)$ conventional states were unexpectedly observed in the $\Upsilon(5S) \rightarrow \pi\pi h_b(mP)$ ($m = 1, 2$) hadronic transitions [18]. The $h_b(mP)$ were observed in the $\pi\pi$ recoil spectrum, as can be see in Fig 1.9.

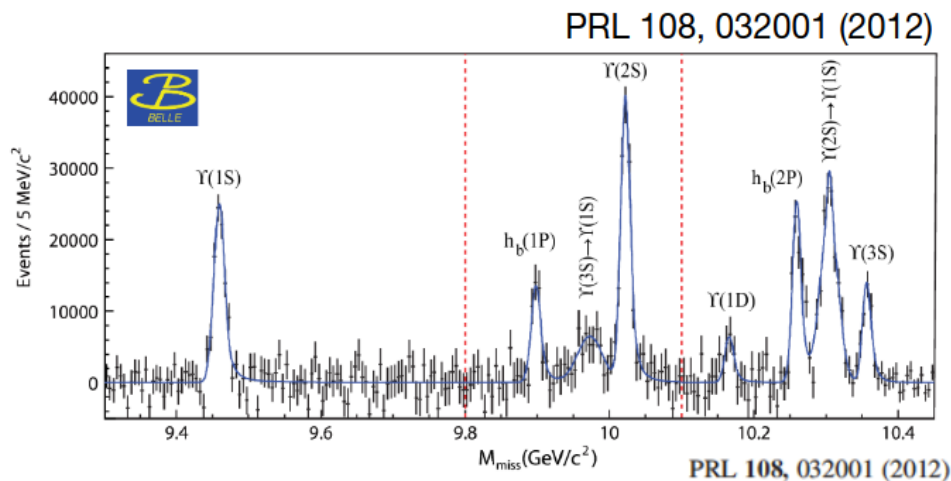


Figure 1.9: Spectrum of the dipion recoil mass ($M_{miss}(\pi\pi)$) at the $Y(5S)$ as reported in [18].

The $\Upsilon(5S) \rightarrow \pi\pi h_b(mP)$ process should be suppressed both due to the OZI rule and the heavy quark spin symmetry. Indeed, heavy quark spin symmetry (HQSS) involves heavy hadrons in general and states that in the $m_Q \rightarrow \infty$ limit, the dynamics of heavy hadrons which differ only for the spin and flavour of the heavy quark is perfectly identical [19]. This is valid since the relativistic interaction between the light and heavy quarks vanishes as $m_Q \rightarrow \infty$. One implication of the HQSS in the heavy quarkonium spectroscopy is the fact that any transition that spins the flip of a quark should not be possible, since it would carry

a factor proportional to $1/m^2$, that will vanish in the $m_Q \rightarrow \infty$ approximation. While HQSS is not an exact symmetry, since the mass of the heavy quarks is large but finite, the spin flip transitions are still greatly suppressed, due to the mass square factor.

Since the $\Upsilon(nS)$ are spin triplet states while $h_b(mP)$ are spin singlets, a transition between the two would require a spin flip, therefore it would be greatly suppressed for the aforementioned reasons. The large amount of $h_b(mP)$ can be explained by the presence of the charged intermediate states $Z_b(10610)$ and $Z_b(10650)$, that allows the transition to happen without a spin flip, as shown in Fig. 4.6.

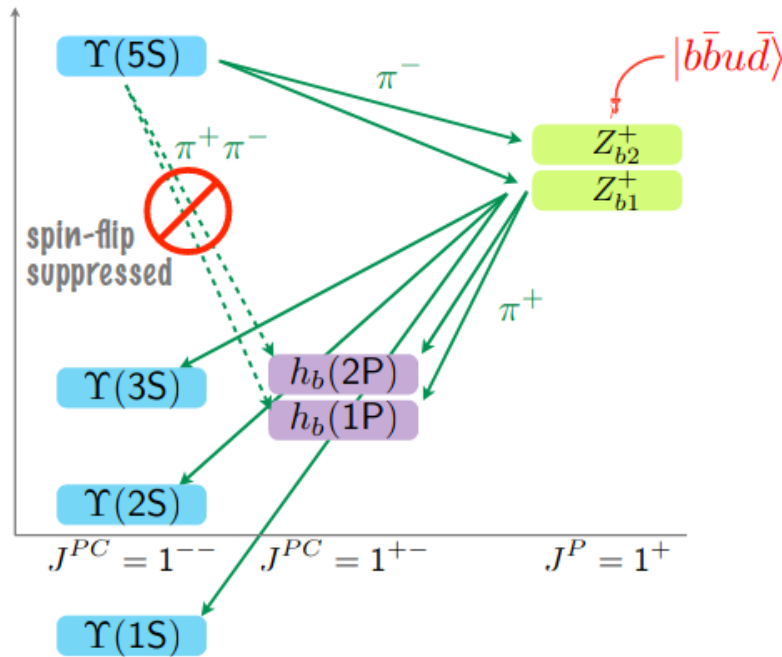
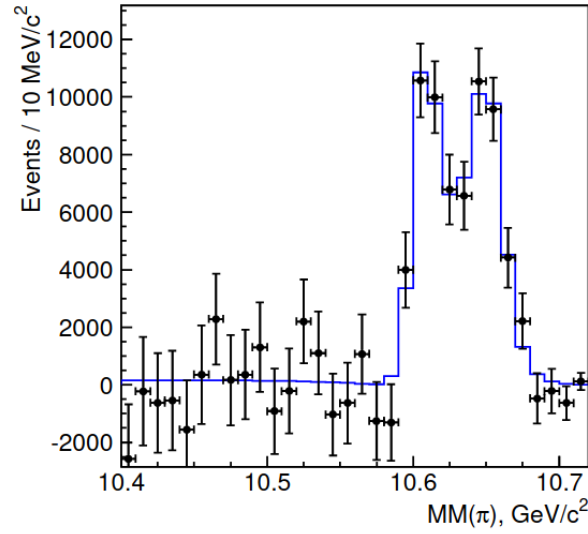
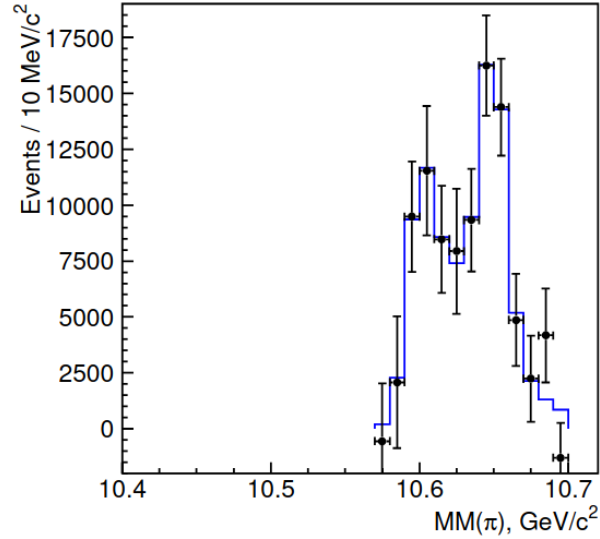


Figure 1.10: Cascade decays involved in the $\Upsilon(5S)$ to the $h_b(1P)$ state.

Evidences of the transitions via Z_b states have in fact been found [20] measuring the transition $\Upsilon(5S) \rightarrow \pi\pi h_b(mP)$ and looking at the distribution of the recoil mass of the single pion $M_{miss}(\pi)$. The distributions were fitted, obtaining two clear peaks as shown in Fig. 4.8.



(a)



(b)

Figure 1.11: Distributions of $M_{miss}(\pi\pi)$ for $h_b(1P)$ (a) and $h_b(2P)$ (b) events. Points with error bars are data, blue lines are the fit results [20].

The non-resonant component for the $e^+e^- \rightarrow \pi\pi h_b(2P)$ final states has been estimated as close to zero, therefore $e^+e^- \rightarrow \pi Z_b$ seems to be the only way to produce $h_b(2P)$ via dipion transition from $Y(5S)$.

Interpretation of the Z_b states

The $Z_b^\pm(10610)$ and $Z_b^\pm(10650)$ decay to bottomonium states, therefore they must have a $b\bar{b}$ component, and since they are charged they must be composed by at least four quarks, making them manifestly exotic.

The Z_b looks like the bottomonium counterpart of the $Z_c(3900)$ [21][22] and $Z_c(4020)$ [22][23] charmonium-like states, which are most likely identified as isotriplets with quantum numbers $J^P = 1^+$. However, while evidence for a neutral partner has been found for both the Z_c [24] [25] and the $Z_b(10610)$ [26], thus completing the triplets, this has not been the case for the $Z_b(10650)$.

This charged states are also very close to open flavour threshold, and a molecular interpretation was introduced after their discoveries: $B\bar{B}^*$ and $B\bar{B}^*$ for Z_b [27] and $D\bar{D}^*$ and $D\bar{D}^*$ for Z_c [17][28]. Their measured spin and parity $J^P = 1^+$ correspond to heavy-light mesons in S -wave, in line with a molecular interpretation.

The existence of the charged states as the Z_c^\pm and Z_b^\pm resonances is also predicted by the tetraquark models; moreover, according to the present data, the mass of all these states is above their meson-meson thresholds with the corresponding quantum numbers. This is a hint toward a tetraquark interpretation: since diquarks (which compose the tetraquarks) are slightly less bound than colour singlets, they should appear close, yet above, the open flavor thresholds.

1.4 $Y(10753)$

Another Belle result in the bottomonium sector was the discovery of the $Y(10753)$ state during the scan of the energies above the $\Upsilon(4S)$. This resonance was found in $e^+e^- \rightarrow \pi\pi\Upsilon(nS)$ ($n = 1, 2, 3$) cross section [29].

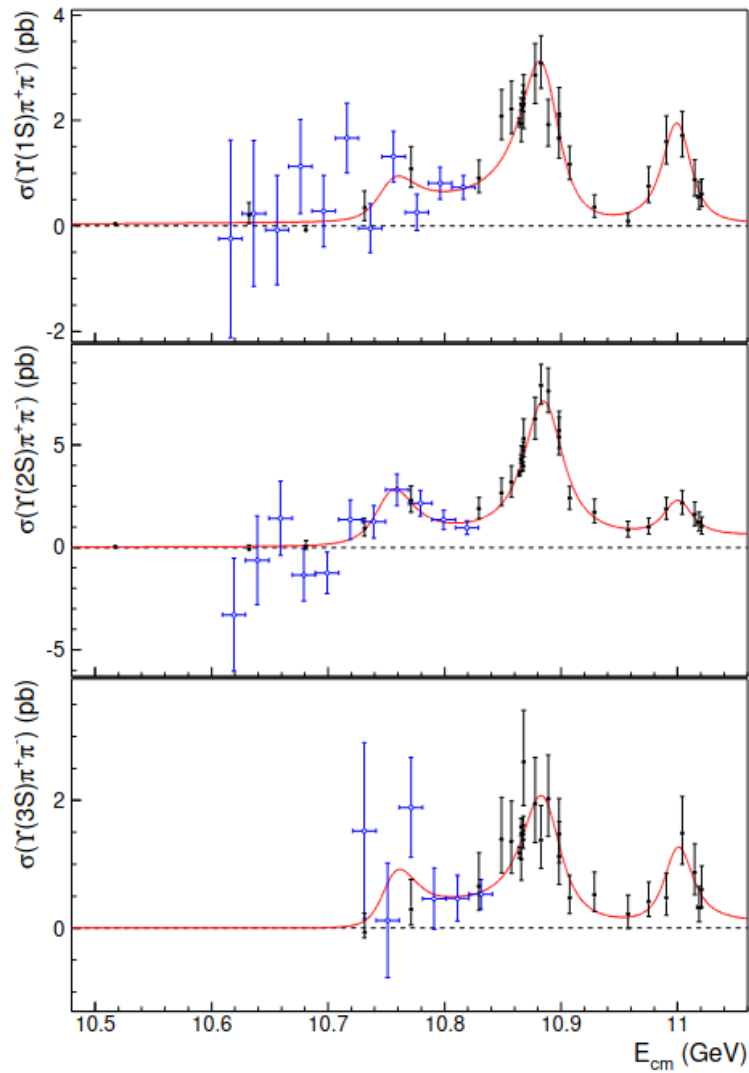


Figure 1.12: Energy dependence of the $e^+e^- \rightarrow \pi\pi\Upsilon(nS)$ cross sections [29]. Black points with error bars are data from the energy scan, red lines are the result of the simultaneous fit to these distributions, blue dots with error bars are the cross section values estimated with ISR from $\Upsilon(10860)$.

The structure was described with a Breit-Wigner amplitude, obtaining the following values for mass and with:

Mass	$10751 \pm 5.9^{+0.7}_{-1.1} \text{ MeV}/c^2$
Width	$35.5^{+17.6+3.9}_{-11.3-3.3} \text{ MeV}$

The structure was observed with one point on resonance and three points in the region of interest, with luminosity of 1 fb^{-1} each and a 5.2σ significance. Since it was produced directly in the e^+e^- , it was given the quantum numbers $J^{PC} = 1^{--}$.

Further evidences of this structure were obtained by the measurement of the $e^+e^- \rightarrow b\bar{b}$ cross section with ISR correction by BaBar for the refitting of $R_b = \sigma(e^+e^- \rightarrow b\bar{b})/\sigma(e^+e^- \rightarrow \mu\mu)$ [30](Fig. 1.13)

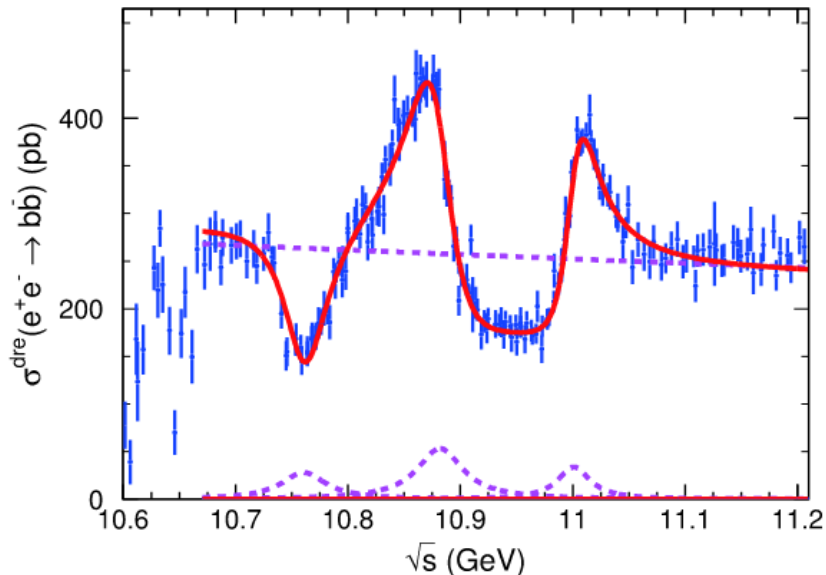
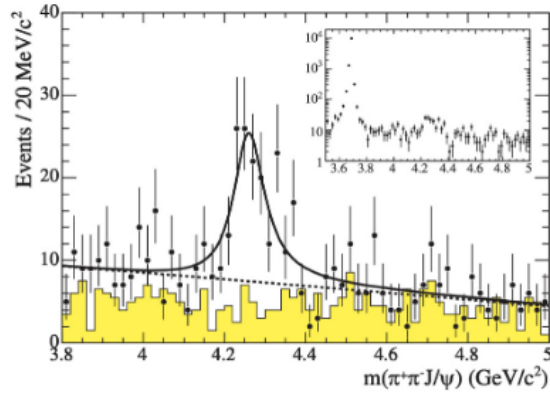


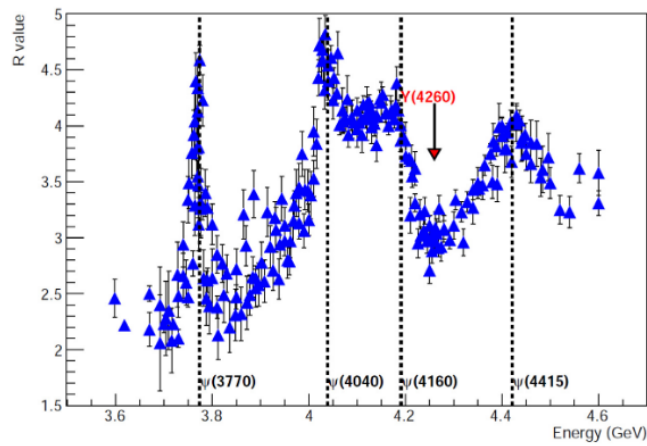
Figure 1.13: Fit of the $e^+e^- \rightarrow b\bar{b}$ cross section with coherent sum of continuum amplitude and three Breit-Wigner functions.

The dip at around 10750 MeV is described as an interference between the continuum amplitude and a Breit-Wigner with Mass = (10761 ± 2) MeV/ c^2 and width = (48.5 ± 3.0) MeV.

The $Y(10753)$ presents some analogies with the $Y(4260)$ in the charmonium sector, which is an exotic state with the same quantum numbers $J^{PC} = 1^{--}$ as the $Y(10753)$. The $Y(4260)$ was observed both in the $e^+e^- \rightarrow \pi\pi J/\psi$ [31] and as a dip in the $\sigma(e^+e^- \rightarrow d\bar{d})$ [32] (see Fig. 1.14).



(a)



(b)

Figure 1.14: (a) Invariant mass of $\pi^+\pi^-J/\psi$ as measured by BaBar [31] with the peak of the $Y(4260)$; (b) $R = \sigma(e^+e^- \rightarrow \text{hadrons})/\sigma(e^+e^- \rightarrow \mu^+\mu^-)$ from [32].

The $Y(10753)$ nature is still unclear: since no S-wave threshold is located near the $Y(10753)$, a molecular nature is unlikely; neither a direct match to a conventional state is present, although possibilities of an $S - D$ mixing has been investigated [33]. Tetraquark interpretations have also been proposed [34] and branching ratios of the decays to $B\bar{B}$ have been predicted with most of the models, alongside other transitions into bottomonia (Table 1.2).

Mode	$\mathcal{B}(4q)(\%)$	$\mathcal{B}(b\bar{b})(\%)$
$B\bar{B}$	$39.3^{+38.7}_{-22.9}$	21.3
$B\bar{B}^*$	~ 0.2	64.1
$B^* \bar{B}^*$	$52.3^{+54.9}_{31.7}$	0.3
$B_s \bar{B}_s$	—	0.3
$\omega\eta_b$	$7.9^{+14.0}_{-5.0}$	—
$\omega\chi_{bJ}$	—	~ 0.3
$\eta\Upsilon$	—	~ 0.2
$\eta\Upsilon$	—	~ 0.06
ηh_b	—	~ 0.2

Table 1.2: Predictions of $Y(10753)$ branching ratios under different interpretations as reported in [34][35][36][37][38][39][40]

Figure 1.15 shows the prediction for the spectrum of the dipion invariant mass in $Y(10753) \rightarrow \pi\pi\Upsilon$, under tetraquark assumption, provided by [34].

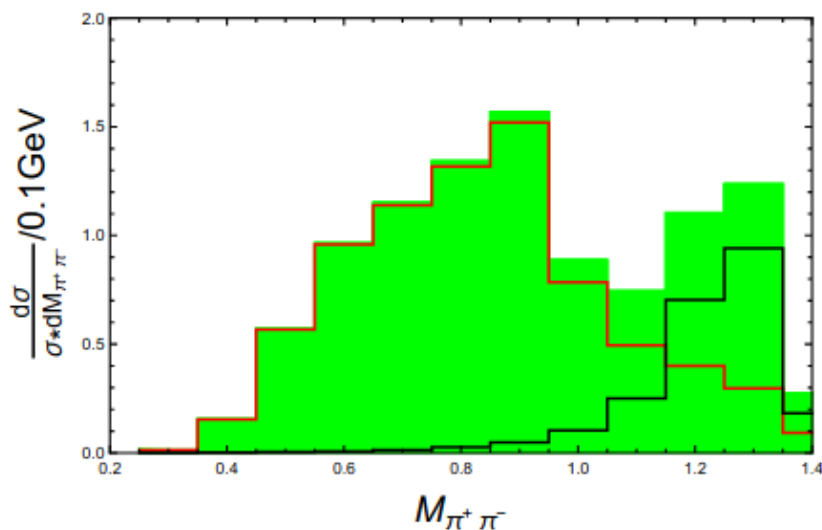


Figure 1.15: Normalized resonant distribution [34] for $M(\pi\pi)$ (GeV) in the $e^+e^- \rightarrow Y(10753) \rightarrow \pi\pi\Upsilon(1S)$. Colored lines are the separate contributions for the scalar $f_0(500)$ $f_0(980)$ (red line) and the tensor $f_2(1270)$ (black line) involved in the model.

The physical picture for the $Y(10753)$ is interesting, due to its exotic nature and the charmonium analogy, however more statistics is needed to discriminate between the models and to study different decay channels. In November 2021 Belle II performed a scan above the $\Upsilon(4S)$, taking data at four energy point between the ones already investigated by Belle, with a much higher luminosity (Fig. 4.6).

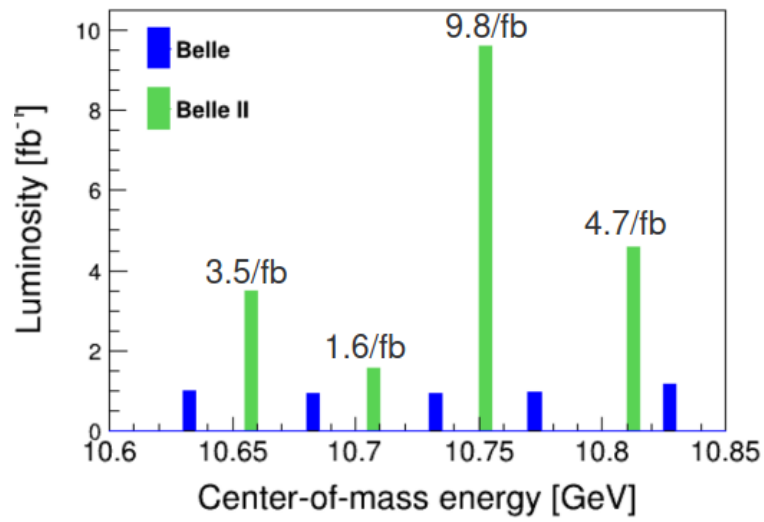


Figure 1.16: Plot of the luminosity at each energy point of the scan of Belle II around the $Y(10753)$ (green); the blue histogram corresponds to the energy that Belle already measured.

By investigating different decay modes, it should be possible to determine the nature of the $Y(10753)$, while exploring further similarities with the charmonium.

Chapter 2

The Belle II Experiment

The Belle II experiment is located at the SuperKEKB facility at Tsukuba (Japan). The main goal of the experiment is to search for new physics (NP) in the flavour sector and to improve the precision of Standard Model (SM) parameters.

This chapter is focused on the Belle II experiment, and it is organized as follows: the SuperKEKB collider will be presented in section 2.1 and an overview of the Belle II detector and its subsystems is presented in section 2.2.

2.1 The SuperKEKB facility

SuperKEKB [41] is an asymmetric electron-positron double ring collider constructed, by upgrading the previous KEKB B-factory. The design luminosity of superKEKB is $8 \times 10^{35} \text{ cm}^{-2} \text{ s}^{-1}$, which is 40 times the luminosity achieved by KEK, with the goal to accumulate 50 ab^{-1} of data. SuperKEKB started operations in 2018 [42], and so far reached the world highest instantaneous luminosity of $4.7 \times 10^{34} \text{ cm}^{-2} \text{ s}^{-1}$, and an integrated luminosity of 424 fb^{-1} . The collider complex consists of a 7 GeV electron ring (called the high-energy ring, HER) and a 4 GeV positron ring (the low-energy ring, LER); the gain in luminosity with the respect to the former facility comes mainly from the significant decrease of the beam size at the interaction point, based on the nanobeam collision scheme.

A comparison of the beam configuration in KEKB and SuperKEKB is shown in Fig. 2.1

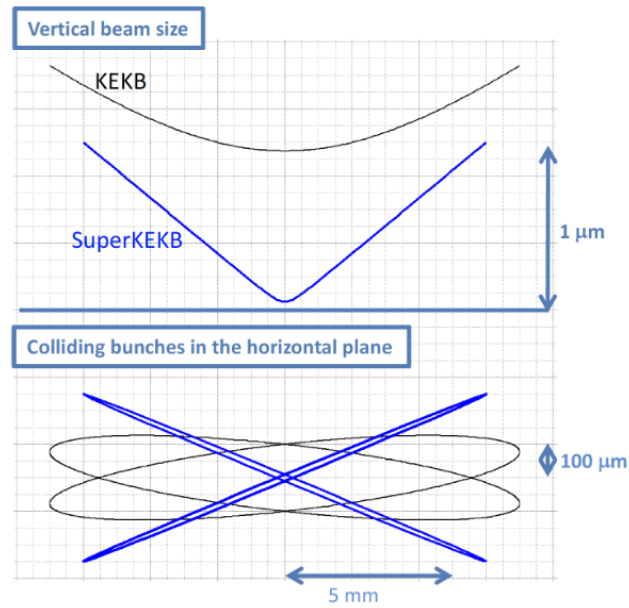


Figure 2.1: Schematic view of the nanobeam scheme adopted in SuperKEKB (blue lines) in comparison with KEK (black lines).

While the energy of the beams can be modulated, allowing to take data at different \sqrt{s} , most of the data are acquired at the $\Upsilon(4S)$ resonance, where a large amount of $B\bar{B}$ mesons are produced via $\Upsilon(4S) \rightarrow B\bar{B}$. The asymmetric energies of the beams are designed in order to boost the decay products of the $\Upsilon(4S)$. The $\Upsilon(4S)$ mass is just 20 MeV above the $B\bar{B}$ threshold, thus the mesons are produced nearly in the rest frame; since the life time of the neutral B-mesons is short ($\tau = 1.510 \times 10^{-12}$ s) and they are produced with relatively slow velocities, they travel for short distance in the center of mass frame before decaying, making it difficult to separate the decays of the two produced mesons. The asymmetric energy provides a boost in order to extend the decay length of the mesons in the laboratory frame. A schematic view of the SuperKEKB facility is reported in Fig. 2.2.

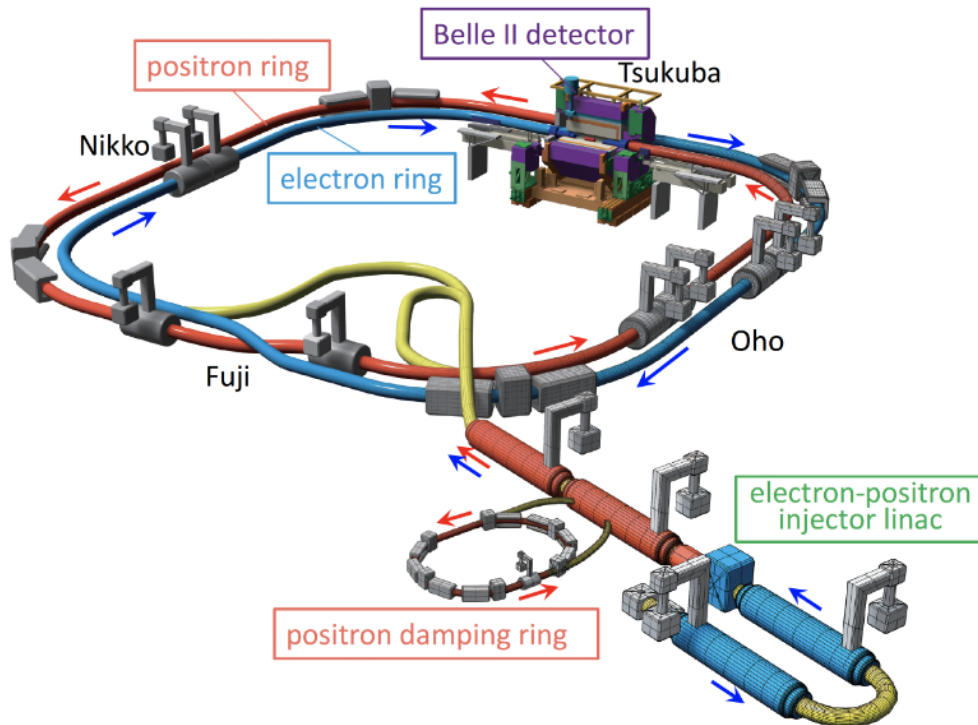


Figure 2.2: Schematic view of the SuperKEKB facility. The electron and the positron beams collision point is located in the Tsukuba section, where the Belle II detector is located.

2.2 The Belle II detector

Belle II is a nearly 4π magnetic spectrometer surrounded by a calorimeter and a muon detector [43]. The beam pipe around the interaction point (IP) is made of Beryllium (Be) to minimize the material budget, due to its lower radiation length (X_0) which reduces the multiple scattering.

The detector comprises of several subdetectors arranged cylindrically around the interaction space-point, with a polar structure that reflects the asymmetric distribution of the final states particles obtained in a boosted collision. A multi level trigger is used to identify the event of interest during data taking. The cylindrical volume around the beam pipe is called the "barrel", while the region that would correspond to the bases of the cylinder are the forward (in the direction of the e^- momentum) and backward (direction of the e^+ momentum) "end-cap"; a schematic view of the Belle II top view is shown in Fig. 2.3

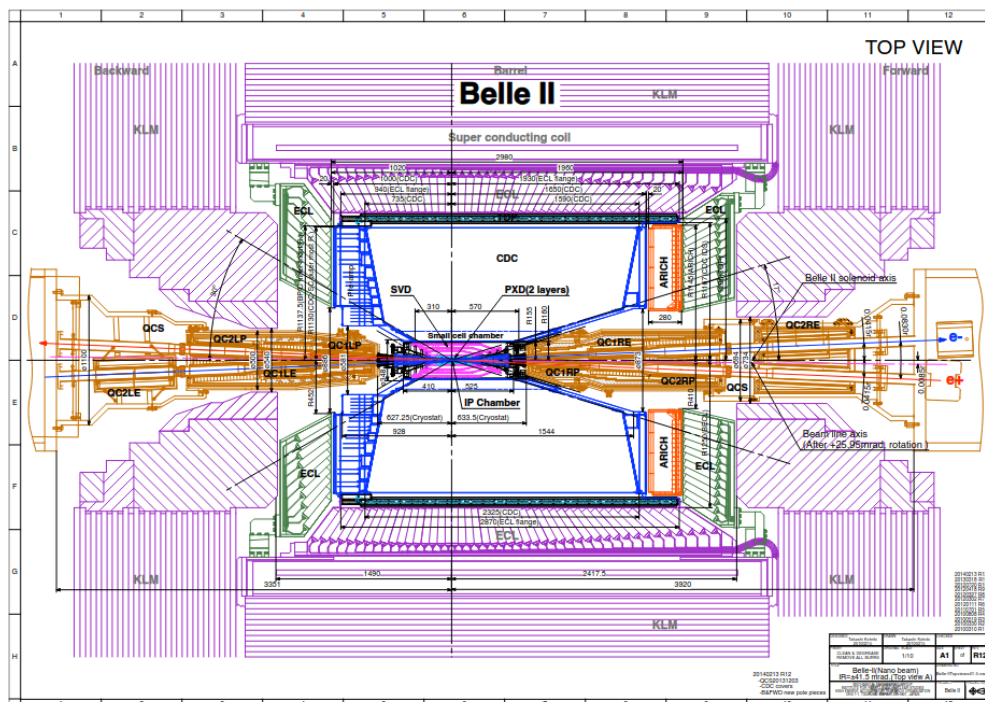


Figure 2.3: Belle II Top view.

From innermost to outermost the subdetectors are:

- The vertex detector (VXD), composed by two layers of silicon pixel detectors (PXD) and four layers of silicon strip detector (SVD), has the main scope of reconstructing the vertex of the tracks, but contributes also to the tracking.
- The central drift chamber (CDC), a large volume drift chamber which is the main device for tracking the charged particles into the detector.
- The particle identification system, composed by a time-of-propagation (TOP) Cherenkov counter for the barrel region and a proximity focusing Cherenkov ring imaging (ARICH) for the forward end-cap region.
- The electromagnetic calorimeter (ECL), to detect photons and to identify charged particles, especially electrons.
- The K_L -muon detector (KLM), that consists of 4.7 cm thick iron plates alternated to active detector elements, to tracks muons and K_L .

Between the calorimeter and the KLM there is the solenoid coil, that provides a 1 T axial magnetic field, in order to bend charged particles for the measurement of their charge and momentum by the tracking system. In Fig. 2.3 a top view of Belle II is presented. Each subdetector will be discussed in its dedicated section [2].

2.2.1 Vertex Detector (VXD)

The vertex detector is comprised of two devices, the silicon Pixel Detector (PXD) [44] and the Silicon Vertex Detector (SVD) [45], with a total of six layers around the

beam pipe. A schematic view of the Belle II SVD is shown in Fig. 2.4. With respect of the direction of the e^- beam, the VXD covers the polar angle interval of $17^\circ < \theta < 150^\circ$, and has full coverage of the azimuthal angle.

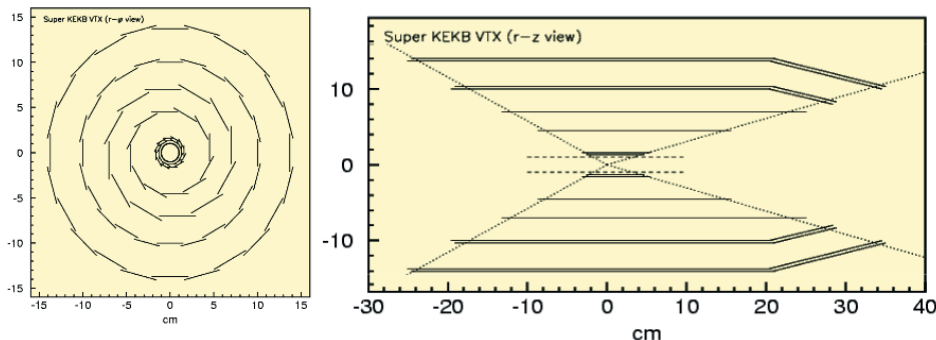


Figure 2.4: Schematic view of the Belle II VXD.

The first two layers, at radii 14 and 22 mm, use pixelated detector of the DEPFET type, which are characterized by fast charge collection ($O(\text{ns})$), high signal-to-noise ratio and low power consumption. The remaining four layers, at radii of 38 mm, 80 mm, 115 mm and 140 mm, are equipped with double-sided silicon strips. A track leave a signal on both sides of each strip, thus the highest number of hits a particle can have in the SVD should be 8, but since the modules are superimposed in certain region of ϕ , as one can see in Fig. 2.4, the maximum amount of hits is 16 instead.

2.2.2 Central Drift Chamber (CDC)

The CDC [46] is the main tracking system of the Belle II detector; it is composed by a large drift chamber with small drift cells, and is extended to a radius of 1130 mm. In total the CDC contains 14336 wires arranged in 56 layers, either parallel to the longitudinal magnetic field (*axial* orientation) or skewed respect to the axial wires (*stereo* orientation). By combining the information of both axial and stereo wires it is possible to reconstruct a full 3D helix track. The CDC can also perform PID via dE/dx measurement.

As for the SVD, the CDC covers a polar angle interval of $17^\circ < \theta < 150^\circ$, and has full coverage of the azimuthal angle. The gas that fills the chamber is a 50:50 mixture of $He - C_2H_6$; the gas was chosen as a compromise between a good momentum resolution for tracking and good dE/dx resolution for the PID: the former requirement implies a lower Z to reduce multiple scattering, while a Z too low would reduce the dE/dx of the particles, thus compromising the PID performances.

A picture with a schematic view of the *CDC* is presented in Fig. 2.5.

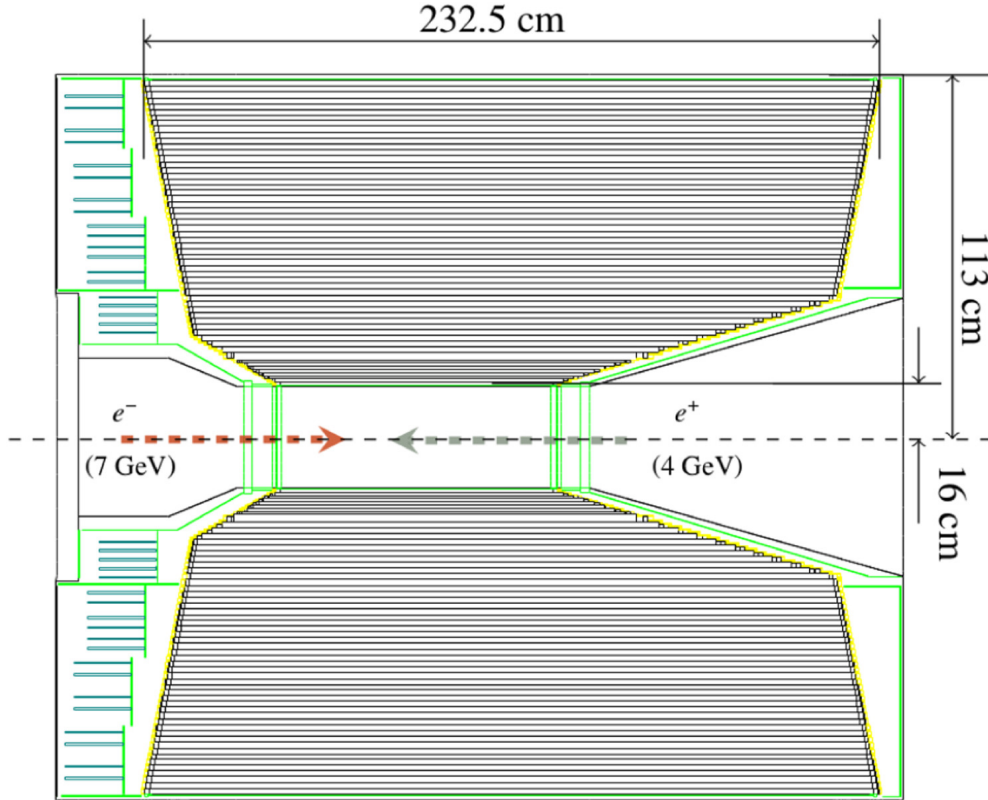


Figure 2.5: Schematic view of the Belle II CDC.

2.2.3 PID systems: ARICH and TOP

The ARICH, a proximity ring imaging Cherenkov detector [47], is located at the front end barrel and is optimized for the K and π identification. The Cherenkov radiator is composed by two 2 cm thick layers of aerogel, with different refractive indices, n_1 and n_2 . Particles crossing the Cherenkov radiator with $\beta > \frac{c}{n_i}$ will emit photons at an angle of $\theta = \arccos\left(\frac{1}{\beta n_i}\right)$, as in Fig. 2.6.

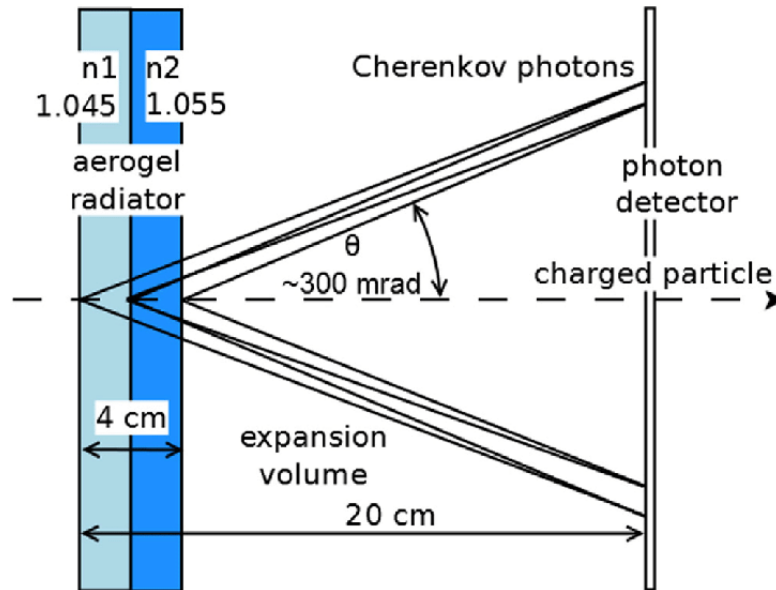


Figure 2.6: Working principle of the ARICH detector.

Particles with the same momentum but different masses radiate at different angles, therefore it is possible to distinguish between them. Two materials with different n_i are used as radiators in order to improve the angular resolution. Photons emitted in the aerogel are detected by a high granularity two dimensional array of single photon detectors.

The Time of Propagation subdetector (TOP) [48] is a special kind of Cherenkov detector, and it is used for particle identification in the barrel region. The calibration of the TOP system is done by the INFN/University groups of Torino and Padova in Italy.

There are 16 TOP modules placed around the barrel; each module consists of a 45 cm wide and 2 cm thick quartz bar, with a small expansion volume (≈ 10 cm long) at the backward sensor end of the bar. At the exit windows of the volume, two rows of sixteen fast multi-anode photon detectors are mounted, while a reflective mirror is accommodated at the forward end of the bar. The quartz works as radiator for Cherenkov photons, which travel via total internal reflection to the mirror, where they are reflected towards the photon detectors at the backward end. A visualization of the internal reflection of the photons is presented in Fig. 2.8, alongside a conceptual overview of the TOP counter Fig. 2.7.

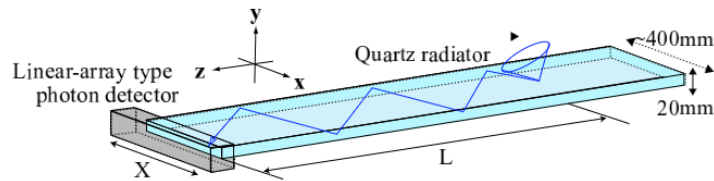


Figure 2.7: Conceptual view of TOP counter. This is only a schematic presentation of the operation, since the TOP installed in Belle II has the photodetector in the backward region and a focusing mirror in the forward region

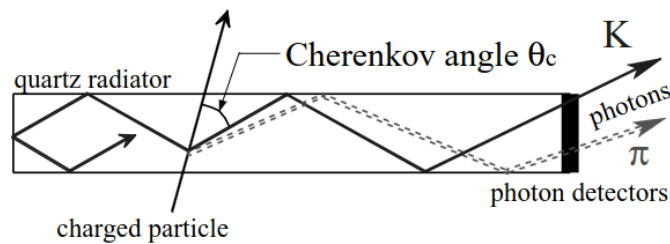


Figure 2.8: Side view of the TOP counter with the internal reflection of the Cherenkov photons visualized

The Cherenkov image is reconstructed using the 3-dimensional information provided by the two (x, y) coordinates and the precise timing of the photon in the detectors at the backward end. For a given track the distribution of the hits will be different according to the particle mass, since different particles emit at different angles, as is visualized in fig 2.8. The location and the recorded time of each Cherenkov photons can be combined together to form a likelihood for a given particle hypothesis, with the most likely particle assigned to the track.

2.2.4 Electromagnetic Calorimeter (ECL)

The Electromagnetic Calorimeter [49] is used to detect gamma rays and to identify electrons from hadrons. It is composed by a highly segmented array of thallium-doped caesium iodide CsI(Tl) projected toward the interaction region of the beams (IR) (as shown in Fig. 2.9). The barrel and the end caps cover around 90% of the solid angle.

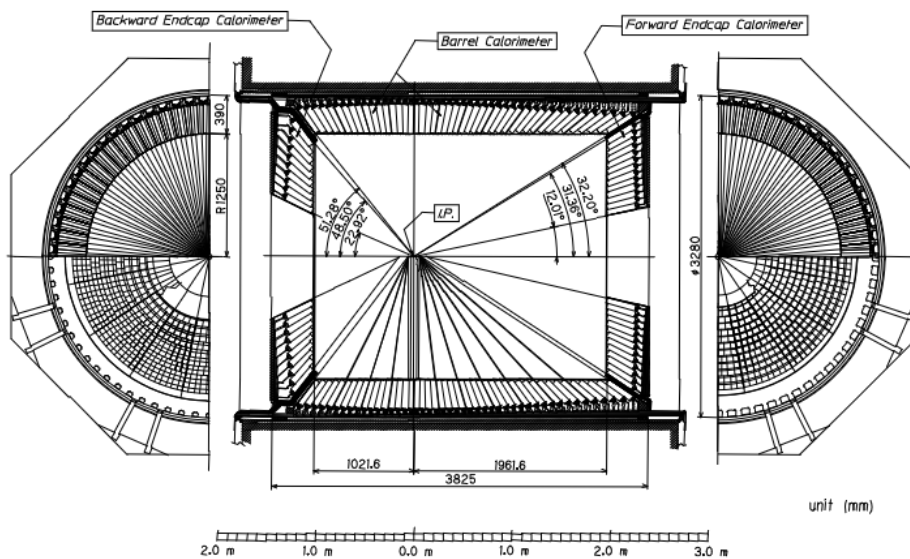


Figure 2.9: Schematic view of the ECL detector.

The light obtained by scintillation in the crystals is detected with two independent sets of photodiodes with a sensitive area of 10 mm^2 connected with a charge sensitive preamplifiers. The CsI(Tl) crystals, preamplifiers and support structures have been in fact reused from Belle, whereas the readout electronics and reconstruction software have been upgraded. In the presence of a considerably large background compared to the operations in Belle, the relatively long scintillation decay of the CsI(Tl) ($1.3 \mu\text{s}$) considerably increases the overlapping impulses from neighbour background events. To mitigate the large pile up of noise, the scintillator photosensors were equipped with wave-form-sampling read-out electronics, in order to discriminate the off-timing hits.

2.2.5 K_L - Muon detector (KLM)

The KLM [50] consists of an alternating sandwich of 4.7 cm thick iron plate and active detector elements located outside the superconductive solenoid. The iron bars serve as magnetic flux return of the solenoid. They also provide 3.9 units of interaction lengths (the mean distance of a particle in a medium before an inelastic process occurs), beyond the 0.8 units of the detector: this allows the K_L to produce hadronic shower inside. The active layers are composed of scintillator strips readout by silicon photomultipliers. A figure of the

2.2.6 Trigger system

The main scope of the trigger system in Belle II is to identify events of interest and to reject background events that are not worth being acquired [43].

The trigger conditions must maintain a high efficiency for interesting physics events and suppress the background. The trigger system in Belle II is composed of two levels, a hardware based low level trigger (L1) and a software based high level trigger (HTL), and represents an upgrade of the existing Belle trigger system. The Belle trigger scheme consists of sub-trigger systems and one final decision logic.

A sub-trigger system summarizes trigger information on its sub-system and sends it to the final-decision logic, which reads the sub-triggers information and issues a positive decision when its criteria are satisfied. In Belle II the general concept is maintained to create the L1 trigger, but all the components are replaced with new technologies. Each component deploy a Field Programmable Gate Array (FPGA), thus the trigger logic is configurable and not hand-wired, and all data flow along high speed serial links, which enable to send a huge amount of information, equivalent of $O(1000)$ channels, to one FPGA. A schematic view of the Belle II L1 trigger is show in Fig. 2.10.

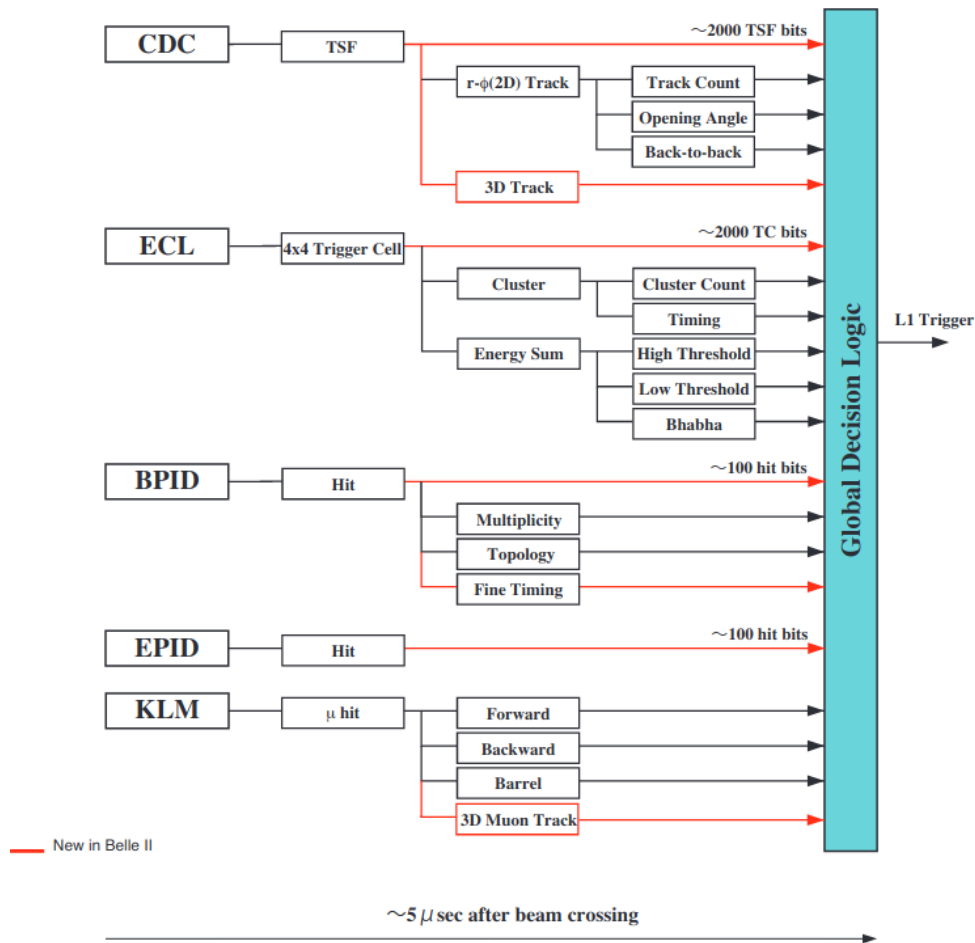


Figure 2.10: Scheme of the Belle II L1 Trigger [43].

The CDC sub-trigger provides the charged track information, such as momentum, position and charge. The ECL sub-trigger gives energy deposit information, energy cluster information, Bhabha events ($e^+e^- \rightarrow e^+e^-$) and cosmic-ray identification. The Barrel PID (BPID) gives precise timing and topology information. Timing information is also provided by the Endcap PID (EPID) sub system. The KLM sub-trigger gives muon track information. The Global Decision Logic receives all the sub trigger information and makes the final decision. The total latency in the trigger subsystem is about $5\mu s$.

The HLT consists of multiple units of PC clusters, that perform a full reconstruction of the event data from all the detectors. The software trigger for the events uses the basf2 framework to perform a reconstruction of the event to a physics level. It has the aim of reducing the trigger rate to a storable rate and assigning the skim flags, a set of selections for specific analysis (e.g the *hadronic* tag from the HLT selects events in which a hadronic final state is produced, thus excluding Bhabha or $e^+e^- \rightarrow \mu^+\mu^-$ events).

2.3 Software

The first step to perform analysis of the data is the reconstruction of the events. This means that the information coming from the various sub-detectors are combined to form particle candidates. Once the events are reconstructed, the more specific steps of the analysis, like making histograms or fitting distributions, can be done via C++ macros or Python scripts. To study the behaviour of both signal and background, Monte Carlo simulations (MC) are performed to reproduce the physical processes that occur both in the e^+e^- collisions and in the propagation of the particles through the detector.

The basf2 software, i.e. the main tool for decay reconstruction and event selection, is described in section 2.3.1, the Monte Carlo generation is described section 4, the reconstruction process, alongside the tracking system and the particle identification, is described in section 2.3.3.

2.3.1 basf2

The Belle II software is called basf2, which stands for "Belle II Analysis Software Framework" [51]. basf2 is mainly used for generating simulated data, unpacking raw data, reconstruction (e.g. tracking or vertex fitting).

In basf2 a typical data processing chain consists of a linear arrangement of smaller blocks, called "Modules". Modules are small blocks of code written in C++, that can perform simple tasks like reading data from a file or more complex ones, like full detector simulation or tracking. Each module is arranged in a "Path" in a strict linear order. The specific selection and arrangement of modules depends on the task. When processing data, the framework executes the modules of the path one at a time, starting with the first one and proceeding with the next one, in the order in which they were placed. The data to be processed by the modules is stored in the DataStore, a common storage to which each module has read and write access to. Non-event data, the so called conditions, are loaded from a central conditions database and are available in the DBStore. These database mainly stores the information about the detector conditions at any run of the experiment (hence the name). The basf2 software has an interface with python3, therefore the data processing can be performed with python3 scripts, called steering files. A typical steering file declare a Path, configure basf2 modules and then add them to the path. The path is then processed and the modules are executed. In Fig. 2.11 the scheme of the processing flow in a steering file is shown.

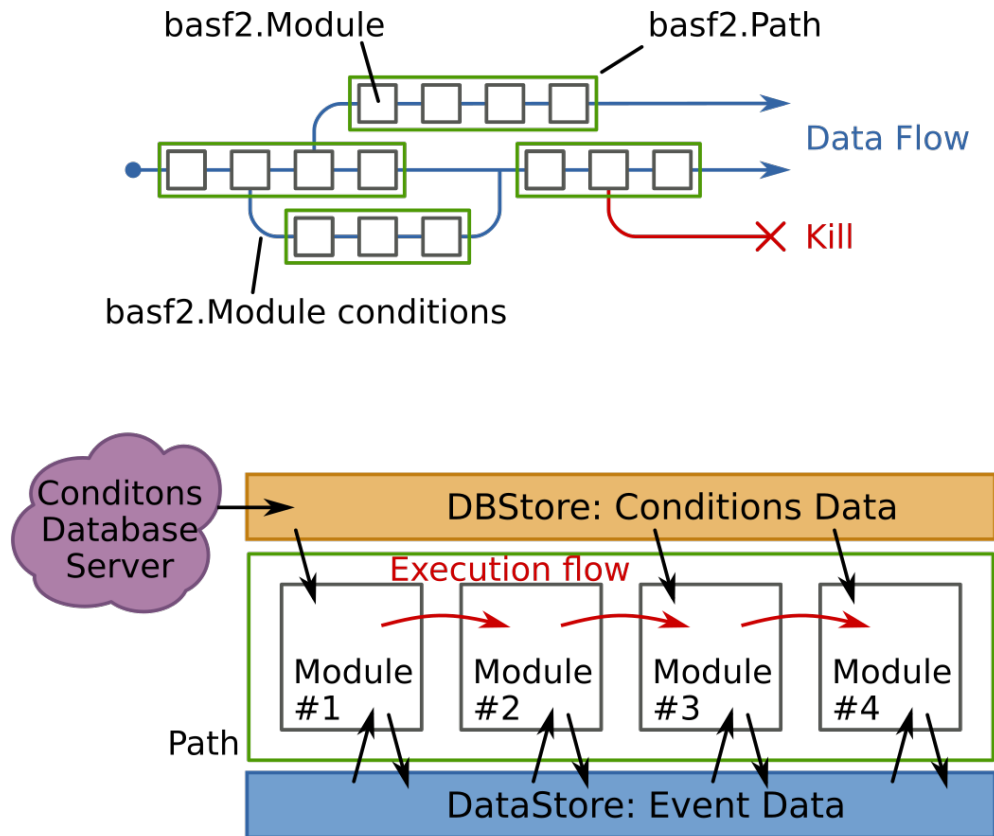


Figure 2.11: Schematic view of the processing flow in the Belle II Software.

2.3.2 Monte Carlo simulation

Monte Carlo (MC) simulations are used to create simulated events of specific physical processes and to study how the detector responds to them. The MC procedure is divided into two steps: the generation of the events, which concerns the production and the decays of particles with specific properties, and the simulation of the passage of the particles in the detector materials. During the generation of the event, given the initial conditions of the electron and positron collision, a number of particles are generated according to the physical models in study, that could follow either the Standard Model or more advanced ones, like super symmetry models or dark matter production. The positions and four-vectors of the particles of the event can be obtained with a large variety of generators optimized for different uses. Example of generators are EvtGen for B and D decays, MadGraph for SM (Standard Model) and BSM (Beyond Standard Model) processes, PHOKARA for leptonic and hadronic final states with and without ISR and so forth.

Once the particles are generated, the next step is to simulate their propagation into the detector. This means to simulate the interaction of the particles with both the sub-detector active regions and the structures of the detector; this interactions can come from various processes like ionisation, multiple scattering, Cherenkov radiation, scintillation and so forth. All these process are simulated using the software Geant4 [52]. Geant4 is an open source software published in 2003, used to

describe the interaction between particles and the detector systems. The materials of the detectors are specified by their physical features, like atomic and mass number, density and radiation length, and they are given as input parameters to the program. The probability of each process, like ionization or pair production, must be coded into the program, and random MC methods are used to decide what kind of interaction occurs at each step of the simulation of the particle propagation.

2.3.3 Reconstruction

The reconstruction process involves the identification of the particles from the information obtained in all the sub-detectors. The main task of the reconstruction is to identify the particle as correctly as possible and get the original four-vector as it was produced in the interaction. However, not all the particles can be reconstructed directly, since most of the products of the e^+e^- are short living particles that decay before reaching the detector, hence they have to be reconstructed from their daughter particles. Every detector has intrinsic noise, that leads to some channels to register a signal even without the presence of a real particle. In addition to noise background, physical background, like the one coming from interaction of the particles with the accelerator structure, can lead to hits not related to the events of interest.

The reconstruction process looks at the detector response in each event and find a set of most likely particles. The same algorithms are used in data and MC to obtain the exact same reconstruction for the two type of events; however, since in the MC the properties of the particles and their hits on the sub detectors are known, one can trace the correctness of the reconstruction by looking at what is called the *MCTruth*.

The reconstruction involves three main steps: the clustering, the tracking and the particle identification, as it follows.

Clustering

The clustering process involves the combination of the detector responses in each sub detector if they are related to the same particles. For example, a particle crossing the PXD should leave a signal in just one of the pixel, but it could hit the boundaries of the pixels or hit several of them, if it crosses the sub detector at a shallow angle. To account for this effect, neighbour pixels are clustered together and properties such as the size, shape or center of the cluster can be calculated. An example to illustrate the clustering in the PXD is shown in Fig. 2.12.

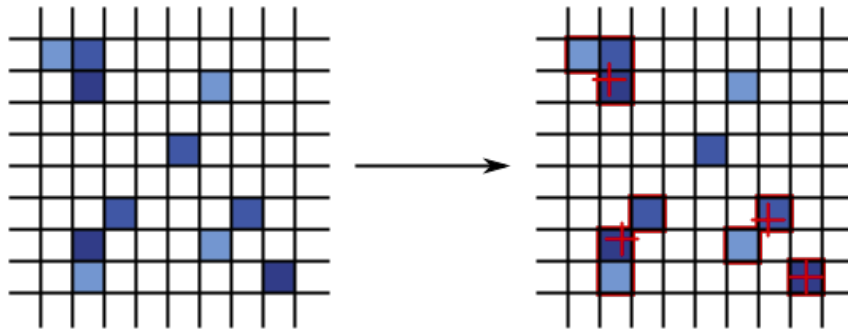


Figure 2.12: Simple example of 2D clustering in the PXD detector.

This principle is also used in the SVD for each of the 1D side and in the ECL. However, the ECL clustering needs to take into account the different shapes of the cluster depending on which particle created the shower, being a hadronic interaction or a photon.

Tracking

The tracking process involves the identification of the particle trajectories and is performed using the responses of the VXD and CDC sub detectors. The xyz coordinate system used in the tracking is defined as it follows:

- z axis, taken to be anti-parallel to the LER momentum vector;
- y axis, pointing to the vertically upward direction;
- x axis, pointing horizontally to complete a right handed system.

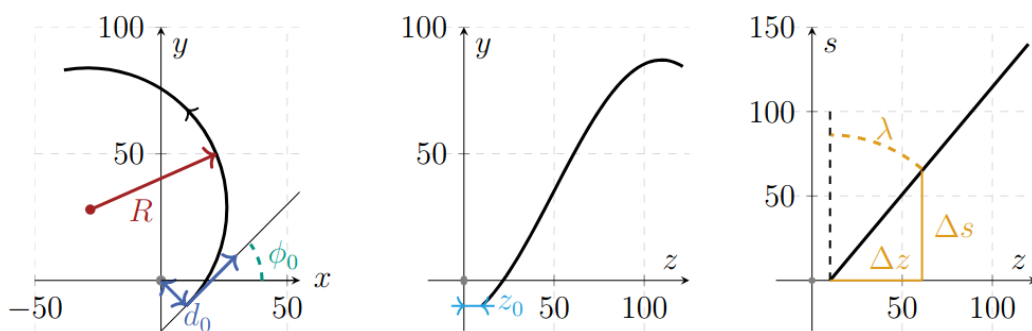


Figure 2.13: Schematic representation of the track trajectory in the $x - y$ (left), $z - y$ (middle) and $z - s$ (right) projections. Dimensions are in cm. The definition of the variables is reported in the text. The radius of the track R is the inverse of the absolute value of the track curvature ω .

The particle trajectories are represented locally using the helix parametrization, as shown in Fig. 2.13; the total number of parameters is five. Three out of the five parameters are in the $x - y$ plane:

- d_0 : the signed distance of the point of closest approach (POCA) to the z axis;
- ϕ_0 : the angle defined by the x axis and the track transverse momentum at the POCA;
- ω : the track curvature signed with the particle charge.

The helix can be represented as a straight line in the $s - z$ plane, with s being the path length along the circular trajectory in the $x - y$ projection. The two corresponding parameters are:

- z_0 : the z coordinate at d_0 ;
- $\tan \lambda$: the slope of the track.

An in-depth discussion of the tracking system in Belle II is presented in this report [53], here only the general procedure will be discussed.

The first step of the track reconstruction is the filtering and reconstruction of the signal measured in the CDC. The results are merged and the CDC-only tracks are fitted. A combinatorial Kalman filter (CKF) is used to extend the CDC tracks with SVD hits. High curvature tracks (low transverse momentum) that did not produce enough hits in the CDC are reconstructed with a standalone track finder using only the hits in the SVD. The final step after the track finding consists of the track fit using the deterministic annealing filter (DAF) provided by GENFIT2 [54]. The results of the fit are stored to be used in physics analyses.

Particle Identification

The PID in Belle II is performed differently for charged and neutral particles, and it is based on likelihood ratio.

The sub-detectors mainly involved in the PID for charged particles are the TOP and the ARICH. Information from these sub-detectors is combined with the one from specific ionization (dE/dx) obtained from the CDC to act as the primary sources of information for charged hadron PID. In a similar way, the ECL provides the primary information to use in electron identification and the KLM provide the one for muon identification.

First the PID log likelihood from each detector are summed to create a combined PID likelihood for each of the six long-lived charged particle hypotheses: electron, muon, pion, kaon, proton and deuteron. The difference in log likelihood between two particle hypotheses is used to construct a PID value $L(\alpha : \beta)$ according to:

$$\mathcal{L}(\alpha : \beta) = \frac{1}{1 + e^{\ln \mathcal{L}_\alpha - \ln \mathcal{L}_\beta}} = \frac{\prod_{det} \mathcal{L}(\alpha)}{\prod_{det} \mathcal{L}(\alpha) + \prod_{det} \mathcal{L}(\beta)} \quad (2.1)$$

where α and β represents the two different particle types and the product is done over the detectors used for the PID of interest. The value of $L(\alpha : \beta)$ is greater than 0.5 for a charged particle resembling more a type α particle, while is less than 0.5 if resembling more a type β particles.

Neutral particle identification involves the identification of photons, π_0 and K_L^0 . The identification of photons in the ECL is based on the shape of the shower in the ECL clusters not matched to reconstructed tracks (therefore rejecting charged particles). The identification relies on the fact that the electromagnetic showers caused by an incident photon is cylindrically symmetric and the energy deposition decrease exponentially with the distance to the incident axis. Neutral or charged hadrons, which are the main background for photon identification, create asymmetric shower shapes instead. The reconstruction of π_0 in the decay mode $\pi_0 \rightarrow \gamma\gamma$ is based on the combination of two photon candidates. The angle separation of the two photons decreases as the energy of the π_0 grows, thus making them harder to distinguish as separate clusters in the ECL. π_0 energies below ~ 2.5 GeV can be reconstructed as two separate photon candidates in the ECL, while for π_0 energies above this threshold, the two photon induced showers cannot be separated and are reconstructed as a single photon candidate. The π_0 reconstruction is also improved by performing a mass constrained fit of the two photon candidates to the π_0 mass.

The identification of K_L^0 is based on information collected on the KLM and the ECL detector, using a multivariate method to classify ECL and KLM clusters. The largest contribution to the backgrounds are from neutrons and photons originating from beam interactions with detector or beam-pipe material.

Chapter 3

Analysis outline

This analysis will focus on the process $Y(10753) \rightarrow \pi^+\pi^-h_b(1P)$, using data taken at the four point of the Belle II scan around the $Y(10753)$. This transition is expected to be greatly suppressed by both the OZI rule and by HQSS, since passing from a triplet states to a singlet state would require a spin flip of the heavy quark.

Di-pion transitions have been however observed with very large partial width from both the $\Upsilon(5S)$ and $\Upsilon(6S)$. This apparent strong violation of the aforementioned selection rules has been explained by the action of intermediate charged states, the $Z_b(10610)$ and $Z_b(10650)$, as discussed in sec. 1.3. Instead of having a three-body decay, the dipion transitions proceed dominantly as a cascade of two-body processes: $Y(10753) \rightarrow \pi^{-(+)}Z_b^{+(-)} \rightarrow \pi^{-(+)}\pi^{+(-)}h_b(1P)$. Since the Z_b should present both a spin singlet and a spin triplet component with equal amplitudes [27], the single pion decay is not affected by the spin flip suppression.

The $Y(10753)$ is particularly interesting in this regard, as it is located across the $\pi Z_b(10610)$ threshold: the measurement of the $e^+e^- \rightarrow \pi^+\pi^-h_b(1P)$ cross section as a function of the energy allows to study if the transition through the $\pi Z_b(10610)$ is present or not. Indeed, if the decay is mediated by the Z_b a signal is expected in the recoil spectrum of the single pions; if the transition is not found, measuring the cross section or the branching ratio could instead validate the presence of an intermediate state. While the phase space transition, without any intermediate resonance, is kinematically allowed at all the four energy points, only the one at 10805 MeV has enough phase space to allow the single pion transition to the Z_b , since the third point, which is the closest to the resonance, is 5 MeV below the cinematic threshold for $e^+e^- \rightarrow \pi Z_b(10610)$.

The decay chain of $Y(10753) \rightarrow \pi\pi h_b(1P)$ is illustrated in Fig. 4.6.

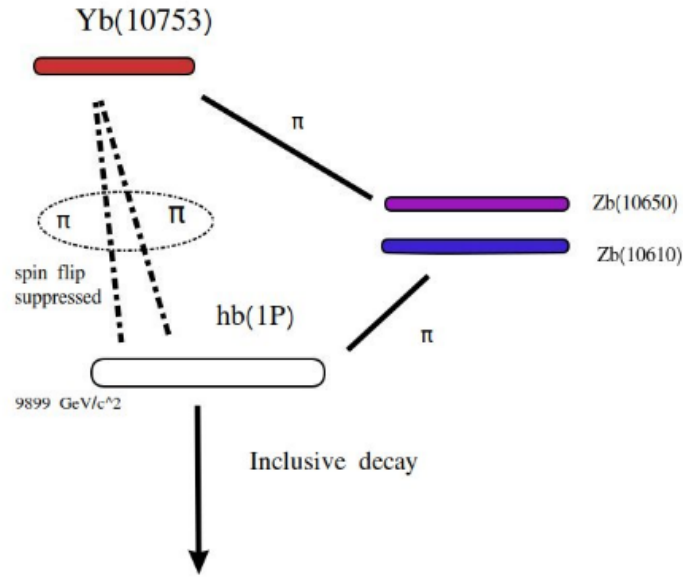


Figure 3.1: Decay of the $Y(10753) \rightarrow \pi\pi h_b(1P)$.

The $h_b(1P)$ decays mainly to $\eta_b(1S)$ via radiative transition, with the η_b decaying into lighter hadrons. Since an exclusive reconstruction of the $h_b(1P)$ would require the reconstruction of the η_b through a large number of processes with small branching ratios, an inclusive strategy will be performed by looking at the missing mass of the dipion from the $e^+e^- \rightarrow \pi^+\pi^-h_b(1P)$. This variable is defined as $M_{miss}(\pi\pi) = \sqrt{(E_{cm} - E_{\pi\pi}^*)^2 - p_{\pi\pi}^{*2}}$ (where $E_{c.m.}$ is the center of mass (c.m.) energy, $E_{\pi\pi}^*$ and $p_{\pi\pi}^*$ are respectively the energy and the momentum of the pion pair in the c.m.) and is peaking at the $h_b(1P)$ mass for the signal.

A blind analysis will be performed, therefore the signal region on data will not be inspected until all cuts for the selection are chosen and the systematic uncertainties are under control. Cuts will be studied with Monte Carlo simulated events (MC). The used samples are discussed in the following section.

3.1 Monte Carlo samples

The signal is generated as a phase space transition from the $Y(10753)$ to $h_b(1P)$ via the pion pair. The number of generated events is not an input of the simulation, but the MC uses the luminosity at each point to generate the number of events accordingly. A total amount of 37516 events was generated at the four energy points as listed in Table 3.1.

Process	Luminosity (fb^{-1})	Number of events
10657	3.5	6257
10706	1.6	926
10745	9.8	19007
10805	4.7	11326
Total	19.6	37516

Table 3.1: Number of $e^+e^- \rightarrow \pi\pi h_b(1P)$ events produced in the signal sample, for each energy.

Since the luminosity of the second points is roughly half of the first, one should expect also the ratio of the number of events to be close to 0.5, since the phase space transition should not be affected by the \sqrt{s} , as long as the phase space is enough. However, the number of events at 10706 MeV is around one third of the expected amount. The cause of this is ascribed to the simulation process, however since the analysis will be performed with the four samples unified, the lower counts at 10706 MeV will not affect the results. In this analysis this sample will be referred as the *signal MC* sample.

A sample of $e^+e^- \rightarrow \pi^\pm Z_b(10610)^\mp$ is also generated in order to investigate the behaviour of the signal with the intermediate transition to the $Z_b(10610)$. Both $e^+e^- \rightarrow \pi^\pm Z_b(10610)^\mp$ and $Z_b(10610)^\pm \rightarrow \pi^\mp$ decay are generated via phase space transitions. Since the decay is kinematically forbidden for all the energies but the point at 10805 MeV, this events will be generated only for the latter energy. In this analysis this sample will be referred as the *Z_b signal MC*.

The background is simulated with a sample containing events from the most common processes that occur in the e^+e^- collisions at these energies, as listed in Table 3.2.

Process	Luminosity (fb^{-1})
$e^+e^- \rightarrow (q\bar{q}(q = d, u, s, c))$	76.525
$e^+e^- \rightarrow ee$	1.913
$e^+e^- \rightarrow \mu\mu$	76.525
$e^+e^- \rightarrow \tau\tau$	76.525
$e^+e^- \rightarrow ee\mu\mu$	19.131
$e^+e^- \rightarrow eeee$	19.131
$e^+e^- \rightarrow llXX$	19.131
$e^+e^- \rightarrow hhISR$	19.131
$e^+e^- \rightarrow gg$	8.262
$e^+e^- \rightarrow B\bar{B}$	76.525

Table 3.2: Luminosity for each process of the BG.

Events are generated at the four energies of the Belle II scan, namely at 10657, 10705, 10745 and 10805 MeV.

Beam background, i.e. the events that come from secondary interactions of the beam particles in the pipe, like beam-gas scattering or synchrotron radiation, is also simulated for each event in every sample.

3.2 Selection of tracks

The first selection requires the events to pass the Level 1 Trigger and to be tagged as hadronic by the HLT trigger. This selection has an efficiency close to 100 %, as studied in other analyses, and does not compromise the signal yield.

A second selection is performed in order to remove tracks coming from the beam background or wrongly reconstructed by the tracking system. While the signal events should be produced close to the interaction point (IP), the "bad" tracks have a much broader distribution of their POCA to the IP, and this will be used to discriminate them.

The cuts are explained in details in section 4.2, the efficiency will be measured on generic MC as a function of the transverse momentum of the track (p_t) and will be compared to the value on data, measured with a control channel.

3.3 Continuum Suppression

A significant amount of background comes from $e^+e^- \rightarrow q\bar{q}$ events. These events create multiple streams of particles in the detector. These streams are called *jets* and present a topology quite different from the $e^+e^- \rightarrow Y(10753)$ events. In fact, since the $h_b(1P)$ has a large mass, it is produced nearly in the rest frame. Therefore, the final state of its decay chain has a more spherical distribution in the detector, when compared to jet events. Indeed, this is true also for $e^+e^- \rightarrow B\bar{B}$ events, since the B mesons are heavy particles with small boost in the laboratory frame. This kind of events is usually called *central events*, and their topology, in comparison to jets, is illustrated in Fig 3.2. A multi variate analysis will be performed in order to suppress events from continuum, using selections on event topology.

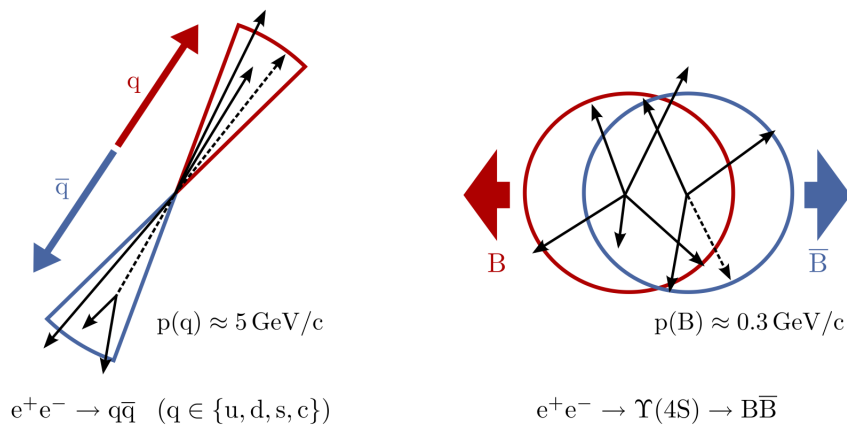


Figure 3.2: Topology for jet and central events.

3.4 Fit on signal

Once the cuts are chosen, fit on the distributions of the missing mass of the dipions $M_{miss}(\pi\pi)$ will be performed at each energy, to obtain the signal yield. Events will be weighted before fitting to account for the efficiency of the reconstruction and selections. The signal yields will be used to measure the cross section of the process or to make an esteem of the upper limits if no evidence for signal will be found on data.

Chapter 4

Studies on Monte Carlo

4.1 Signal shape

In this section a study of the signal for both the $e^+e^- \rightarrow \pi\pi h_b(1P)$ and $e^+e^- \rightarrow \pi Z_b \rightarrow \pi\pi h_b(1P)$ processes will be presented. Distribution of the momentum of the tracks and $M_{miss}(\pi\pi)$ will be shown alongside an esteem of the acceptance for each energy.

4.1.1 Study of the signal for the phase space transition

The $e^+e^- \rightarrow \pi\pi h_b(1P)$ process is kinematically permitted at all the four energies of the scan. While, without intermediate resonances, this process is expected to be suppressed according to the HQSS, this is the only process that allows us to study the production of the $h_b(1P)$ for all the four energy points.

In the following we will call *signal pions* the pions coming from the $Y(10753)$ transitions, in contrast to the pions which come from the $h_b(1P)$ decays. The momentum distribution for the reconstructed signal pions at the four energies is shown in Fig. 4.1.

A structure at low momentum is found for all the energies. This effect is due to events with ISR, in which a photon is emitted by the e^+ or the e^- before the collision, thus lowering the \sqrt{s} of the process.

This leads to a different kinematic of the pions, as one can see in the Fig. 4.2, where the dipion momentum distribution is shown for signal events excluding ISR processes.

Since the energy of the photons from ISR has a continuous distribution, the \sqrt{s} of the event is not fixed anymore by the beam energy, therefore the pion momentum distribution from ISR events must account for three body decays at different energies lower than nominal \sqrt{s} . This leads to events with both tracks in regions of p that otherwise would be kinematically forbidden.

Events without ISR are instead produced with fixed \sqrt{s} and their kinematic is constrained in a limited region, as one can see in Fig. 4.2.

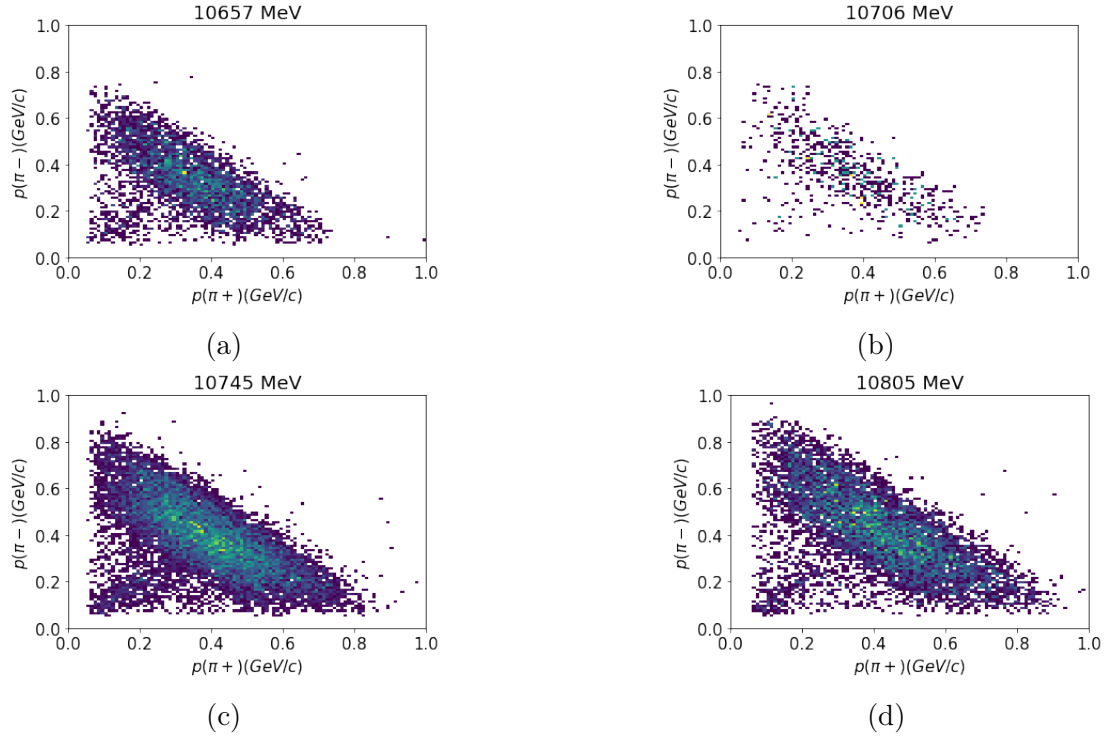


Figure 4.1: Two dimensional distribution of the signal pion momenta in the laboratory frame, at different energy points.

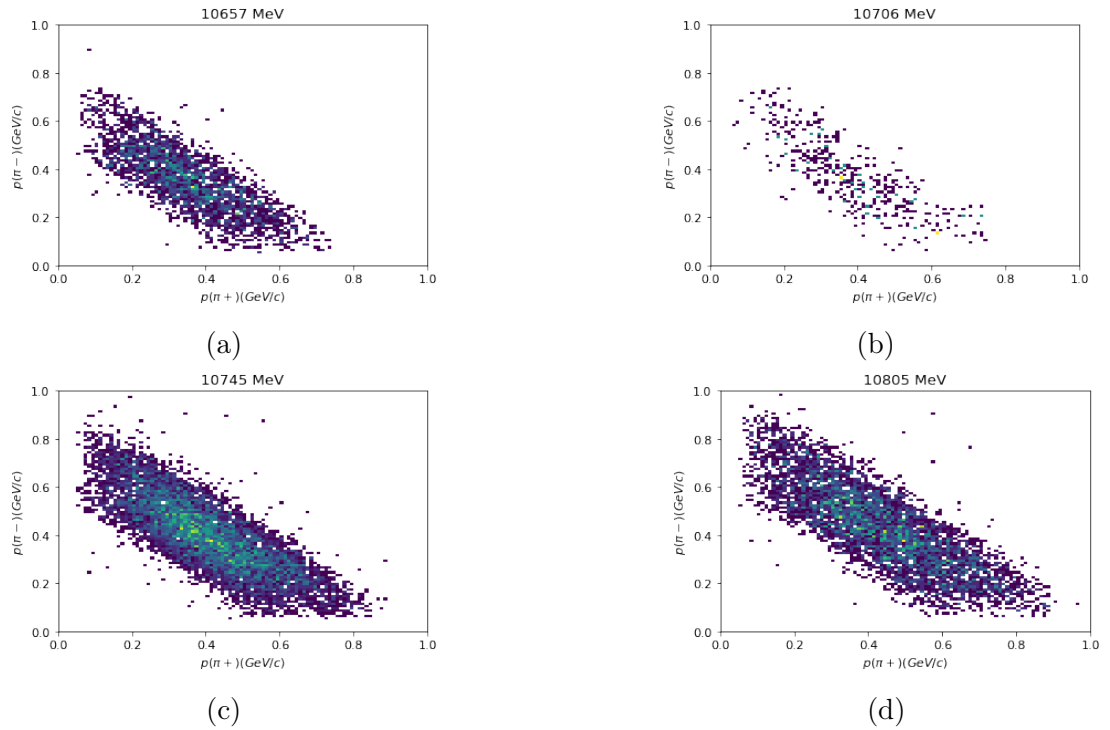


Figure 4.2: Distribution of dipion momenta for events without ISR.

The distribution of the reconstructed $M_{miss}(\pi^+\pi^-)$ from $e^+e^- \rightarrow h_b(1P)$ is shown in Fig. 4.3. Since in real data we cannot distinguish between pions from

the $h_b(1P)$ recoil and pions from the $h_b(1P)$ decay, the missing mass distribution is affected also by pairs when one or both of the pions are not the ones of the signal. While the combinatorial BG creates a uniform distribution, the signal pairs shows a clear peak at the $h_b(1P)$ mass.

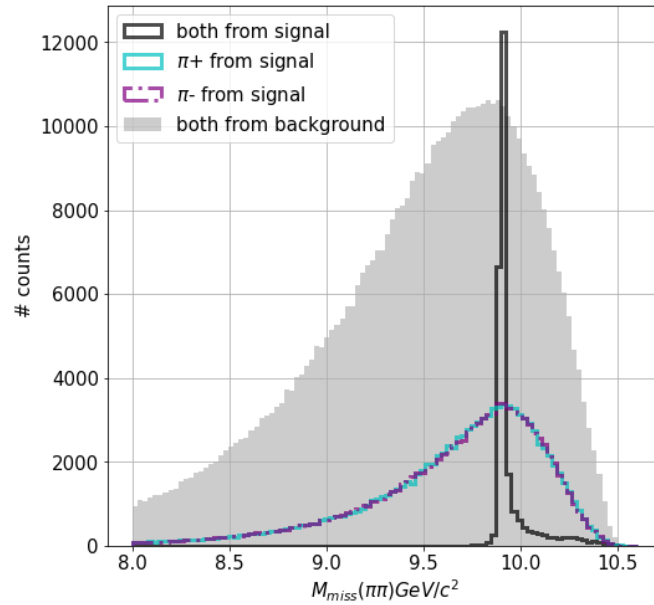


Figure 4.3: Distribution of $M_{miss}(\pi\pi)$ with the different pion pair combinations. The narrow distribution in black come from the signal events. Large distribution in gray comes from background tracks, namely from the decay of the h_b or from beam background. Blue and purple lines represent the distributions of candidates in which one of the pion comes from the signal and the other from the background.

Distribution of the $M_{miss}(\pi\pi)$ of the reconstructed candidates with BG is shown in 4.4, separately for each energy:

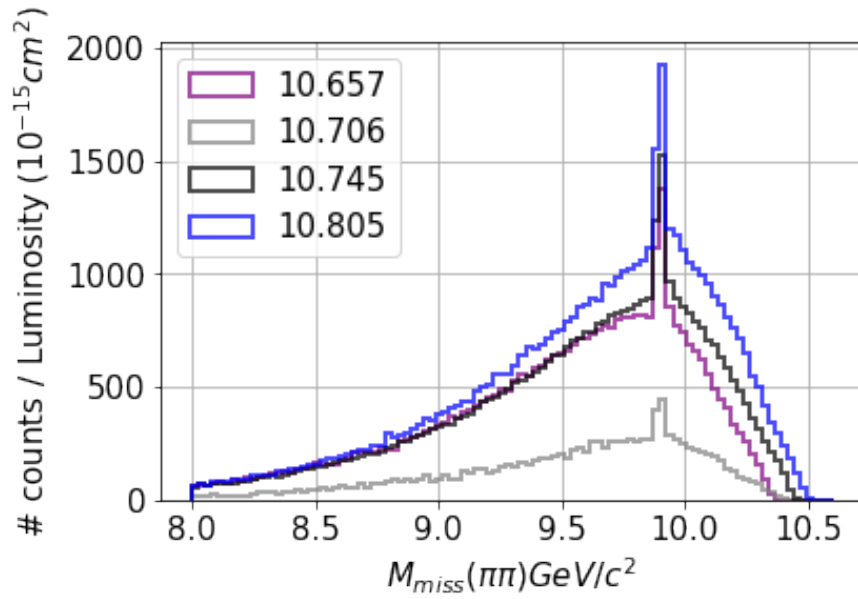


Figure 4.4: Distribution of $M_{miss}(\pi\pi)$ weighted by luminosity, for each energy point. The signal peak is located at the $h_b(1P)$ mass region ($9.9 \text{ GeV}/c^2$).

The low number of events at 10706 MeV compared to the other points was already discussed. No other discrepancy are found in the distribution, as one would expect since the phase space should only shift the kinematic limit of the $M_{miss}(\pi\pi)$, without altering the general shape of both signal and combinatorial background.

The acceptance of the signal events is defined as:

$$acceptance = \frac{N_{reconstructed}}{N_{produced}} \quad (4.1)$$

where $N_{reconstructed}$ is the number of events obtained after reconstruction of the MC simulation through the analysis framework and $N_{produced}$ is the number of events as generated in the MC.

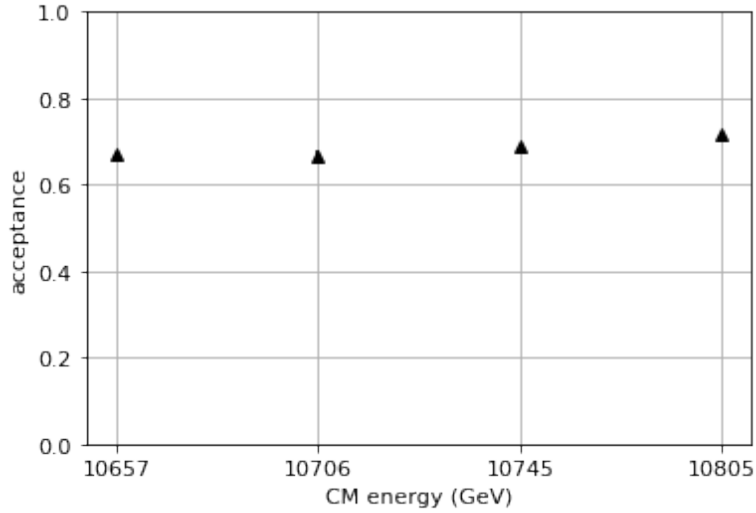


Figure 4.5: Acceptance of the dipion from $e^+e^- \rightarrow \pi\pi h_b$ at the four energies.

Value of acceptance for each energy are reported in Table 4.1 and shown in Fig. 4.10.

Energy (MeV)	Acceptance
10657	0.669 ± 0.005
10706	0.666 ± 0.015
10746	0.691 ± 0.003
10805	0.716 ± 0.004

Table 4.1: Acceptance of the dipion from $e^+e^- \rightarrow \pi\pi h_b(1P)$ at the four energies.

The acceptance increases with the energy; this effect is expected since a higher Q value of the transition leads to more energetic pions, and since tracking efficiency grows with the particle momentum, this means that a higher number of them is correctly reconstructed.

4.1.2 Study of the signal for the Z_b mediated transition

At the most energetic point at 10805 MeV the transition through both states of the Z_b is allowed. At this energy, the Q value of the decay to the $Z_b(10610)$ is 65 MeV, while the transition to the $Z_b(10650)$ has a Q value of just 15 MeV, as one can see in the illustration of the decay chain in Fig. 4.6.

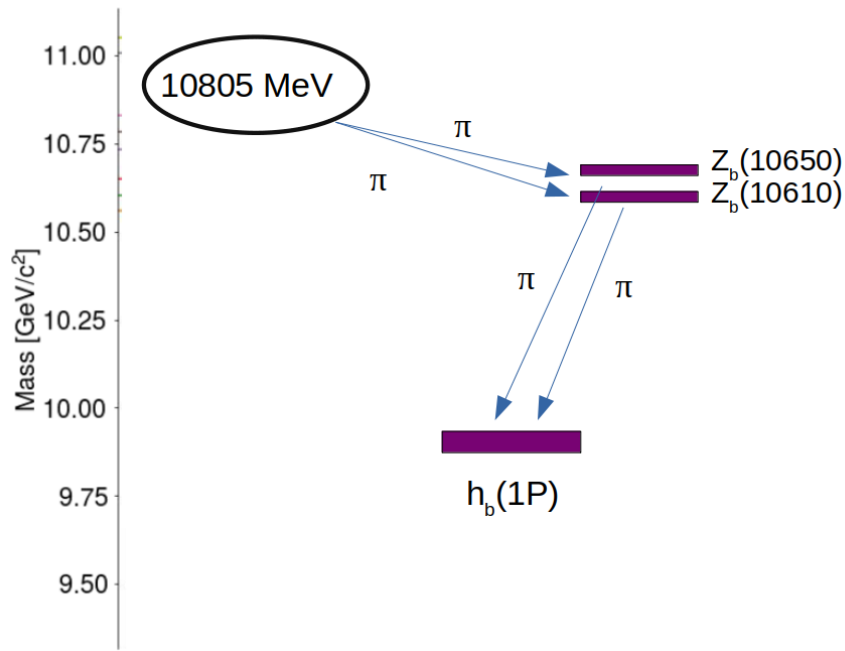


Figure 4.6: Decay chain of $e^+e^-(\sqrt{s} = 10805) \rightarrow \pi Z_b(10610)/(Z_b(10650)) \rightarrow \pi\pi h_b(1P)$.

The pion tracks from the decay to the $Z_b(10650)$ will be affected by a low reconstruction efficiency, since low momentum (soft) tracks rarely reach the CDC and must rely only on the SVD for the tracking. Due to its limited phase space, the $e^+e^- \rightarrow \pi Z_b(10650)$ channel will not be investigated with MC simulation.

The $e^+e^- \rightarrow \pi Z_b(10610) \rightarrow \pi\pi h_b(1P)$ decay, conversely, is hereby studied, in order to understand the behaviour of the signal in this specific case.

The MC sample consists of around 15k events of $e^+e^- \rightarrow \pi Z_b(10610) \rightarrow \pi\pi h_b(1P)$ events, with simulation of the beam background.

The distribution of the momentum of the pions involved in the decay is shown in Fig. 4.7.

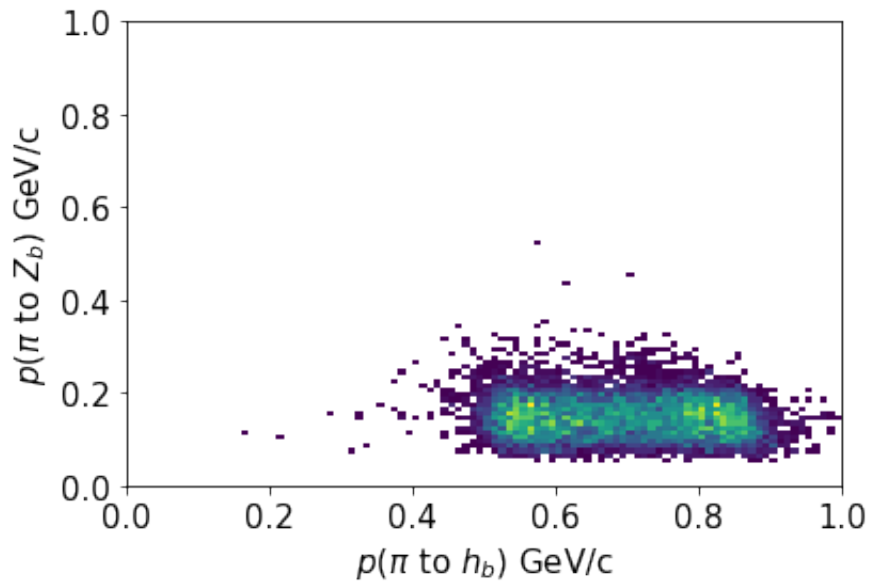


Figure 4.7: Distribution of the momentum of the signal pions from the $Z_b(10610)$ mediated transition.

There is a clear asymmetry on the distribution of the two tracks momentum; this is expected since the decay from the $Z_b(10610)$ to the $h_b(1P)$ has a much larger phase space compared to the $e^+e^- \rightarrow \pi Z_b(10610)$ process at 10805 MeV, as can be seen in the Fig. 4.6. Thus, for the purpose of this discussion, the pion from the Z_b will be labelled as the *hard pion* and the one to the Z_b as the *soft pion*.

The distribution of the M_{miss} is shown in Fig. 4.8

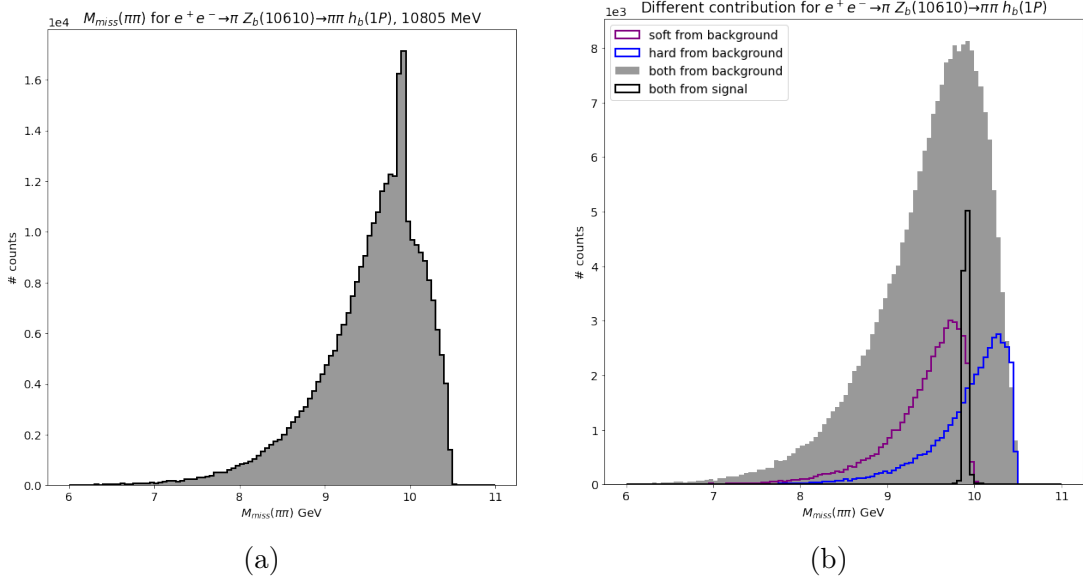


Figure 4.8: (a) Distribution of the $M_{miss}(\pi\pi)$ for the $Z_b(10610)$ transition. (b) Distribution of the different contributions: grey distribution for both tracks coming from background, either beam background or $h_b(1P)$ decay; black line for both signal tracks correctly reconstructed; blue line for candidates with the hard pion reconstructed and the soft pion coming from background; purple line for events with soft pion correctly reconstructed and hard pion from background.

The kinematic of this decay produces an asymmetric threshold effect in proximity of the $h_b(1P)$ mass, due to the soft pion being already at limit of the phase space; therefore, a pion from the background cannot have much less energy than the soft pion from the signal. Thus the kinematic limit of the M_{miss} of a hard pion from the signal and a random pion from the backgrounds is at the $h_b(1P)$ mass value.

The acceptance of the signal, defined in the same way as Eq. 4.1, is reported in Table 4.2.

Energy (MeV)	Acceptance for the Z_b channel
10805	0.618 ± 0.004

Table 4.2: Acceptance for $e^+e^- \rightarrow \pi Z_b(10610) \rightarrow \pi\pi h_b(1P)$ at $\sqrt{s} = 10805$ MeV.

The acceptance for the Z_b channel is around 10% lower than for the phase space transition. This is expected since low momentum tracks, as the one involved in the decay to the Z_b , are harder to reconstruct in the detector.

While the transition through the $Z_b(10610)$ could be possible at 10805 MeV, this point is 60 MeV off resonance. The $Y(10753)$ has a width of around 35 MeV, so the cross section is expected to decrease when moving far from the resonance. Therefore, this transition is not expected to play a relevant role for the $e^+e^- \rightarrow \pi\pi h_b(1P)$, and all the simulations will be done using the phase space events a signal sample. However, while focusing the analysis on the phase space transition, particular care will still be taken when treating low energy pions, since they play a crucial role in the Z_b production.

4.2 tracks selection

The next step of the analysis is to choose a set of cuts to reject the bad tracks, namely the ones coming from the beam background and the fakes (created by wrong combinations by the pattern recognition) or clones (reconstructed using hits from different particles). The generic MC sample was used to inspect the distributions of three variables for the background events:

- dr : the radial distance of the point of closest approach (POCA) of the track to the IP;
- dz : axial distance of the point of closest approach (POCA) of the track to the IP;
- $nSVDHits$: number of hits of the tracks in the SVD.

Since tracks from beam background do not necessary comes from the IP, dr and dz are inspected to see how background differs from the signal in regard of the POCA position distributions. The number of SVD hits was chosen as a cut variable since most of the real tracks will leave a signal in all the four layers of SVD, while Beam background tracks will be stopped before reaching the last layer of the SVD, since due to their low momentum they will either be absorbed in the material or keep curling in the magnetic field.

A similar discussion can be made for the fake tracks. Since they are not produced at the IP, they can have a broader distribution in terms of dr and dz , or they could miss some SVD layer and have a fewer amount of SVD hits.

4.2.1 Comparison between data and MC

The reliability of the generic MC is checked by looking at the distributions of these three variables in MC and data, as shown in Fig. 4.9 and 4.10. Data events come from the samples taken at the four energy scan, while generated events come from the generic MC sample.

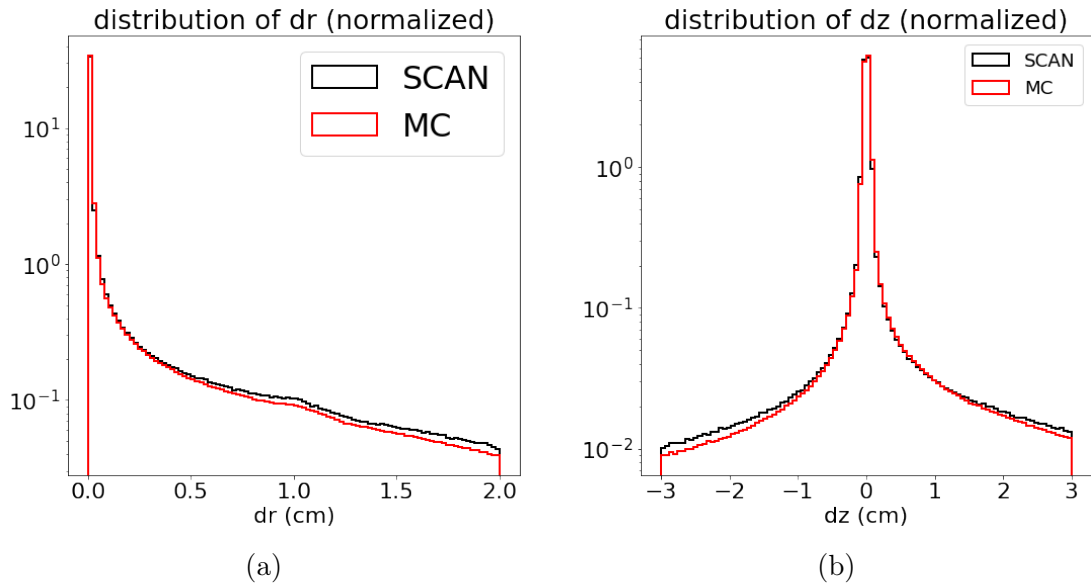


Figure 4.9: Distributions of dz and dr for data (black) and MC (red), normalized to one.

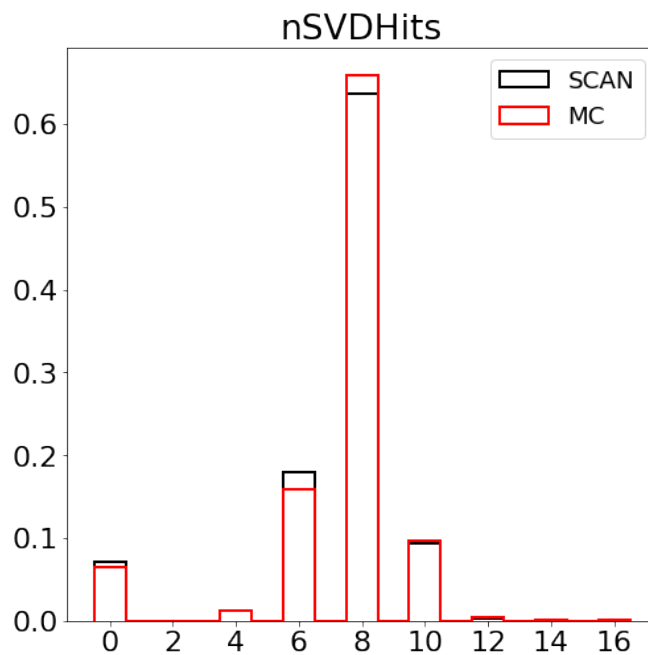


Figure 4.10: Distribution of $nSVDHits$ for data (black) and MC (red), normalized to one.

There is a good agreement between the data and MC samples; the next step is to confront the shape of signal and background events.

4.2.2 cuts selection

Distributions of dr , dz , and $nSVDHits$ are reported in Fig. 4.11 for signal MC tracks and background tracks extracted from the generic MC. Background tracks

are identified with at least one of the two conditions below:

- not matched with a generated MC particle: this select beam background and fake tracks;
- assigned to multiple candidates: this select clone tracks.

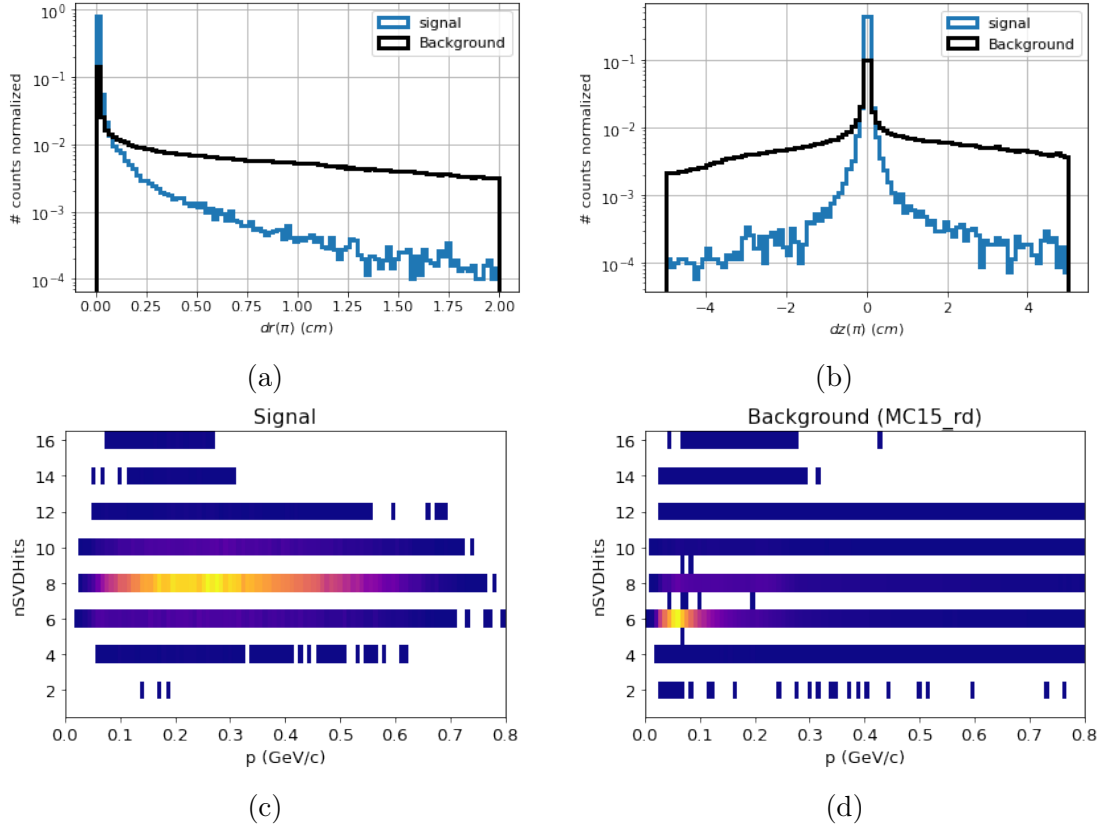


Figure 4.11: Distributions of dr (a), dz (b) (both normalized to one) and $nSVDHits$ vs p , for signal (c) and background (d) tracks.

Signal events are produced extremely close to the IP and their tracks are mostly correctly reconstructed, while background tracks have a much broader distribution compared to signal in terms of dr and dz .

Figure 4.11d shows that background tracks are mainly found in a region of low momentum with six hits on the SVD. This exact number is due to the fact that most of the background tracks do not reach the last layer of the SVD, thus leaving a signal in just three of them (a hit on the SVD is composed by two signals in each layer of the SVD, as explained in 2.2.1).

These are the cuts chosen for the selection of the tracks:

- $dr < 0.5$ cm
- $|dz| < 2$ cm
- $nSVDHits > 6$

The cuts on dr and dz are taken from standard cuts already used in a large number of analyses, and are considered good thresholds to select the signal tracks.

From now on these cuts will be referred to as the *track selection cuts* or *ts cuts*

4.2.3 Efficiency on signal

The efficiency for the tracks selection cuts on the signal MC is estimated as:

$$Eff(ts) = \frac{N_{rec}(after\ cuts)}{N_{rec}} \quad (4.2)$$

where N_{rec} is the number of reconstructed events of the signal MC.

The global efficiency is measured integrating over the four energies:

$$Eff(ts) = 0.777 \pm 0.004 \quad (4.3)$$

Chapter 5

Validation on control sample

In order to validate the efficiency estimated on the MC simulation, it is important to perform a comparison of MC with experimental data on known and well studied physics channels, with characteristics similar to the channel under analysis in this work. Two channels have been chosen for this analysis, namely $D^{*+} \rightarrow D_0 \pi^+ \rightarrow \pi^+ K^- \pi^+$ and $D^{*+} \rightarrow D_0 \pi^+ \rightarrow \pi^+ K^- \pi^+ \pi_0$, with $BR(D_0 \rightarrow K^- \pi^+) = 3.89\%$ and $BR(D_0 \rightarrow K^- \pi^+ \pi_0) = 3.89\%$.

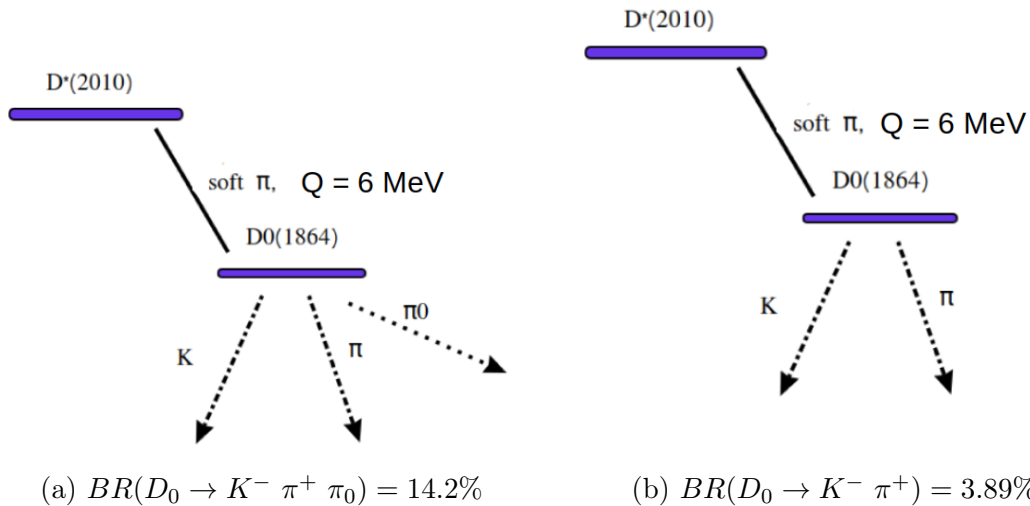


Figure 5.1: Scheme of the decays used for validation of the tracks selection.

The cuts presented in section 4.2.2 will be applied to the pion from the transition to the D_0 and the efficiency computed in the MC will be compared to the efficiency obtained from the data. The ratio of efficiencies will be used as a correction factor to account for discrepancy between MC and data.

These channels are useful since they allow to validate the track selection efficiency of pions track in a clean environment. The validation will be performed studying the efficiency as a function of the transverse momentum of the tracks (p_t). The p_t distribution for the $D^{*+} \rightarrow \pi D_0$ and $e^+ e^- \rightarrow \pi \pi h_b(1P)$ pions is shown in Fig. 5.2.

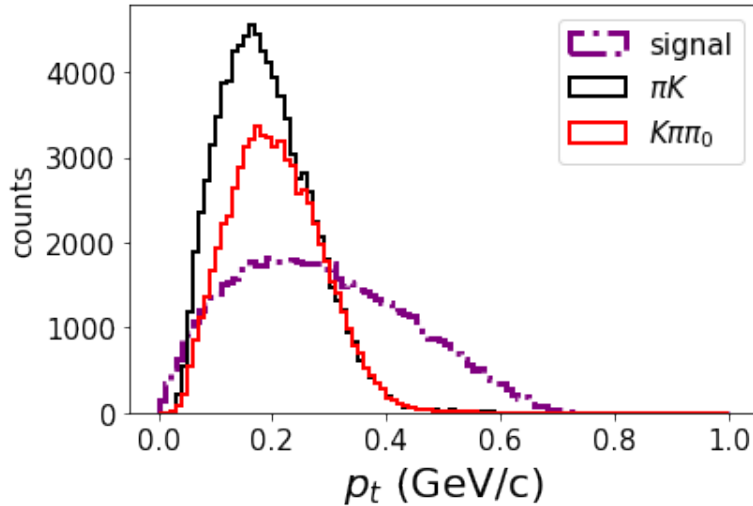


Figure 5.2: Distribution of the p_t from $e^+e^- \rightarrow \pi\pi h_b(1P)$ (purple) and $D^* \rightarrow \pi^+ D^0$ (black and red) pions.

Since $D^{*+} \rightarrow D_0$ transition has a limited phase space, it can mimic the spectrum in p_t of the tracks from the signal, particularly in the lowest region of p_t , where the efficiency is lower and the correction could be more significant. Moreover, since pions of an eventual Z_b transition are very soft, with this channel we can monitor the selection also in their region of p_t .

5.1 Reconstruction of the D^{*+}

Data events are reconstructed from the sample at the four energies of the scan, while generated events are reconstructed from the generic MC.

An inclusive reconstruction of the D^{*+} is performed with both the decay chains shown in Fig. 5.1. Cuts applied for the reconstruction are presented below.

- Cuts for the K^- and π^+ from the D_0 :
 - $thetaInCDCAcceptance == 1$ and $nCDCHits > 20$: requesting the track to be in the CDC acceptance ($17^\circ < \theta < 150^\circ$) and to have number of CDC hits greater than 20 to select well reconstructed tracks;
 - $dr < 0.5$ and $abs(dz) < 2$: select tracks coming from IP.
- Cuts for the π_0 :
 - $0.121 < InvM < 0.142$: constraint on the invariant mass of the $\gamma\gamma$ pairs;
 - $-1.0 < daughterDiffOf(0,1,phi) < 1.0$ and $daughterAngle(0,1) < 0.9$: constraints on the two photons of the π_0 decay, namely their difference of ϕ must be between (-1,1) rad, and the angle between their momentum must be lower than 0.9 rad.
- Cut for the $D^{*+} \rightarrow \pi^+ D_0$ pion:

- $p < 1$ GeV/c: since the majority of signal pions have p lower than 1 GeV/c.
- Cuts for the reconstructed D_0 :
 - $M(K^- \pi^+)$ must be 100 MeV from D_0 mass PDG value (1.864 GeV/ c^2);
 - $M(K^- \pi^+ \pi_0)$ must be 100 MeV from D_0 mass PDG value (1.864 GeV/ c^2).

A kinematic fit on the mass of the π_0 is also performed for the reconstruction of the π_0 .

5.1.1 Analysis of $D_0 \rightarrow K\pi$ channel

The distribution of $M(K\pi\pi)$ and $M(K\pi)$ for the $D_0 \rightarrow K\pi$ channel for both data and MC is shown in Fig. 5.3. MC events are scaled down by a factor of four to account for the higher luminosity of the MC sample.

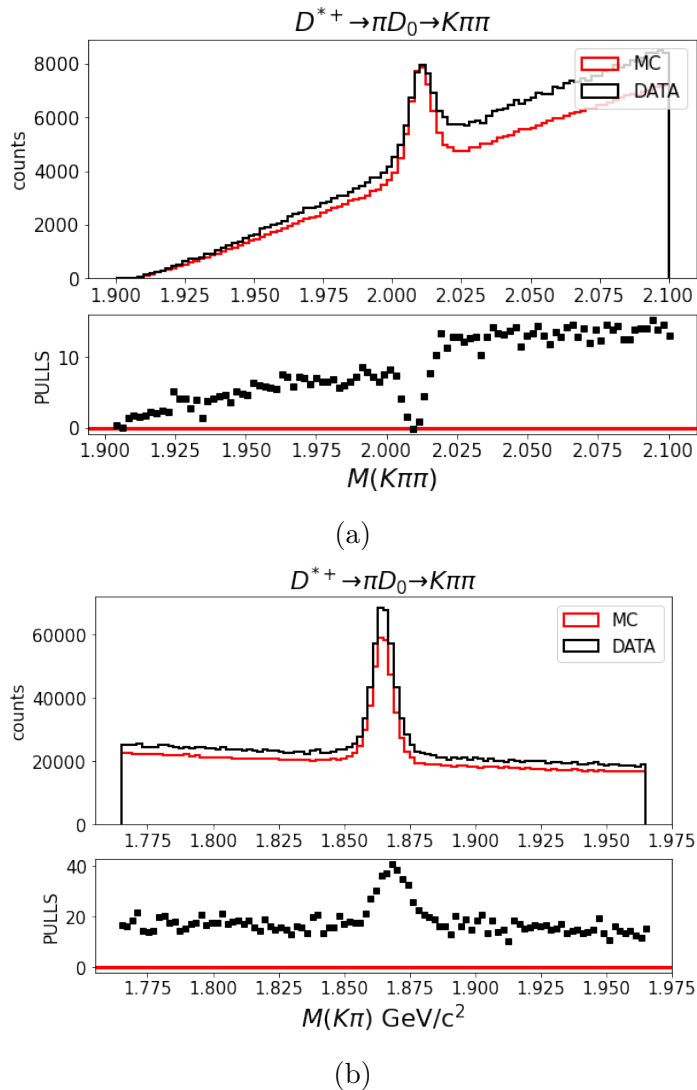


Figure 5.3: Distribution of $M(K\pi\pi)$ and $M(K\pi)$ for data and MC. MC events are scaled down by a factor of four.

The discrepancy between data and MC is ascribed to the fact that while most of the processes in the generic MC are indeed produced with four times the luminosity of the data, as it is reported in Table 3.2, some of the background process are produced with lower luminosity. Since the D^{*+} in the MC are not reconstructed separately for each of the process in 3.2, but from the whole MC sample instead, scaling all the events by a factor of four produces an underestimation of the MC events. The discrepancy is strongly reduced when inspecting difference of mass $\Delta M = (M(K\pi\pi) - M(K\pi))$, as shown in Fig 5.4. The variable represents the energy available for the transition and the peak at $0.136 \text{ MeV}/c^2$ in Fig. 5.4 corresponds to the D^{*+} correctly reconstructed.

This is due to the lower background level in the signal region for ΔM , therefore the discrepancy is smaller. The background reduction is due to the fact that requesting the ΔM to be less than $0.155 \text{ GeV}/c^2$, as reported in Fig 5.4, already removes most of the non resonant background.

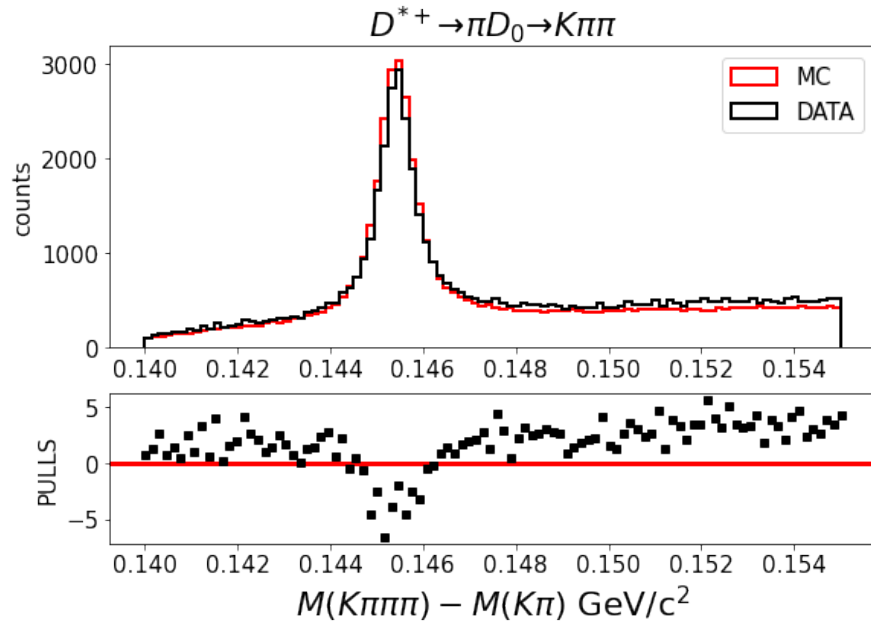
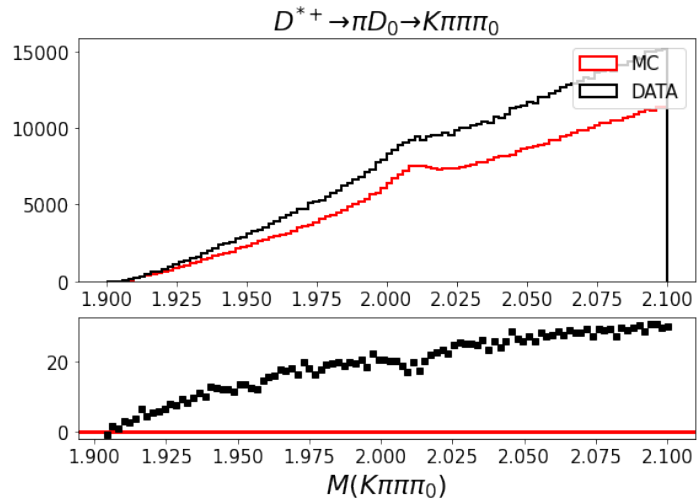


Figure 5.4: Distribution of $M(K\pi\pi) - M(K\pi)$ for $D_0 \rightarrow K\pi$ channel for data and MC (simulated events are scaled down by a factor of four).

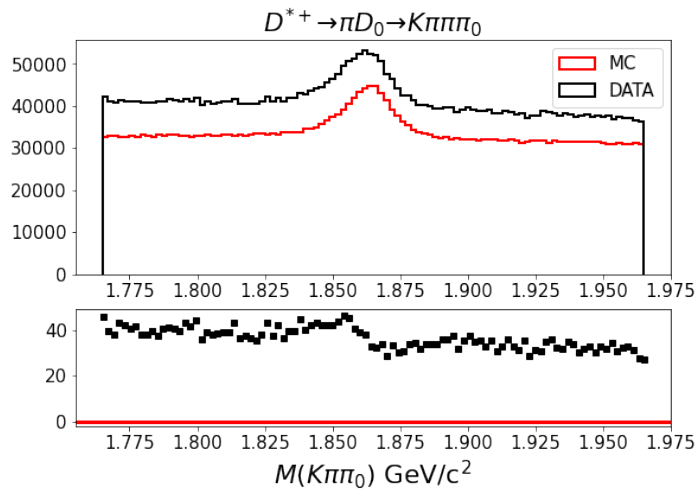
However, the disagreement between the number of events is not relevant to the purpose of this analysis, since the goal of this study is to validate the efficiency of the cuts and not the absolute yield of the D^{*+} .

5.1.2 Analysis the $D_0 \rightarrow K\pi\pi_0$ channel

Distribution of $M(K\pi\pi)$ and $M(K\pi)$ for the $D_0 \rightarrow K\pi$ for both data and MC (simulated events are scaled down by a factor of four) is shown in Fig 5.5.



(a)



(b)

Figure 5.5: Distribution of $M(K\pi\pi)$ and $M(K\pi\pi\pi_0)$ for data and MC (scaled down by a factor of four).

The resolution is considerably worse when compared to the $D_0 \rightarrow K\pi\pi_0$. This is due to the reconstruction of the additional π_0 from a couple of photons in the calorimeter, which lowers the $M(K\pi\pi\pi_0)$ resolution. As for the $D_0 \rightarrow K\pi\pi_0$ channel, the agreement between data and MC is biased for not taking into account the different luminosity for some of the processes.

Distribution of ΔM is shown in Fig. 5.6.

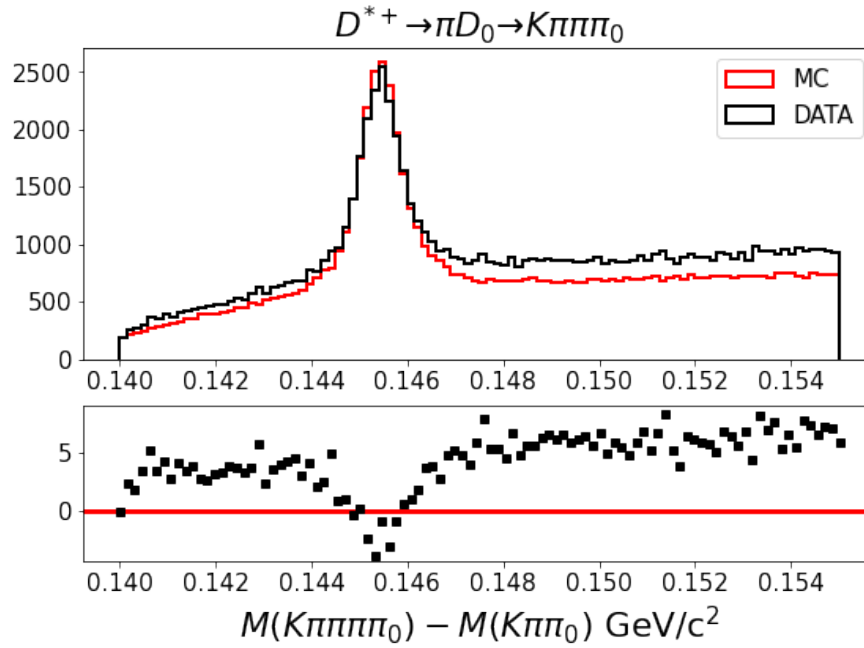


Figure 5.6: Distribution of $M(K\pi\pi) - M(K\pi)$ for $D_0 \rightarrow K\pi\pi_0$ channel.

The agreement between data and MC in this region is better, as for the $D_0 \rightarrow K\pi$ channel. The resolution is similar to the $D_0 \rightarrow K\pi$ channel, since the effect of the π_0 reconstruction is cancelled when subtracting the D^{*+} and D_0 masses.

5.2 Validating Efficiency

To study the efficiency of the track selection in different regions of p_t , events were separated in five bins of p_t of the $D^{*+} \rightarrow D_0$ pion. The selected regions are shown in Fig. 5.7.

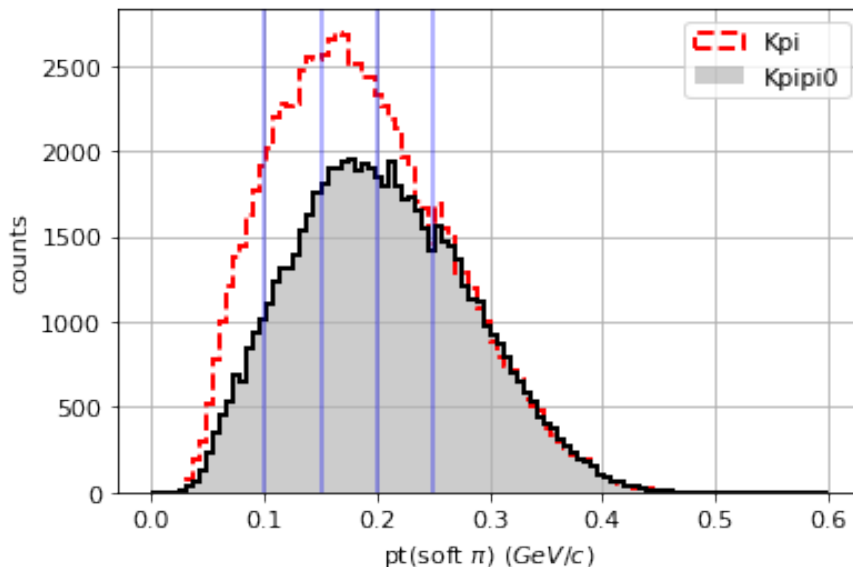


Figure 5.7: Distribution of p_t of the π from $D^{*+} \rightarrow D_0$ in the MC sample. Purple lines represent the bins used in this study.

The bins are 50 MeV/c wide, except for the first, which is 100 MeV and the last, which groups all events with p_t larger than 250 MeV/c. This binning was chosen in order to get a good monitoring in p_t while maintaining a sufficient statistics in each bin.

5.2.1 Measuring efficiency on data

Track selection cuts are applied on the $D^{*+} \rightarrow \pi D_0$ pion and candidates are divided into two samples, the ones passing and the ones not passing the cuts. To obtain both the yield and the efficiency values, ΔM is fitted simultaneously on both samples: this variable was chosen since it shows a better agreement with data and MC, and presents similar resolution in both the $(K\pi)$ and $(K\pi\pi_0)$ channels.

The fit region is defined as $0.14 \leq \Delta M \leq 0.155 \text{ GeV}/c^2$. The signal shape for the two samples (candidates passing and not passing the cuts) is parameterized as the sums of three Gaussians, with their parameters fixed after two fits on MC events. This choice was made since the resolution in the detector is not gaussian, and the tails of the distribution are better parameterized in this way. A Crystal Ball function has been tried for the fit, but the sum of three Gaussians performed better in terms of fit quality, therefore it was preferred.

An example of the fits on MC for the $0.1 < p_t < 0.15 \text{ GeV}/c$ bin on the $D_0 \rightarrow K\pi$ is shown in Fig. B.7.

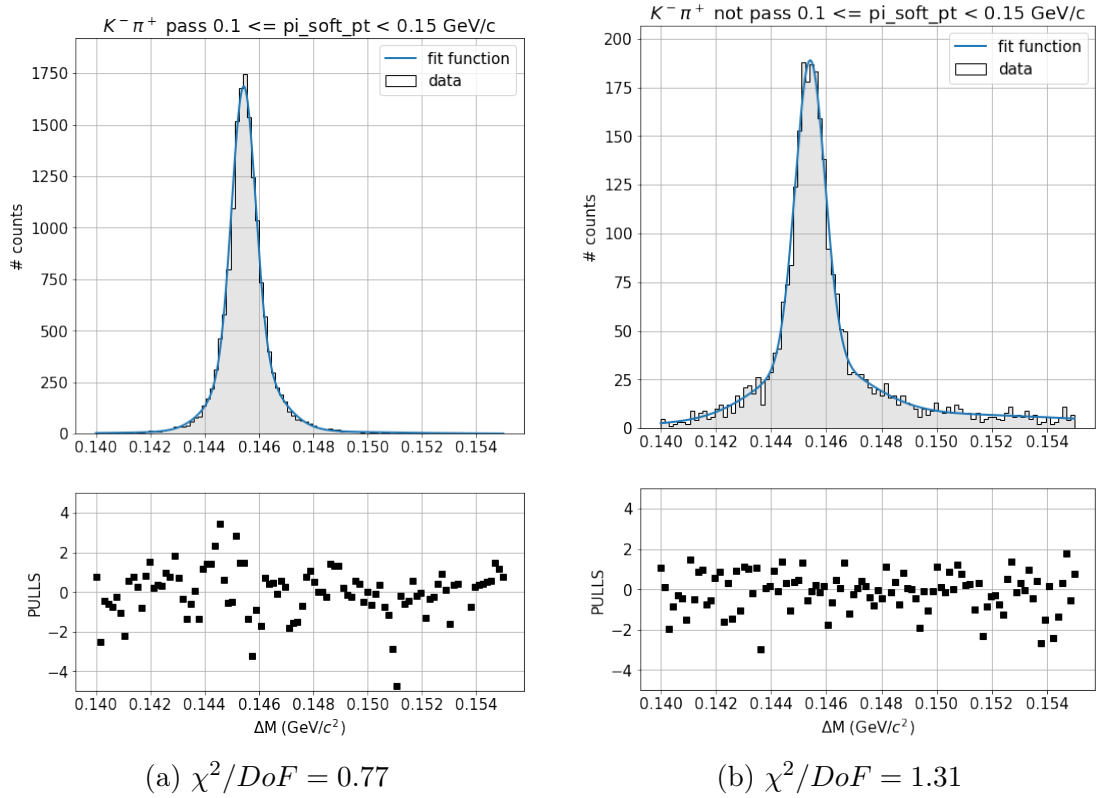


Figure 5.8: Distribution of ΔM for MC $D^{*+} \rightarrow K^+\pi^+\pi^+$ signal events that pass (a) and do not pass (b) the track selection cuts in the $0.1 < p_t < 0.15$ GeV/c bin. Grey histogram represents the MC points, blue solid line is the signal fit function.

Pass the cut	
χ^2/Dof	1.46
μ_1	$(1.45437 \pm 0.00001) \cdot 10^{-1}$
μ_2	$(1.4555 \pm 0.0002) \cdot 10^{-1}$
μ_3	$(1.462 \pm 0.0002) \cdot 10^{-1}$
σ_1	$(4.3 \pm 0.01) \cdot 10^{-4}$
σ_2	$(10.8 \pm 0.4) \cdot 10^{-4}$
σ_3	$(3.8 \pm 0.3) \cdot 10^{-4}$
D_{yield}^*	$(16.4 \pm 0.1) \cdot 10^3$
$yield_1/yield_2$	(0.63 ± 0.02)
$yield_{1+2}/yield_3$	(0.953 ± 0.005)
Do not pass the cut	
χ^2/Dof	0.90
μ_1	$(1.454 \pm 0.001) \cdot 10^{-1}$
μ_2	$(1.50 \pm 0.02) \cdot 10^{-1}$
μ_3	$(1.4542 \pm 0.0002) \cdot 10^{-1}$
σ_1	$(1.9 \pm 0.2) \cdot 10^{-4}$
σ_2	$(6.2 \pm 1.1) \cdot 10^{-3}$
σ_3	$(5.4 \pm 0.3) \cdot 10^{-4}$
D_{yield}^*	$(28.4 \pm 0.5) \cdot 10^2$
$yield_1/yield_2$	(0.61 ± 0.07)
$yield_{1+2}/yield_3$	(0.51 ± 0.03)

Table 5.1: Fit results on both MC samples.

Once the parameters of the probability density function (pdf) for the signal are fixed, a simultaneous fit is performed on data, for events that pass the cuts and events that do not. Total yield (pass + not pass) and efficiency are left as common parameters; since the two samples are completely separated, the uncertainties obtained from the fit are not correlated. Signal pdfs obtained from MC are convoluted with a gaussian, to account for different resolution between data and MC. Background in each data sample is parameterized as a 5th order Chebychev polynomial. The first bin on the $K\pi$ channel uses the following function instead:

$$F_{bkg} = Pol(3) * \sqrt{\Delta M - \Delta M_{min}} \quad (5.1)$$

where $Pol(3)$ is a third order polynomial and ΔM_{min} is the kinematic limit of the distribution. This choice was made since it produces a better agreement between model and data in the first bin, but in the other cases the Chebychev polynomial still lead to better fits.

The fits are performed on unbinned data with minimization of Likelihood. An example of the simultaneous fit performed in the $0.1 < p_t < 0.15$ bin for the $D_0 \rightarrow K\pi$ channel is shown in Fig. ??.

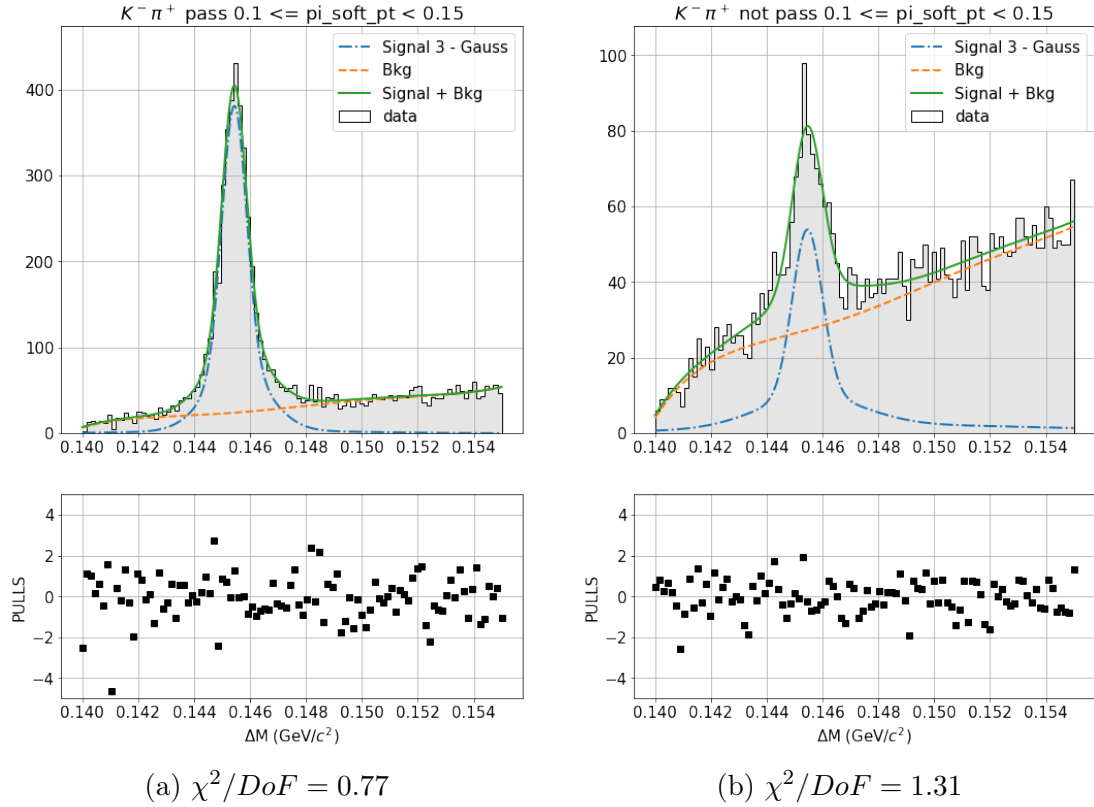


Figure 5.9: Distribution of ΔM for DATA events that pass (a) and do not pass (b) the track selection cuts in the $0.1 < p_t < 0.15$ GeV/c bin. Grey histogram represents the data points, green solid line is the combined fit function, blue dotted line is the signal fit function, orange dotted line is the background fit function.

Sample Parameters	Pass	Not pass
χ^2/DoF	1.31	0.78
μ_{conv}	$(-0.07 \pm 5) \cdot 10^{-5}$	$(3 \pm 5) \cdot 10^{-5}$
σ_{conv}	$(0 \pm 7) \cdot 10^{-5}$	$(0 \pm 7) \cdot 10^{-4}$
a	$(6.8 \pm 0.4) \cdot 10^{-2}$	$(7 \pm 0.4) \cdot 10^{-1}$
b	$(-0.1 \pm 4) \cdot 10^{-2}$	$(-4 \pm 4) \cdot 10^{-2}$
c	$(3 \pm 4) \cdot 10^{-2}$	$(5 \pm 3) \cdot 10^{-2}$
d	$(-2 \pm 3) \cdot 10^{-2}$	$(-5 \pm 3) \cdot 10^{-2}$
e	$(5 \pm 4) \cdot 10^{-2}$	$(2 \pm 3) \cdot 10^{-2}$
Common Parameters		
Signal yield	$(4.5 \pm 0.1) \cdot 10^3$	
eff	(0.82 ± 0.01)	

Table 5.2: Fit results on data samples; sample parameters are different between the two sample, while common parameters are shared.

All the fits are performed with the Zfit [55] package on Python3.

5.2.2 Results

The plots of the efficiency in bins of p_t for data and MC in each channel are shown in Fig. 5.10, efficiency on MC was computed by looking at the MC truth.

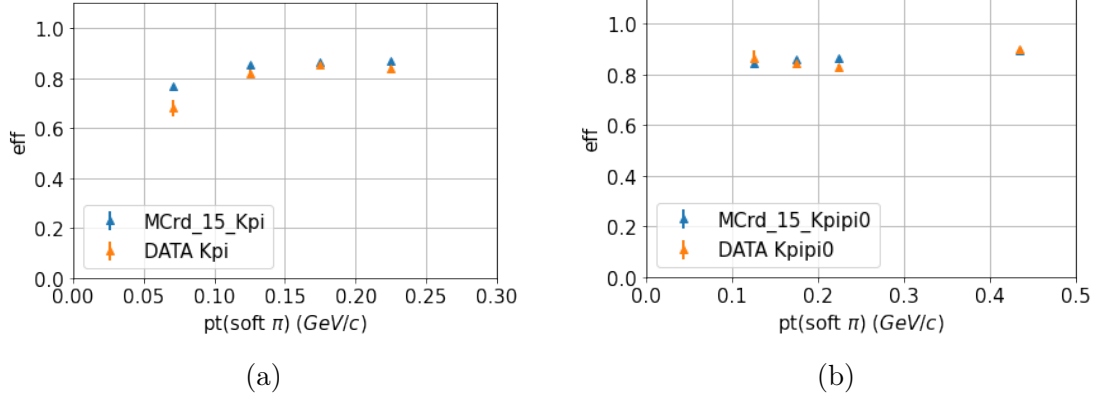


Figure 5.10: Distributions of efficiency in MC and data vs p_t of the soft pion, for both $K^- \pi^+$ (a) and $K^- \pi^+ \pi_0$ (b) channels.

The first bin ($p_t < 0.1$) of the $K\pi\pi_0$ channel and the last bin ($p_t > 0.25$) of $K\pi$ channel are missing, since in the first case the statistics was too low to perform a fit and in the latter case the fit showed low significance.

The ratio between the efficiency on data and MC is introduced as a parameter called $R(p_t)$:

$$R(p_t) = \frac{eff_{data}(p_t)}{eff_{MC}(p_t)} \quad (5.2)$$

The distribution of the values of R for the $K\pi$ and $K\pi\pi_0$ channels is shown in Fig. 5.11, and the obtained values are reported in Table 5.3.

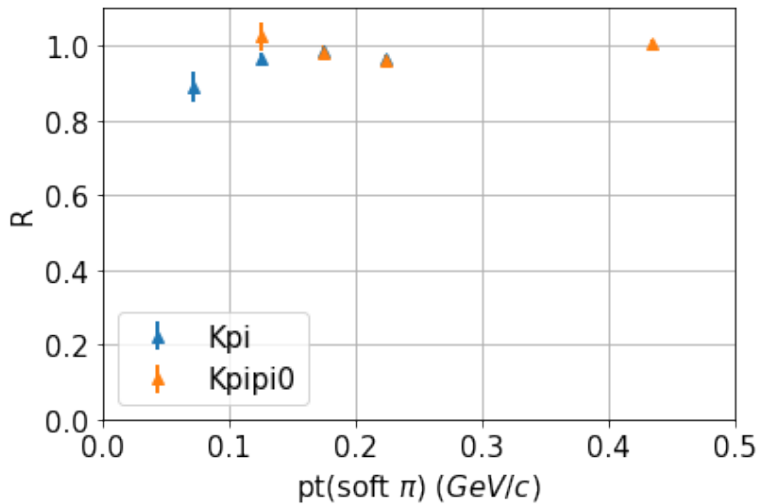


Figure 5.11: Distribution of R as a function of p_t .

Bin	$R(K\pi)$	$R(K\pi\pi_0)$
$p_t < 0.1$	0.89 ± 0.04	
$0.1 \leq p_t < 0.15$	0.96 ± 0.02	1.02 ± 0.04
$0.15 \leq p_t < 0.2$	0.98 ± 0.01	0.98 ± 0.02
$0.2 \leq p_t < 0.25$	0.96 ± 0.01	0.96 ± 0.01
$p_t \geq 0.25$	1.01 ± 0.01	

Table 5.3: Values of $R = \text{eff}_{Data}/\text{eff}_{MC}$ for the different bin of p_t in $D^0 \rightarrow K^-\pi^+$ and $D^0 \rightarrow K^-\pi^+\pi_0$.

The corrections between data and MC are quite small, except for the first bin, where the MC events have larger efficiency compared to data. R is also similar between the two channels and the final value will be computed as the weighted mean in each bin. Having obtained this results, the values of R will be interpolated to get a function $R(p_t)$.

Chapter 6

Efficiency as a function of p_t and $\cos \theta$

A study of the dependence of the efficiency for both the tracks selection and the reconstruction from p_t and $\cos \theta$ is performed. The binning in $\cos \theta$ is introduced to study possible effects due to the geometry of the detector.

Opposite charge tracks are studied separately to account for different efficiency between positive or negative pions. Since the efficiency is measured on the single tracks, this method ignores the correlation between the two pions: efficiency of reconstructing two positively correlated tracks could be larger than the product of efficiencies of the single tracks. The effect of correlation will be checked on section 6.

6.1 Efficiency estimation on generic MC

This study is performed on the generic MC, since it has a much larger statistic and the efficiency measurement on MC has been proven to be reliable using the control channel. A 2D histogram is constructed with p_t and $\cos \theta$ on the axes, and the efficiency on each bin is measured as:

$$Eff(p_t, \cos \theta) = \frac{N_{rec}^{cut}(p_t, \cos \theta)}{N_{MC}(p_t, \cos \theta)} \quad (6.1)$$

where $N_{rec}^{cut}(p_t, \cos \theta)$ is the number of reconstructed events after the cuts and $N_{MC}(p_t, \cos \theta)$ is the number of events generated, in each bin of p_t and $\cos \theta$. The obtained distributions are shown in Fig. 6.1.

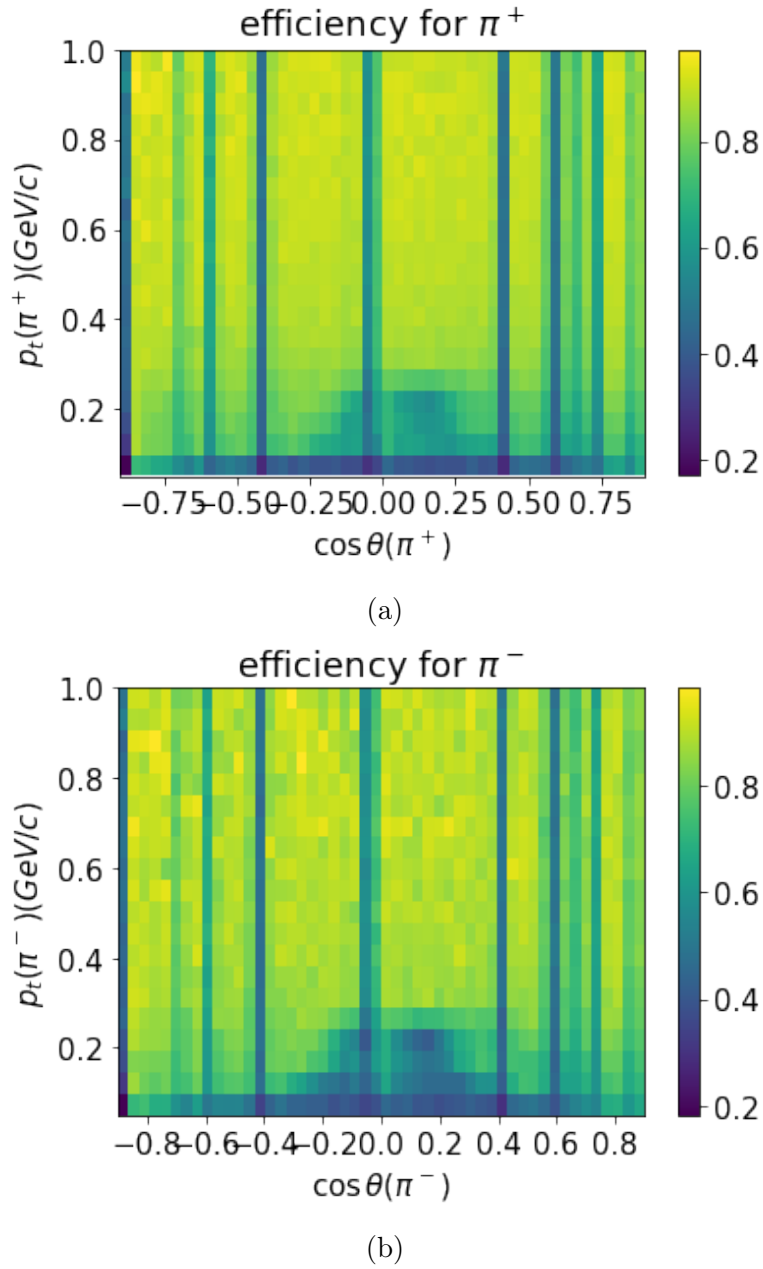


Figure 6.1: Distribution of the efficiency for positive and negative tracks, in bins of p_t and $\cos\theta$.

A drop of efficiency for tracks with low p_t can be found around $\cos\theta = 0$. This drop is ascribed to the fact that soft tracks perpendicular to the beam axis curl and remain trapped in the SVD, thus making them harder to reconstruct since they either do not reach the CDC, or keep curling in the detector, thus leaving several hits in the same region and making them harder to reconstruct.

Several dips of efficiency are found at certain values in $\cos\theta$. This effect is due to blind spots in the SVD at specific values of $\cos\theta$: when selecting tracks with $nSVDHits$ greater than 6, there is a loss of efficiency for signal tracks that cross the four layer of the SVD but due to the blind spots leave signals in just three of them.

The 2D histogram presented in Fig. 6.1 are interpolated in order to get two different functions for positive and negative tracks:

$$eff_p(p_t(\pi^+), \cos \theta^+) \quad eff_n(p_t^{\pi^-}, \cos \theta^{\pi^-}) \quad (6.2)$$

Interpolation of the 2D grids was performed in Python3 with the RegularGridInterpolator method from the scipy library [56], using "nearest" as the interpolation method.

To check the effect of the efficiency correction, each candidate in the generic MC is then weighted with a factor equal to:

$$W_{candidate}(p_t^+, p_t^-, \cos \theta^+, \cos \theta^-) = eff_p(p_t^+, \cos \theta^+)^{-1} \cdot eff_n(p_t^-, \cos \theta^{\pi^-})^{-1} \quad (6.3)$$

and the distribution of $\cos \theta$ and p_t for the weighted events is shown in Fig 6.2.

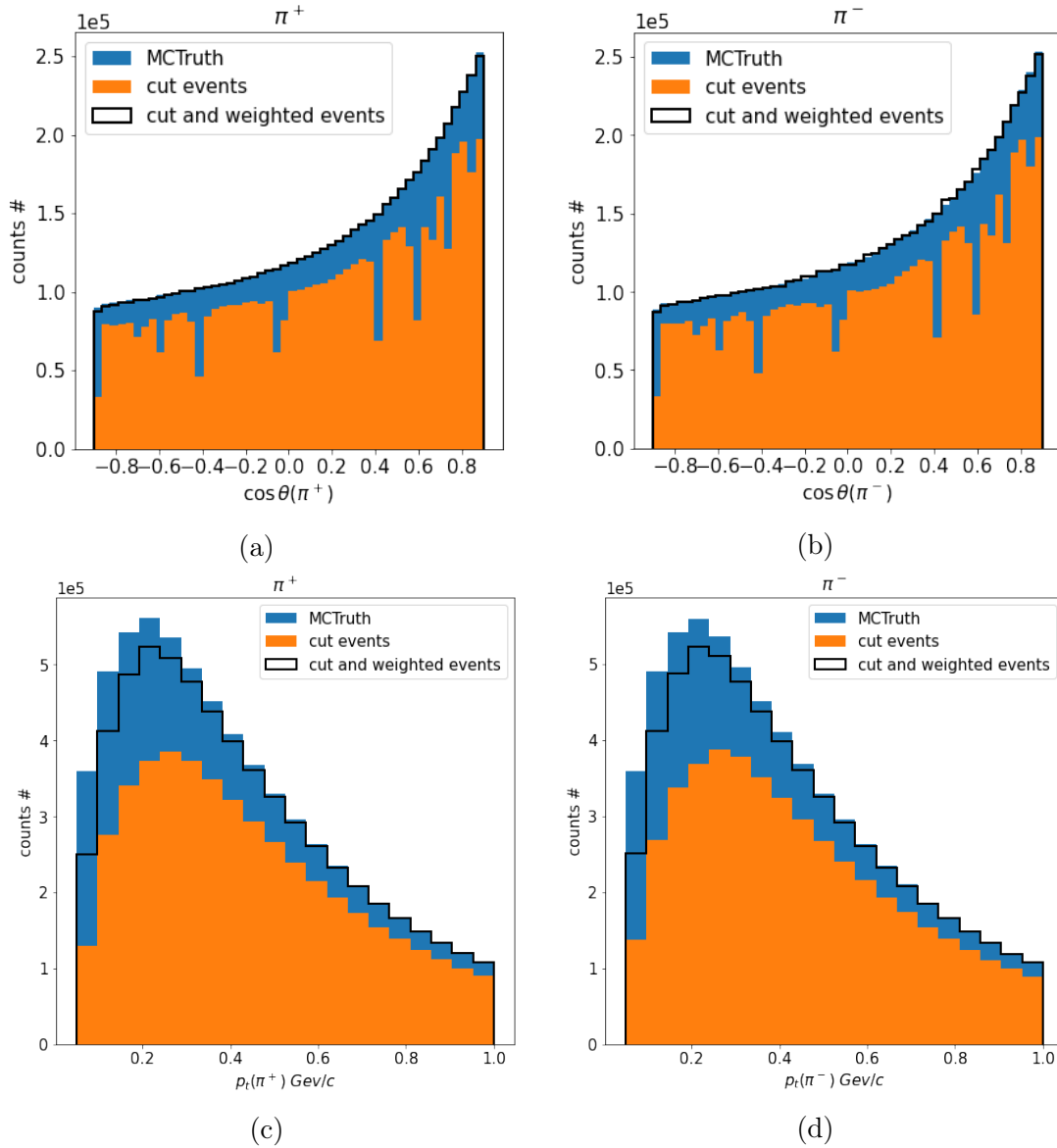


Figure 6.2: Distributions of $\cos \theta$ and p_t for generic MC tracks, weighting each track to account for the efficiency of tracks selection and reconstruction

The dips in $\cos \theta$ have been smoothed out, but still remain some discrepancy at lower p_t . Discrepancies are ascribed to the approximations introduced while interpolating the 2D histogram.

6.2 Weighting the candidates

The generic MC was used to obtain the weights used to correct for the reconstruction and track selection efficiencies.

To account for discrepancy between data and MC, $R(p_t)$ is used to get a new definition of the weight for each track:

$$W_{candidate}^*(p_t^+, p_t^-, \cos \theta^+, \cos \theta^-) = W_{candidate}(p_t^+, p_t^-, \cos \theta^+, \cos \theta^-) \cdot R(p_t^+)^{-1} \cdot R(p_t^-)^{-1} \quad (6.4)$$

where $W_{candidate}$ is computed as in Equation 6.3. The weights obtained with the generic MC are used to correct for both reconstruction and tracks selection. $R(p_t)$ is used to correct only for the efficiency of the latter since it was measured as the ratio of the efficiency for tracks selection cuts in data to MC. The efficiency of the reconstruction is assumed equal for MC and data. $R(p_t)$ is also assumed equal between positive and negative tracks.

To account for systematic uncertainties on R the following strategy will be adopted when fitting on data: multiple fits will be performed, each time randomly varying the values of R obtained in 5.2.2 in a range defined by its errors and making a new interpolation of $R(p_t)$ to compute the weights. The spread of the distribution for the yield will be used as an esteem for the systematic uncertainty related to this correction.

6.2.1 Correlation on the signal

As mentioned before, this strategy neglects correlation between the two pions from the $e^+e^- \rightarrow \pi\pi h_b(1P)$; the reconstruction and selection of two correlated tracks can in fact have an efficiency different from the product of efficiency of the single tracks. The correlation is quantified by measuring the ratio of the two efficiencies as:

$$\frac{eff(p_t^+) \cdot eff(p_t^-)}{eff_{dipion}(p_t^+, p_t^-)} \quad (6.5)$$

where $eff(p_t^+)$ and $eff(p_t^-)$ are the efficiencies measured for the signal pions in the MC, for the positive and negative tracks in bins of p_t , while $eff_{dipion}(p_t^+, p_t^-)$ is the efficiency for the reconstruction of both the two tracks from the decay, in bins of p_t^+ and p_t^- . A 2D histogram of the ratio between the two efficiencies in bins of the track p_t is shown in Fig. 6.3.

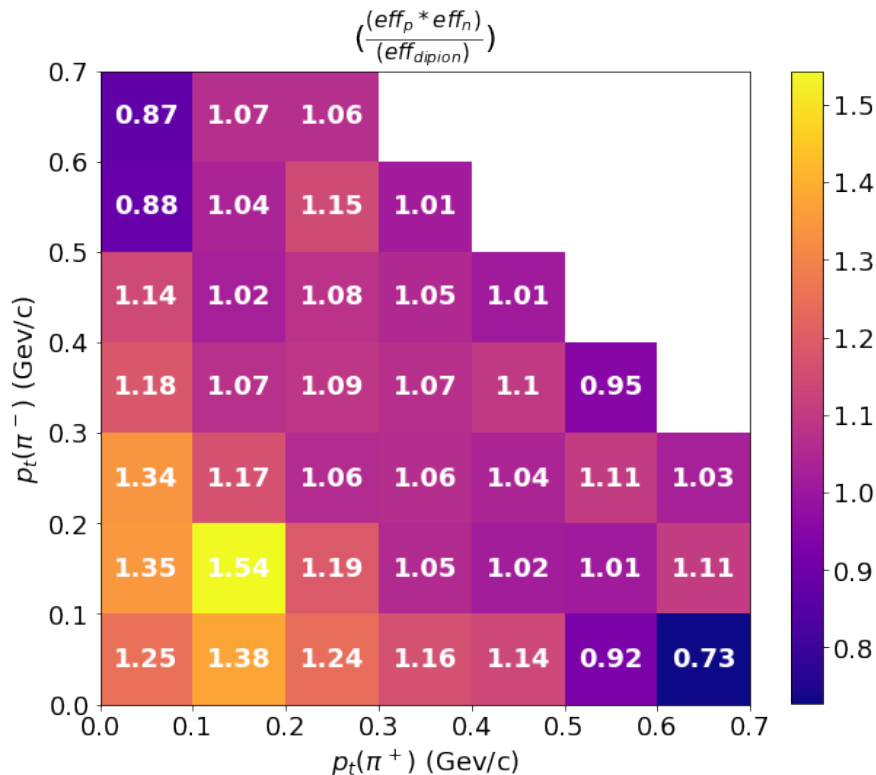


Figure 6.3: Ratio of efficiencies in bins of p_t of the two pion tracks.

The discrepancy is small except for the lower values of p_t , where the product of efficiencies is higher than the efficiency of the pion pair. Since pions from this region come mainly from ISR events, this effect is ascribed to a different kinematic of the tracks. To compute the impact of this correction on the weighting procedure, the MC yield is compared with the yield of the reconstructed events after tracks selection and weighting. The results are shown in Table 6.1.

Energy (MeV)	MC Truth yield	Weighted yield	$\frac{\Delta_{Yield}}{Yield_{MCT}}$
10657	6257	6107	0.03
10706	926	897	0.03
10746	19007	18271	0.04
10805	11326	11123	0.02

Table 6.1: Yields for the generated $e^+e^- \rightarrow \pi\pi h_b(1P)$ signal events (first column), and the weighted values after the reconstruction and the tracks selection.

The weighting produce a small underestimation of the yield. Since this effect is in the order of few points percentage, it will be treated as a systematic effect and yield from the fit will be corrected accordingly to account for this.

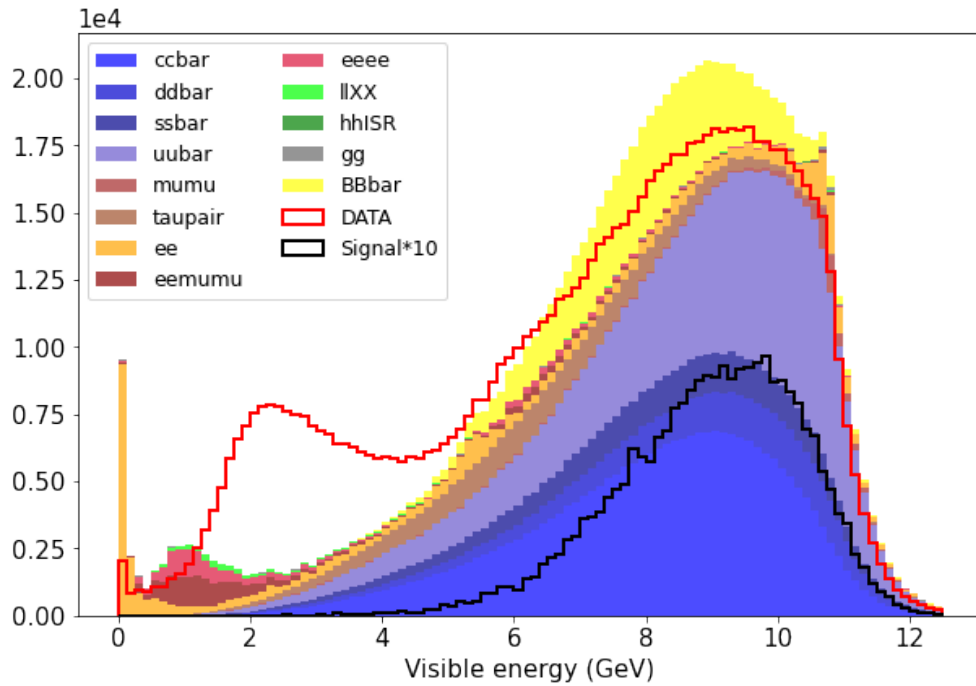
Chapter 7

Events Kinematics and Continuum Suppression

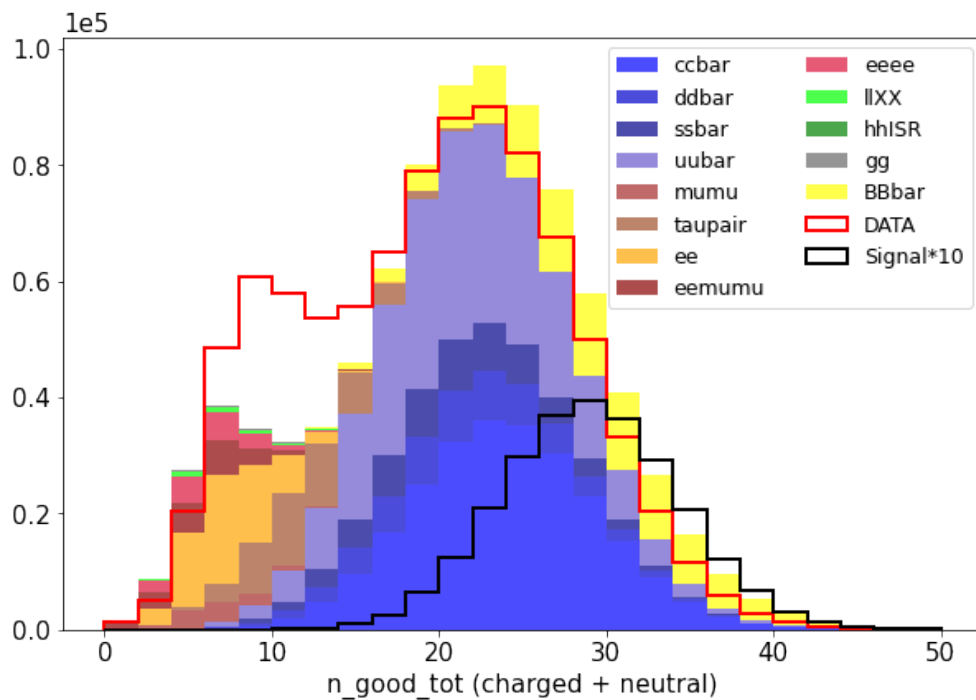
As mentioned in Section 3, Continuum Suppression involves the selection and the removal of events of the type $e^+e^- \rightarrow q\bar{q}$ ($q \in u, d, s, c$). Since they produce lighter hadrons which travel in the detector as jets of particles, their topology can be distinguished from the central events, like $e^+e^- \rightarrow B\bar{B}$. However, before approaching the Continuum Suppression, a brief study of the Events Kinematics will be performed. The distributions of the visible energy of the in the c.m. will be presented for the different contributions to the generic MC, for the signal and for the data. The number of good tracks, both charged and neutral, will also be inspected. While these two variables are not directly involved in the topology of the event (and therefore in the Continuum Suppression), they can still give useful information about the various processes involved in the e^+e^- interactions.

7.1 Energy and Number of tracks

The distributions of visible energy of the event in the center of mass E_{vis} (computed as the $\sqrt{P_*^\mu P_{\mu*}}$, where P_{sum} is the total four-momentum vector in the center of mass of the particle in the event), and of the number of good tracks (n_good_tot) for data and MC (signal and generic) are shown in Fig. 7.1. MC events are weighted to account for the different luminosity and signal is enlarged by a factor of ten.



(a)



(b)

Figure 7.1: Distributions of visible energy in the center of mass and number of good tracks, for data and for different MC samples.

Compared to MC, in data there is a larger number of events characterized by E_{vis} lower than 4 GeV and number of good tracks around ten. This is due to $e^+e^- \rightarrow (\text{many hadrons})$ events, which are not properly simulated in the background. The signal events are located quite far from this region, therefore

events with $(E_{vis}) > 4$ AND $(n_good_tot > 12)$ are selected.

The 2D distribution of n_good_tot vs E_{vis} is shown in Fig. 7.2.

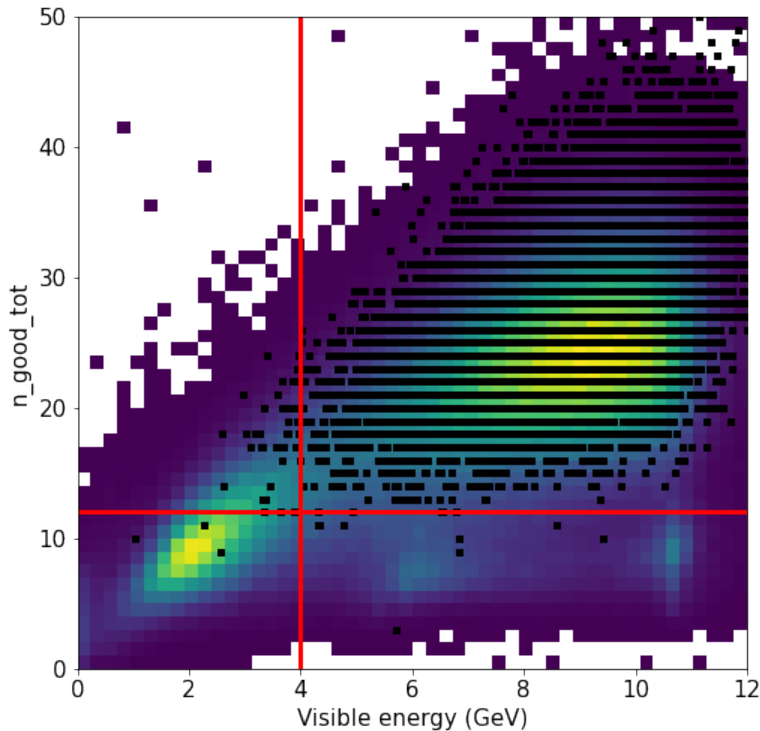


Figure 7.2: Distribution of n_good_tot vs E_{vis} , where the continuous distribution refers to the data events and the black points are the MC signal events.

With this selection, highlighted by the red lines, the $e^+e^- \rightarrow (\text{many hadrons})$ are greatly reduced, without noticeably affecting the signal.

Another source of discrepancy between data and MC comes from the simulation of the Level 1 Trigger (that should suppress Bhabha events) and from simulation of $e^+e^- \rightarrow B\bar{B}$ events, since there are no precise theoretical predictions for the cross section values at these energies.

7.2 Continuum Suppression

Since the topology of the event involves a large amount of variables related to the event shape in the detector, the optimization of a cut for each of them would not be the optimal strategy; therefore, a multi-variate strategy is chosen, namely the selection will be performed using the multi variate classifier FastBDT.

FastBDT performs multi variate classification through stochastic gradient boosted decision trees (SGBDT) [57]; a brief explanation of SGBDTs is reported in the section 7.3.

7.3 Multivariate analysis with SGBDT

A decision tree (DT) performs a classification between signal and background on the data in input via multiple consecutive binary cuts on different variables; the

cuts are applied at the nodes of the tree and the maximum number of consecutive cuts is called the depth of the tree D , once the final node is reached.

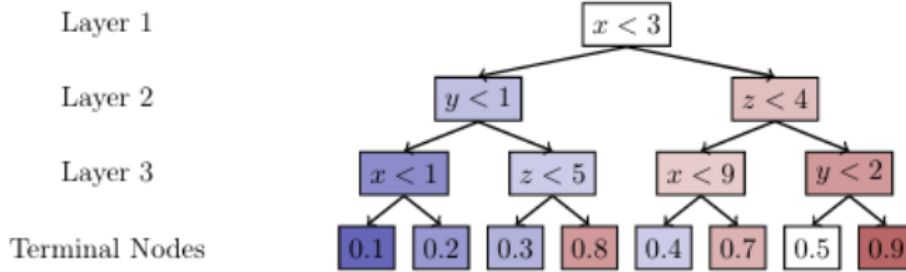


Figure 7.3: Scheme of the operation of a DT [57]: a data event, with no signal/background label, will travel the tree from top to bottom, reaching the final node. The probability of the event to be signal is given from the signal to background ratio in the node.

The first phase of the classification is called the fitting phase, or training phase. In this phase the cuts are determined on a test sample, called training sample, with know signal/background label. For each variable and for each node a cumulative probability histogram (CPH) is calculated for signal and background, respectively. The histograms are used to choose a cut that maximize the separation between the signal and background in each node; this continues till the final node. Once this procedure is done, the cuts can be applied to data events, which travel the tree from top to bottom and reach one of the final node. The probability of a data event to be signal is given by the fraction of signal to background in the reached node (as shown in Fig. 7.3). The prediction of a DT is often dominated by the statistical fluctuation in the training sample, therefore the classifier performs badly on new data points and is usually defined as over-fitted.

To avoid over fitting, a Boosted Decision Tree (BDT) is constructed by creating more shallow trees in the training phase. Since the depth of each DT is limited to avoid over fitting, the separation they provide as singular classifiers is rough, hence are called "weak learners". By joining together many weak learners, however, one obtains a classifier with strong separation power and resistant to over fitting. BDT performances are further improved with by reweighting the original sample at each node in order to give more influence to point that are hard to classify, and by using randomly drawn subsamples in each DT to increase the resistance to over fitting. These are called stochastic gradient boosted decision tree (SGBDT).

7.4 Training the BDT and applying the classifier

The used SGBDT (that for sake of brevity will be called just BDT from now on) was already trained for the $Y(4S) \rightarrow \eta h_b(1P)$ analysis.

The list of variables used for the training is reported below (sums are performed over all the particle p_i and p_j of the events):

- *sphericity* defined as $3/2(\lambda_1 + \lambda_2)$, where λ_i are the first two eigenvalues of the sphericity matrix $S^{\alpha\beta}$

$$S^{\alpha\beta} = \frac{\sum_i p_i^\alpha p_i^\beta}{\sum_i |p_i|^2} \quad (7.1)$$

where α and β refer to the cartesian components of the momentum (xyz);

- 1^{st} and 4^{th} *Wolfram moment*, where the k -th order Fox-Wolfram moment is defined as

$$H_k = \sum_{ij} \frac{|\vec{\pi}| |p_{ij}^\vec{\pi}| P_k(\cos \theta_{ij})}{E_{vis}^2} \quad (7.2)$$

- *CLEO cones* A set of variables that measure the total momentum in cones (at steps of 10°) around the thrust axis, having defined the thrust axis \vec{T} as the following:

$$T = \max(\vec{T}) = \max \frac{\sum_i p_i \cdot \vec{T}}{\sum_i p_i} \quad (7.3)$$

- 0^{th} *order harmonic moment* defined as:

$$B_0 = \sum_i \frac{|\vec{\pi}| P_0(\cos \theta_{ai})}{\sqrt{s}} \quad (7.4)$$

where P_0 is the 0^{th} order Legendre polynomial and θ_{ai} is the angle between the thrust axis and the particle momentum

Although the BDT was not trained for this specific process, since the $Y(4S) \rightarrow \eta h_b(1P)$ transition has a similar topology to $e^+e^- \rightarrow \pi\pi h_b(1P)$, the classifier is assumed to perform well also on this analysis. Once the BDT is trained and the classifier is ready, it is applied on the MC samples (signal and generic), to obtain a variable for each event that indicates the probability of it to be a signal. This variable, called BDT_{prob} in this analysis, will be used to discriminate between background and signal. The BDT is also applied to data for comparison. Distribution of the BDT_{prob} is shown in Fig 7.4 for the different samples.

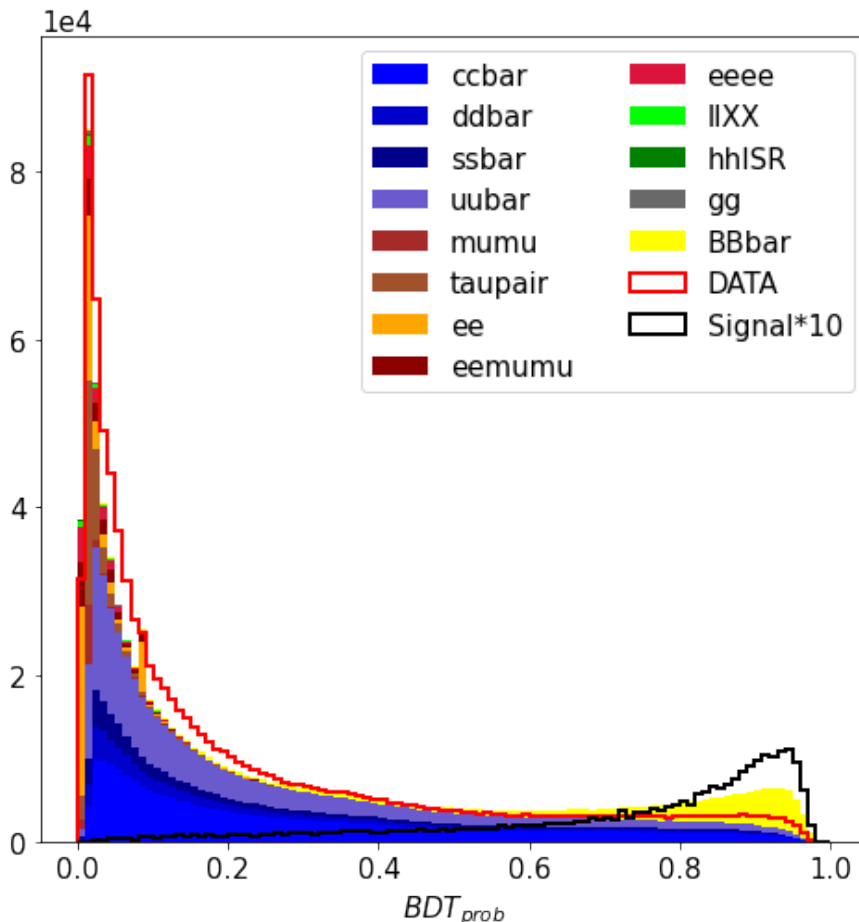


Figure 7.4: Distribution of the BDT_{prob} for the different kinds of MC events (filled), for data (red), and for signal (black).

Signal events have value of BDT_{prob} close to one, while continuum events are peaking close to zero. This means that the classifier manages to separate the signal from the continuum events. Since $B\bar{B}$ are central events, their distribution is similar to the signal as one should expect.

7.5 Optimizing the cut

The cut on the BDT_{prob} is decided via maximization of a figure of merit defined as:

$$FoM = \frac{N_{sig}^*}{\sqrt{N_{sig}^* + N_{bkg}}} \quad (7.5)$$

where N_{bkg} and N_{sig}^* are the number of respectively background and signal events that survive the cut. The signal is weighted to account for a realistic cross section; in this case the events were weighted in order to simulate a cross section of the order of 2pb^{-1} . This is the order of magnitude of the $\Upsilon(5S) \rightarrow \pi\pi\Upsilon(nS)$ ($n = 1, 2, 3$) [58], which proceeds at a similar rate of $Y(5S) \rightarrow \pi\pi h_b(1P)$ [18] transition.

The distribution of the FoM as a function of different cut thresholds is shown in Fig. B.8.

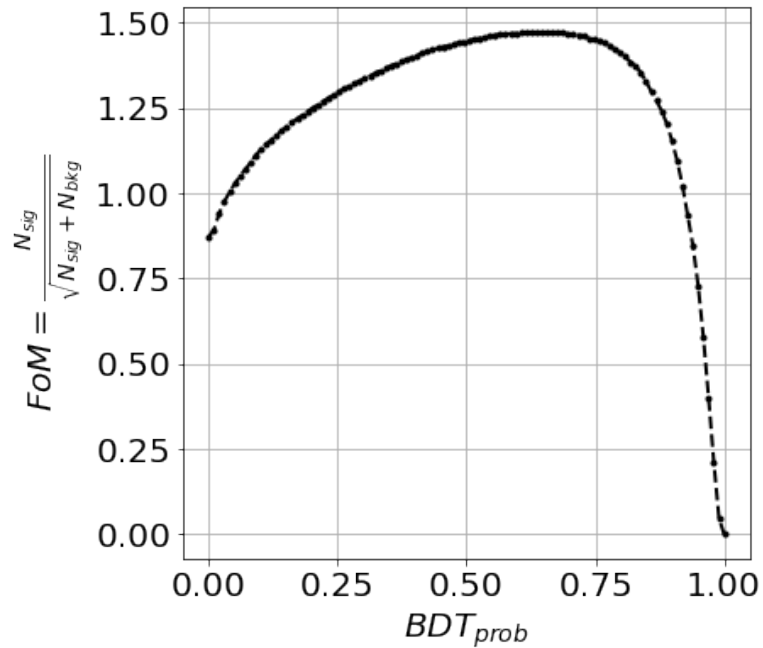


Figure 7.5: Figure of merit for the cut on BDT_{prob} .

The FoM has its maximum for the following cut:

$$BDT_{prob} > 0.62 \quad (7.6)$$

Efficiency for the signal events by applying the following cuts, called *Continuum Suppression cuts* or *CS cuts*:

- $E_{vis} > 4 \text{ GeV}$;
- $n_{good_tot} > 12$
- $BDT_{prob} > 0.62$

is computed as:

$$Eff_{CS} = \frac{N_{rec}(after\ cuts)}{N_{rec}} = 0.728 \pm 0.002 \quad (7.7)$$

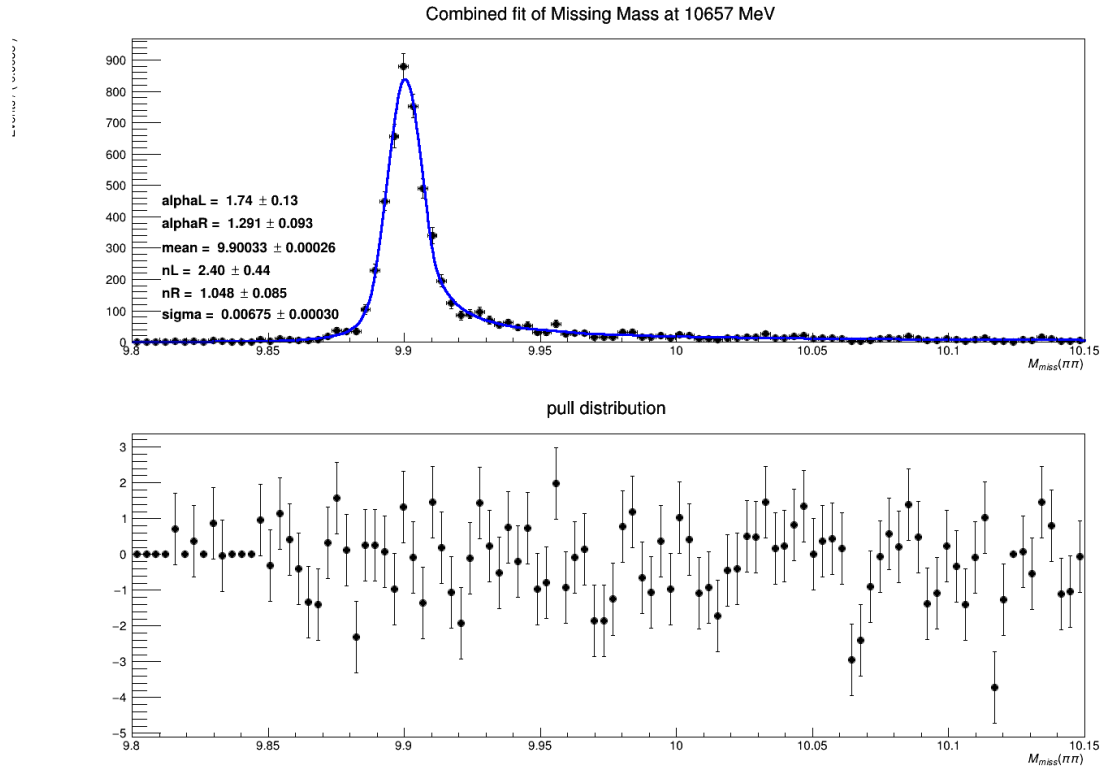
Chapter 8

Fitting strategy

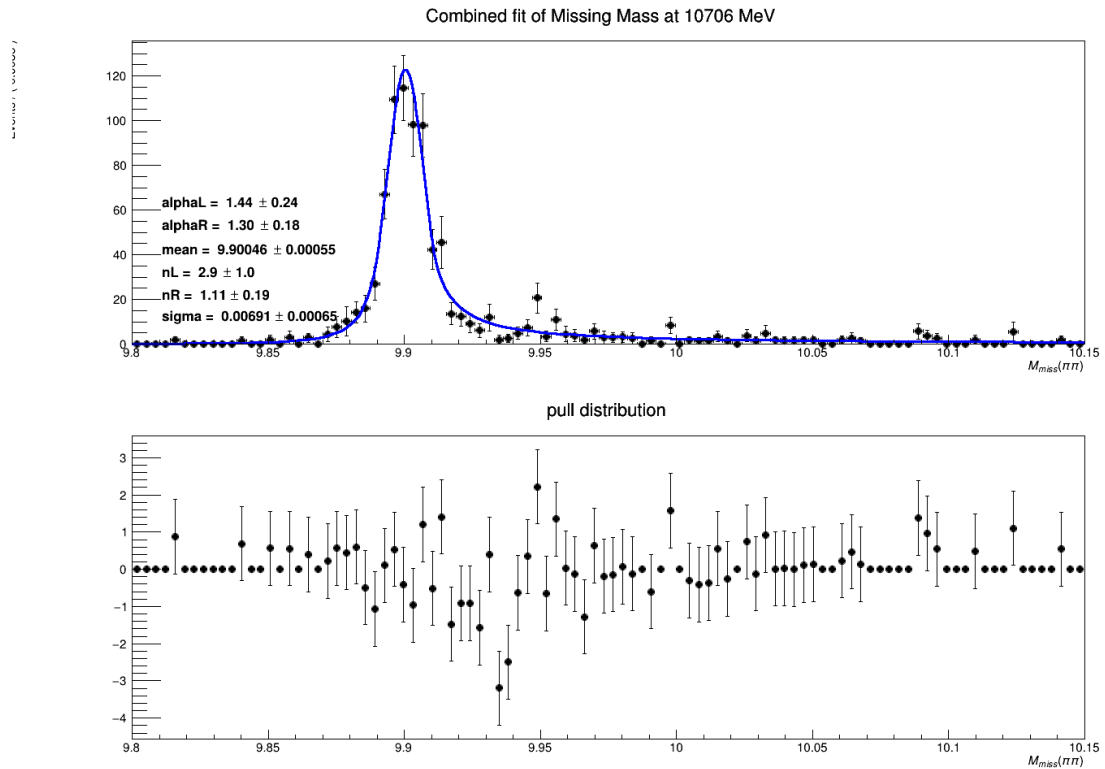
The last part of this analysis involves the identification of the signal region in the $M_{miss}\pi\pi$ spectrum, in which to perform the fit on data and the selection of the pdf for signal and background.

Signal region is defined as $9.8 \leq M_{miss} \leq 10.15$ GeV/c²; this interval was chosen in order to cover a large region of the signal, while maintaining the background distribution sufficiently smooth, to ease the fitting process.

The pdf for the signal is modelled as a Double Sided Crystal Ball (DCB) in order to account for the fact that the tails of the distribution are not Gaussian. A first fit is performed on the reconstructed $e^+e^- \rightarrow \pi\pi h_b(1P)$ signal sample in order to fix the parameters of the distribution for all the four energies; the fit is performed on unbinned data via minimization of the negative log-likelihood. Cuts for tracks selection and continuum suppression are applied, and the candidates are weighted according to the p_t and $\cos\theta$ of the pion pair, as explained in section 6. The results of the fits are shown in Fig. 8.1 and Fig. 8.2.

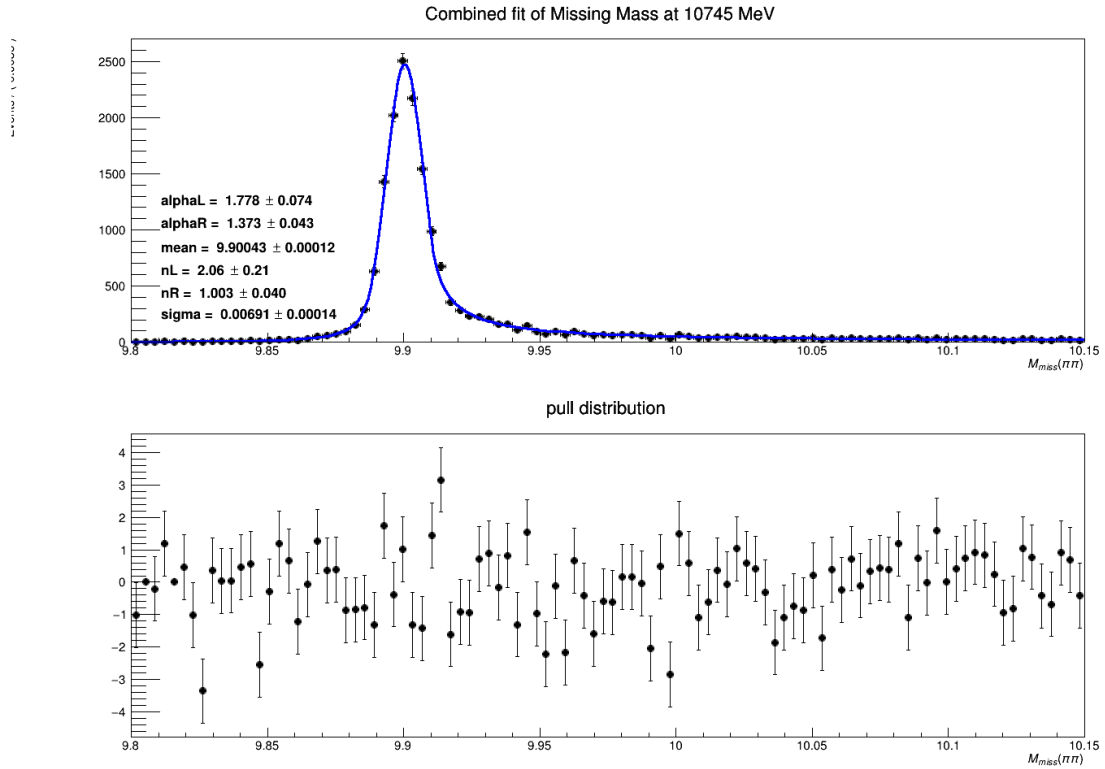


$$(a) \chi^2/DoF = 1.19$$

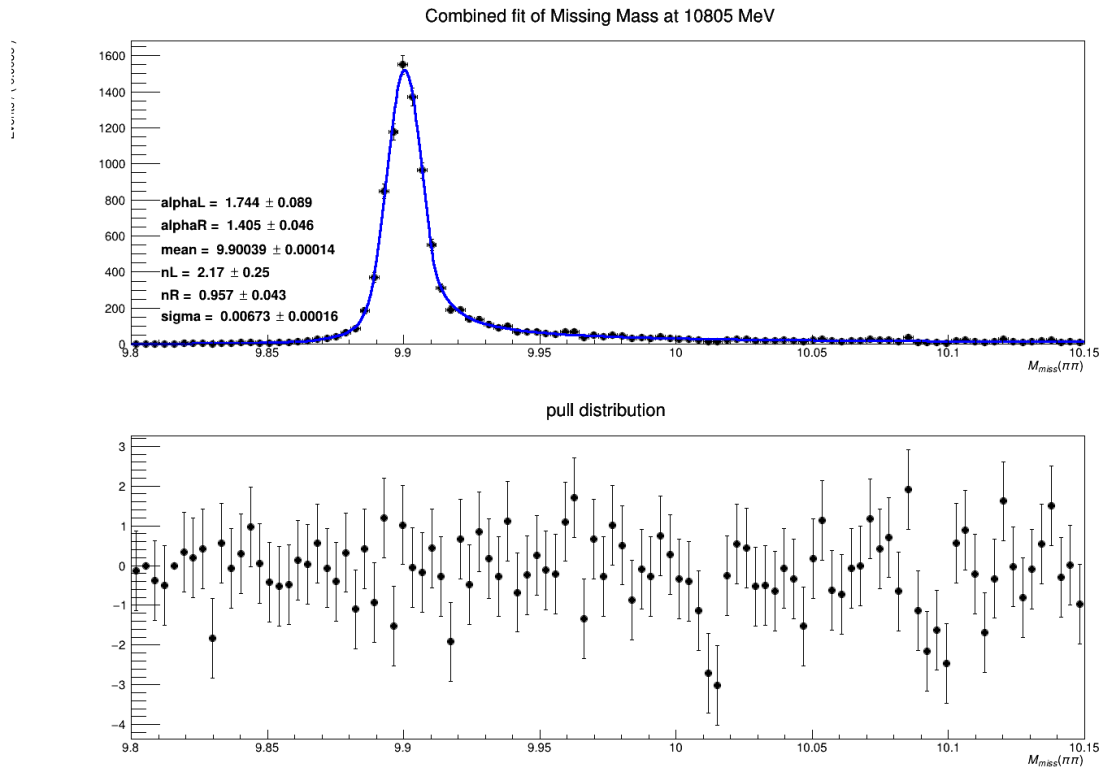


$$(b) \chi^2/DoF = 0.85$$

Figure 8.1: Results of the fits on the $M_{miss}(\pi\pi)$ (GeV/c^2) in the signal region for $e^+e^- \rightarrow \pi\pi h_b(1P)$ events, for the 10657 MeV (a) and 10706 MeV (b) energy points, after applying CS and track selection cuts and weighting the events to account for efficiency of reconstruction and track selection. Points with error bars are MC events, the blue line represents the fit function.



(a) $\chi^2/DoF = 1.21$



(b) $\chi^2/DoF = 0.88$

Figure 8.2: Results of the fits on the $M_{miss}(\pi\pi)$ (GeV/c^2) in the signal region for $e^+e^- \rightarrow \pi\pi h_b(1P)$ events, for the 10745 MeV (a) and 10805 MeV (b) energy points, after applying CS and track selection cuts and weighting the events to account for efficiency of reconstruction and tracks selection. Points with error barr are the MC events, the blue line represents the fit function.

Other four fits are performed at each of the four energy points, combining the signal sample with the generic MC. The pdf for the combined distribution is the sum of a 3rd order Chebyshev polynomial to parameterize the background and the signal pdf obtained before (see Fig. 8.1 and Fig. 8.2), with the DCB parameters fixed except for the σ of the DCB and for the signal yield. This is done in order to check if the fit can resolve the signal peak when the background contribution is added. Continuum suppression and track selection cuts were applied and the candidates were weighted with the usual procedure.

The results of the fits are shown in Fig. 8.3 and Fig. 8.4.

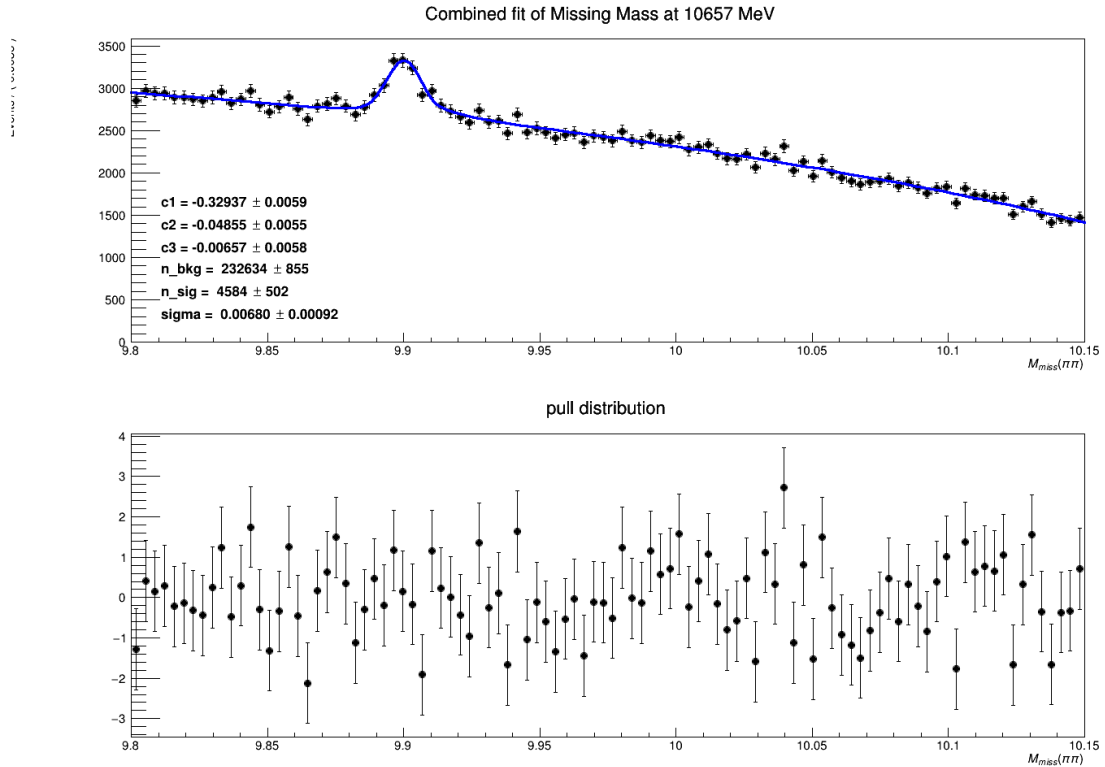
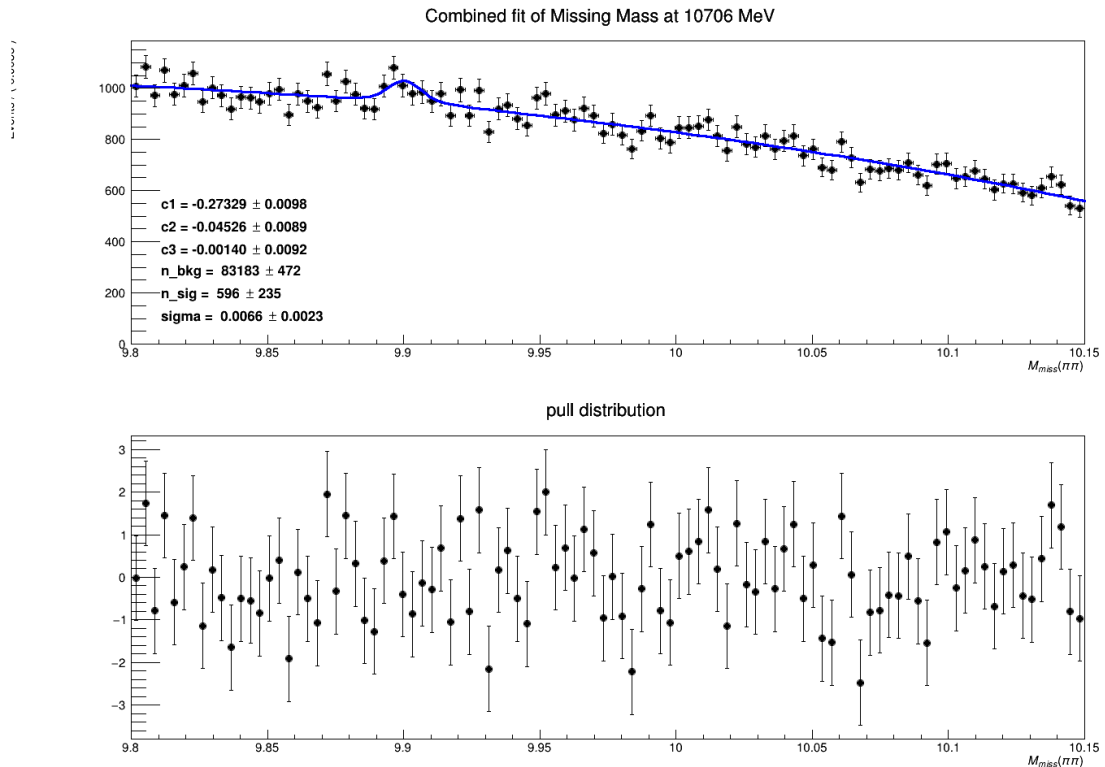
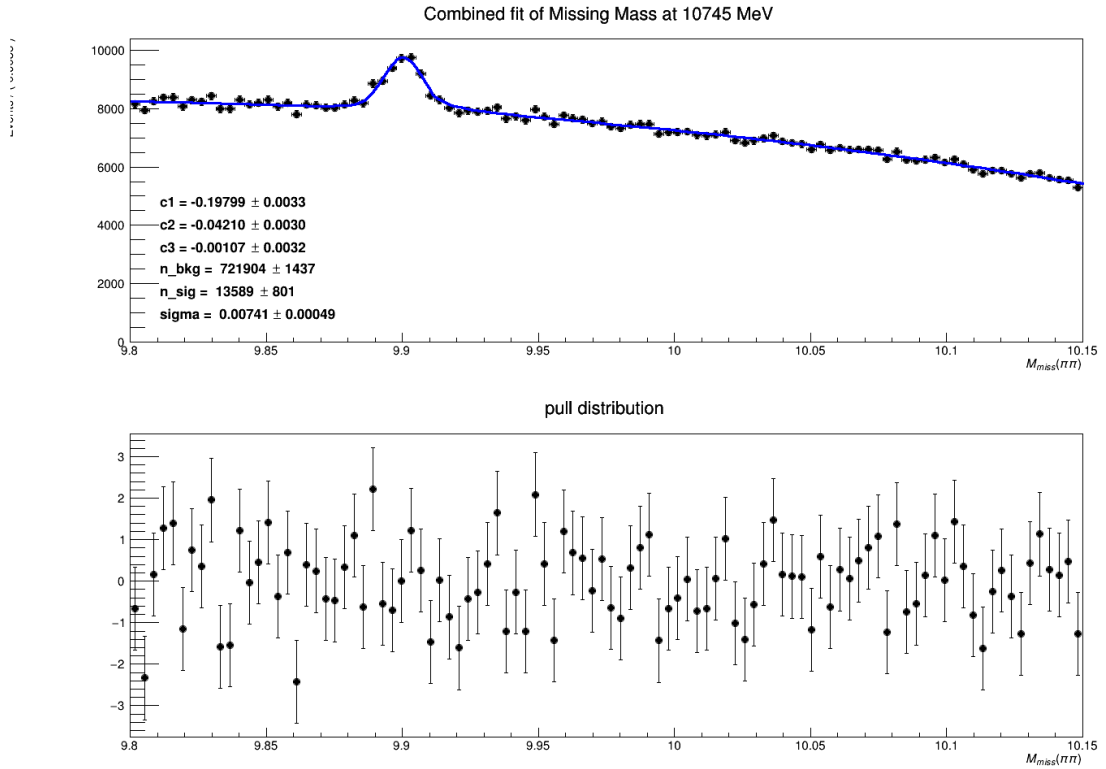
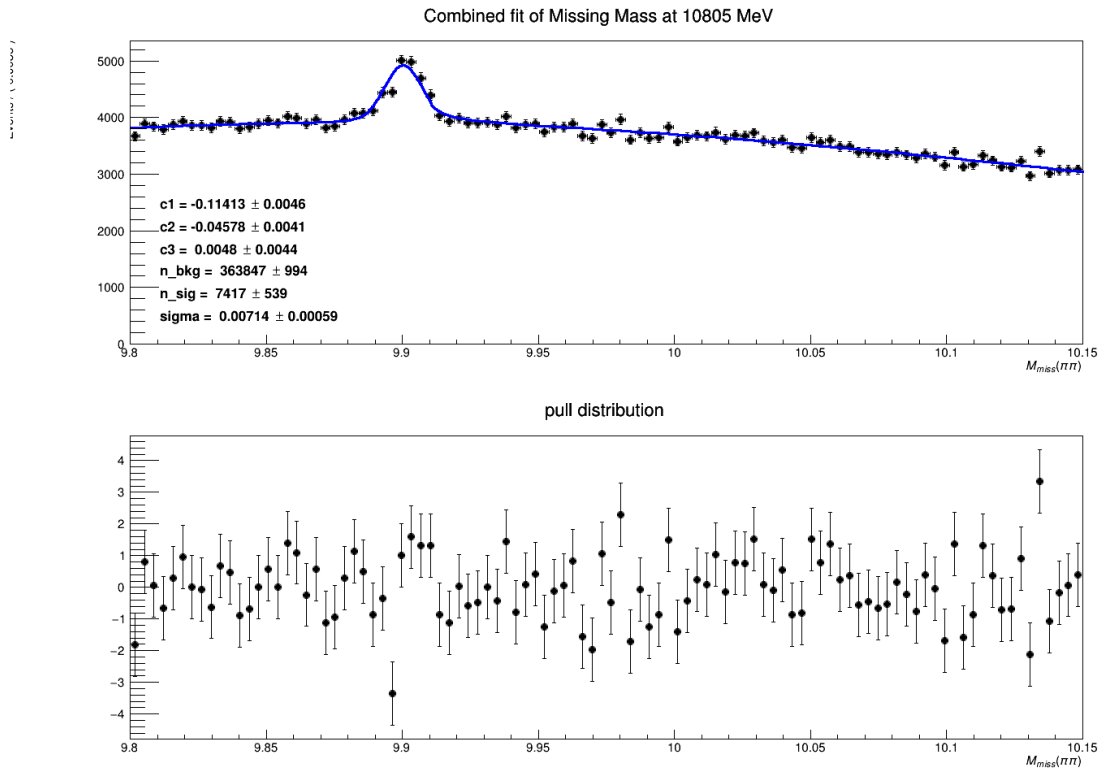
(a) $\chi^2/DoF = 0.97$ (b) $\chi^2/DoF = 1.05$

Figure 8.3: Results of the fits on the $M_{miss}(\pi\pi)$ (GeV/c^2) in the signal region for combined signal and background events, for the 10657 MeV (a) and 10706 MeV (b) energy points, after applying CS and track selection cuts and weighting the events to account for efficiency of reconstruction and tracks selection. Points with error bars are the MC events, blue line represents the fit function.



(a) $\chi^2/DoF = 1.01$



(b) $\chi^2/DoF = 1.14$

Figure 8.4: Results of the fits on the $M_{miss}(\pi\pi)$ (GeV/c^2) in the signal region for combined signal and background events, for the 10745 MeV (a) and 10805 MeV (b) energy points, after applying CS and track selection cuts and weighting the events to account for efficiency of reconstruction and tracks selection. Points with error bars are the MC events, blue line represents the fit function.

All the fits in this section were performed using the ROOT package on Python3.

Chapter 9

Conclusion

Heavy quark spectroscopy is a promising field to study the QCD interaction in a controlled environment. While the spectrum of conventional quarkonium states $Q\bar{Q}$ provides an experimental playground to validate theoretical and phenomenological predictions, the large number of exotic states discovered in the past years casts light on different interesting as well as challenging aspects of the QCD interaction in the $Q\bar{Q}$ system. The discovery of the $Y(10753)$ resonance in the $e^+e^- \rightarrow \pi\pi\Upsilon(nS)$ cross section adds another piece to the puzzle of the exotic states. With the 20fb^{-1} luminosity of data acquired by Belle II at 10657, 10706, 10745 and 10805 MeV around the $Y(10753)$, it will be possible to explore different decay modes of this state, in order to understand its nature.

In this thesis the search of $e^+e^- \rightarrow \pi\pi h_b(1P)$ with the Belle II data taken around the $Y(10751)$ was approached. This process is interesting since the HQSS should largely suppress the dipion transition from a triplet to a singlet of spin state, however the presence of the intermediate charged state $Z_b(10610)$ could lead to a larger cross section than expected, in similar fashion with what has been observed for the $Y(5S) \rightarrow \pi\pi h_b(mP)$ ($m = 1, 2$) decay.

In this analysis the $h_b(1P)$ were reconstructed inclusively on MC samples with the phase space transition $e^+e^- \rightarrow \pi\pi h_b(1P)$ for all the four energy of the scan, and the $Z_b(10610)$ mediated transition $e^+e^- \rightarrow \pi Z_b(10610) \rightarrow \pi\pi h_b(1P)$ for only the point at 10805 MeV, since is the only one in which this transition is kinematically allowed.

The kinematics of the pions and the distribution of the dipion recoil mass for the phase space transition and the Z_b mediated transition were studied, and the phase space transition was chosen as the only channel to simulate the signal in this analysis, since the Z_b transition present a drastically different kinematics for the two pions and the reconstruction would be compromised by a lower acceptance. Selection of the tracks was performed with a sample of MC events from the several processes that could affect the background in this analysis.

Efficiency of the tracks selection was validated using the two control channels $D^{*+} \rightarrow \pi D_0 \rightarrow \pi K\pi$ and $D^{*+} \rightarrow \pi D_0 \rightarrow \pi K\pi\pi_0$. The validation study led to an estimation of the ratio R between the efficiency in data and in MC; values for R were obtained in bins of p_t of the track, thus allowing to interpolate them to obtain a function $R(p_t)$, that will be used to correct data-simulation discrepancy for the track selection when the fit on data point will be performed. To correct for reconstruction and track selection cuts, efficiency in bins of p_t and $\cos\theta$ was measured on the generic MC. Values of efficiency were interpolated to get a 2D function of p_t and $\cos\theta$ of the tracks. This function is used to compute the weights

in order to correct for the track selection cuts and reconstruction effects on the single tracks. The effect of the weighting on the signal yield was inspected and after the weighting of the tracks, a small underestimation of the signal yield of the order of few points percentage was found for all the energies. The events kinematics was also studied and cuts on the visible energy and on the number of good tracks were performed in order to eliminate the contribution of $e^+e^- \rightarrow$ (*many hadrons*) events. Suppression of continuum, i.e. $e^+e^- \rightarrow q\bar{q}$ events, was performed using a SGBDT already trained for the $e^+e^- \rightarrow \eta h_b(1P)$ analysis with the FastBDT implementation. The performance of the BDT was checked for the signal, and the cut for the BDT classifier output was optimized using a figure of merit.

The fitting strategy was addressed and the signal region was identified, alongside the functions that will be used to parameterize signal and background in data, once the analysis will be unblinded by the Belle II analysis referees.

Bibliography

- [1] N. Brambilla et al.. “Heavy quarkonium: progress, puzzles, and opportunities”. In: *The European Physical Journal C* 71.2 (Feb. 2011). DOI: 10.1140/epjc/s10052-010-1534-9. URL: <https://doi.org/10.1140%2Fepjc%2Fs10052-010-1534-9>.
- [2] E Kou and P et almannshofer et others Urquijo. “The Belle II Physics Book”. In: *Progress of Theoretical and Experimental Physics* 2019.12 (Dec. 2019). 123C01. ISSN: 2050-3911. DOI: 10.1093/ptep/ptz106. eprint: <https://academic.oup.com/ptep/article-pdf/2019/12/123C01/32693980/ptz106.pdf>. URL: <https://doi.org/10.1093/ptep/ptz106>.
- [3] Choi et al.. “Observation of a Narrow Charmoniumlike State in Exclusive $B^\pm \rightarrow K^\pm \pi^+ \pi^- J/\psi$ Decays”. In: *Phys. Rev. Lett.* 91 (26 Dec. 2003), p. 262001. DOI: 10.1103/PhysRevLett.91.262001. URL: <https://link.aps.org/doi/10.1103/PhysRevLett.91.262001>.
- [4] Ablikim et al.. “Study of $e^+e^- \rightarrow \gamma\omega J/\psi$ and Observation of $X(3872) \rightarrow \omega J/\psi$ ”. In: *Phys. Rev. Lett.* 122 (23 June 2019), p. 232002. DOI: 10.1103/PhysRevLett.122.232002. URL: <https://link.aps.org/doi/10.1103/PhysRevLett.122.232002>.
- [5] Bhardwaj et al.. “Observation of $X(3872) \rightarrow J/\psi\gamma$ and Search for $X(3872) \rightarrow \psi'\gamma$ in B Decays”. In: *Phys. Rev. Lett.* 107 (9 Aug. 2011), p. 091803. DOI: 10.1103/PhysRevLett.107.091803. URL: <https://link.aps.org/doi/10.1103/PhysRevLett.107.091803>.
- [6] Aaij et al.. “Evidence for the decay $X(3872) \rightarrow \psi(2S)\gamma$ ”. In: *Nuclear Physics B* 886.1 (2014). Cited by: 116; All Open Access, Gold Open Access, Green Open Access, 665 – 680. DOI: 10.1016/j.nuclphysb.2014.06.011. URL: <https://www.scopus.com/inward/record.uri?eid=2-s2.0-84983573910&doi=10.1016%2Fj.nuclphysb.2014.06.011&partnerID=40&md5=7e0625ee8f2d87009107a07615cfbc62>.
- [7] Aubert et al.. “Evidence for $X(3872) \rightarrow \psi(2S)\gamma$ in $B^\pm \rightarrow X(3872)K^\pm$ Decays and a Study of $B \rightarrow c\bar{c}\gamma K$ ”. In: *Phys. Rev. Lett.* 102 (13 Mar. 2009), p. 132001. DOI: 10.1103/PhysRevLett.102.132001. URL: <https://link.aps.org/doi/10.1103/PhysRevLett.102.132001>.
- [8] M. N. Achasov et al. “Study of the $\pi^+\pi^-\pi^0$ mass spectra in the process $e^+e^- \rightarrow \pi^+\pi^-\pi^0$ at $s^{*}(1/2) = 1020\text{-MeV}$ ”. In: *Phys. Rev. D* 65 (2002), p. 032002. DOI: 10.1103/PhysRevD.65.032002. arXiv: hep-ex/0106048.
- [9] Jia-Feng Liu and Gui-Jun Ding. “Bottomonium Spectrum with Coupled-Channel Effects”. In: *Eur. Phys. J. C* 72 (2012), p. 1981. DOI: 10.1140/epjc/s10052-012-1981-6. arXiv: 1105.0855 [hep-ph].

- [10] L. Micu. “Decay rates of meson resonances in a quark model”. In: *Nuclear Physics B* 10.3 (1969), pp. 521–526. ISSN: 0550-3213. DOI: [https://doi.org/10.1016/0550-3213\(69\)90039-X](https://doi.org/10.1016/0550-3213(69)90039-X). URL: <https://www.sciencedirect.com/science/article/pii/055032136990039X>.
- [11] Yu. S. Kalashnikova. “Coupled-channel model for charmonium levels and an option for $X(3872)$ ”. In: *Phys. Rev. D* 72 (3 2005), p. 034010. DOI: 10.1103/PhysRevD.72.034010. URL: <https://link.aps.org/doi/10.1103/PhysRevD.72.034010>.
- [12] K. Abe et al. “Observation of Double $c\bar{c}$ Production in e^+e^- Annihilation at $\sqrt{s} \approx 10.6$ GeV”. In: *Phys. Rev. Lett.* 89 (14 July 2002), p. 142001. DOI: 10.1103/PhysRevLett.89.142001. URL: <https://link.aps.org/doi/10.1103/PhysRevLett.89.142001>.
- [13] B. Martín-González et al. “Toward the discovery of novel B_c states: Radiative and hadronic transitions”. In: *Phys. Rev. D* 106 (5 2022), p. 054009. DOI: 10.1103/PhysRevD.106.054009. URL: <https://link.aps.org/doi/10.1103/PhysRevD.106.054009>.
- [14] N. Brambilla et al.. “QCD and strongly coupled gauge theories: challenges and perspectives”. In: *The European Physical Journal C* 74.10 (Sept. 2014). DOI: 10.1140/epjc/s10052-014-2981-5. URL: <https://doi.org/10.1140/epjc/s10052-014-2981-5>.
- [15] Geoffrey T. Bodwin. *Theory of Charmonium Production*. 2013. arXiv: 1208.5506 [hep-ph].
- [16] T. Barnes, F. E. Close, and E. S. Swanson. “Hybrid and conventional mesons in the flux tube model: Numerical studies and their phenomenological implications”. In: *Physical Review D* 52.9 (Nov. 1995), pp. 5242–5256. DOI: 10.1103/physrevd.52.5242. URL: <https://doi.org/10.1103/physrevd.52.5242>.
- [17] Colin J. Morningstar and Mike Peardon. “Glueball spectrum from an anisotropic lattice study”. In: *Physical Review D* 60.3 (July 1999). DOI: 10.1103/physrevd.60.034509. URL: <https://doi.org/10.1103/physrevd.60.034509>.
- [18] Adachi et al.. “First Observation of the P -Wave Spin-Singlet Bottomonium States $h_b(1P)$ and $h_b(2P)$ ”. In: *Phys. Rev. Lett.* 108 (3 2012), p. 032001. DOI: 10.1103/PhysRevLett.108.032001. URL: <https://link.aps.org/doi/10.1103/PhysRevLett.108.032001>.
- [19] Matthias Neubert. *Heavy-Quark Effective Theory*. 1996. arXiv: hep-ph/9610266 [hep-ph].
- [20] Bondar et al. “Observation of Two Charged Bottomoniumlike Resonances in $\Upsilon(5S)$ Decays”. In: *Phys. Rev. Lett.* 108 (12 2012), p. 122001. DOI: 10.1103/PhysRevLett.108.122001. URL: <https://link.aps.org/doi/10.1103/PhysRevLett.108.122001>.

- [21] Ablikim et al.. “Observation of a Charged Charmoniumlike Structure in $e^+e^- \rightarrow \pi^+\pi^-J/\psi$ at $\sqrt{s}=4.26$ GeV”. In: *Phys. Rev. Lett.* 110 (25 June 2013), p. 252001. DOI: 10.1103/PhysRevLett.110.252001. URL: <https://link.aps.org/doi/10.1103/PhysRevLett.110.252001>.
- [22] Liu et al.. “Study of $e^+e^- \rightarrow \pi^+\pi^-J/\psi$ and Observation of a Charged Charmoniumlike State at Belle”. In: *Phys. Rev. Lett.* 110 (25 July 2013), p. 252002. DOI: 10.1103/PhysRevLett.110.252002. URL: <https://link.aps.org/doi/10.1103/PhysRevLett.110.252002>.
- [23] Ablikim et al. “Observation of a Charged Charmoniumlike Structure $Z_c(4020)$ and Search for the $Z_c(3900)$ in $e^+e^- \rightarrow \pi^+\pi^-h_c$ ”. In: *Phys. Rev. Lett.* 111 (24 2013), p. 242001. DOI: 10.1103/PhysRevLett.111.242001. URL: <https://link.aps.org/doi/10.1103/PhysRevLett.111.242001>.
- [24] Ablikim et al.. “Observation of $Z_c(3900)^0$ in $e^+e^- \rightarrow \pi^0\pi^0J/\psi$ ”. In: *Phys. Rev. Lett.* 115 (11 2015), p. 112003. DOI: 10.1103/PhysRevLett.115.112003. URL: <https://link.aps.org/doi/10.1103/PhysRevLett.115.112003>.
- [25] Ablikim et al.. “Observation of $e^+e^- \rightarrow \pi^0\pi^0h_c$ and a Neutral Charmoniumlike Structure $Z_c(4020)^0$ ”. In: *Phys. Rev. Lett.* 113 (21 Nov. 2014), p. 212002. DOI: 10.1103/PhysRevLett.113.212002. URL: <https://link.aps.org/doi/10.1103/PhysRevLett.113.212002>.
- [26] Krokovny et al.. “First observation of the $Z_b^0(10610)$ in a Dalitz analysis of $\Upsilon(10860) \rightarrow \Upsilon(nS)\pi^0\pi^0$ ”. In: *Phys. Rev. D* 88 (5 Sept. 2013), p. 052016. DOI: 10.1103/PhysRevD.88.052016. URL: <https://link.aps.org/doi/10.1103/PhysRevD.88.052016>.
- [27] A. E. Bondar et al. “Heavy quark spin structure in Z_b resonances”. In: *Phys. Rev. D* 84 (5 Sept. 2011), p. 054010. DOI: 10.1103/PhysRevD.84.054010. URL: <https://link.aps.org/doi/10.1103/PhysRevD.84.054010>.
- [28] Qian Wang, Christoph Hanhart, and Qiang Zhao. “Decoding the Riddle of $Y(4260)$ and $Z_c(3900)$ ”. In: *Phys. Rev. Lett.* 111 (13 2013), p. 132003. DOI: 10.1103/PhysRevLett.111.132003. URL: <https://link.aps.org/doi/10.1103/PhysRevLett.111.132003>.
- [29] R. Mizuk et al.. In: *Journal of High Energy Physics* 2019.10 (Oct. 2019). DOI: 10.1007/jhep10(2019)220. URL: [https://doi.org/10.1007/JHEP10\(2019\)220](https://doi.org/10.1007/JHEP10(2019)220).
- [30] Xiang-Kun Dong et al. In: *Chinese Physics C* 44.8 (Aug. 2020), p. 083001. DOI: 10.1088/1674-1137/44/8/083001. URL: <https://doi.org/10.1088/1674-1137/44/8/083001>.
- [31] Aubert et al.. “Observation of a Broad Structure in the $\pi^+\pi^-J/\psi$ Mass Spectrum around 4.26 GeV/ c^2 ”. In: *Phys. Rev. Lett.* 95 (14 2005), p. 142001. DOI: 10.1103/PhysRevLett.95.142001. URL: <https://link.aps.org/doi/10.1103/PhysRevLett.95.142001>.

- [32] Particle Data Group et al. “Review of Particle Physics”. In: *Progress of Theoretical and Experimental Physics* 2020.8 (Aug. 2020). 083C01. ISSN: 2050-3911. DOI: 10.1093/ptep/ptaa104. eprint: https://academic.oup.com/ptep/article-pdf/2020/8/083C01/34673740/rpp2020-vol12-2015-2092_18.pdf. URL: <https://doi.org/10.1093/ptep/ptaa104>.
- [33] Zi-Yue Bai et al. In: *Physical Review D* 105.7 (Apr. 2022). DOI: 10.1103/physrevd.105.074007. URL: <https://doi.org/10.1103/PhysRevD.105.074007>.
- [34] Ahmed Ali et al. “Interpretation of $Y_b(10753)$ as a tetraquark and its production mechanism”. In: *Phys. Lett. B* 802 (2020), p. 135217. DOI: 10.1016/j.physletb.2020.135217. arXiv: 1910.07671 [hep-ph].
- [35] Bing Chen, Ailin Zhang, and Jin He. “Bottomonium spectrum in the relativistic flux tube model”. In: *Phys. Rev. D* 101 (1 2020), p. 014020. DOI: 10.1103/PhysRevD.101.014020. URL: <https://link.aps.org/doi/10.1103/PhysRevD.101.014020>.
- [36] Jesse F. Giron and Richard F. Lebed. “Spectrum of the hidden-bottom and the hidden-charm-strange exotics in the dynamical diquark model”. In: *Phys. Rev. D* 102 (1 2020), p. 014036. DOI: 10.1103/PhysRevD.102.014036. URL: <https://link.aps.org/doi/10.1103/PhysRevD.102.014036>.
- [37] Qi Li et al. “Canonical interpretation of $Y(10750)$ and $\Upsilon(10860)$ in the Υ family”. In: *The European Physical Journal C* 80.1 (Jan. 2020). DOI: 10.1140/epjc/s10052-020-7626-2. URL: <https://doi.org/10.1140/epjc/s10052-020-7626-2>.
- [38] W.-H. Liang et al. “ $\Upsilon(nL)$ decay into $B^{(*)}\overline{B^{(*)}}$ ”. In: *Physics Letters B* 803 (Feb. 2020), p. 135340. DOI: 10.1016/j.physletb.2020.135340.
- [39] C. Alexandrou et al. “Nucleon axial and pseudoscalar form factors from lattice QCD at the physical point”. In: *Phys. Rev. D* 103 (3 Feb. 2021), p. 034509. DOI: 10.1103/PhysRevD.103.034509. URL: <https://link.aps.org/doi/10.1103/PhysRevD.103.034509>.
- [40] Yu-Shuai Li et al. “Hidden-bottom hadronic decays of $\Upsilon(10753)$ with a $\eta^{(\prime)}$ or ω emission”. In: *Phys. Rev. D* 104 (3 2021), p. 034036. DOI: 10.1103/PhysRevD.104.034036. URL: <https://link.aps.org/doi/10.1103/PhysRevD.104.034036>.
- [41] Kazunori Akai, Kazuro Furukawa, and Haruyo Koiso. “SuperKEKB Collider”. In: *Nucl. Instrum. Meth. A* 907 (2018), pp. 188–199. DOI: 10.1016/j.nima.2018.08.017. arXiv: 1809.01958 [physics.acc-ph].
- [42] Kazunori Akai. “SuperKEKB status—Belle II physics run started”. In: *PoS ICHEP2018* (2019), p. 701. DOI: 10.22323/1.340.0701.
- [43] T. Abe et al. “Belle II Technical Design Report”. In: (Nov. 2010). arXiv: 1011.0352 [physics.ins-det].

- [44] H. Ye et al.. “Commissioning and performance of the Belle II pixel detector”. In: *Nuclear Instruments and Methods in Physics Research Section A: Accelerators, Spectrometers, Detectors and Associated Equipment* 987 (2021), p. 164875. ISSN: 0168-9002. DOI: <https://doi.org/10.1016/j.nima.2020.164875>. URL: <https://www.sciencedirect.com/science/article/pii/S0168900220312729>.
- [45] L. Zani et al.. “The Silicon Vertex Detector of the Belle II experiment”. In: *Nuclear Instruments and Methods in Physics Research Section A: Accelerators, Spectrometers, Detectors and Associated Equipment* 1038 (2022), p. 166952. ISSN: 0168-9002. DOI: <https://doi.org/10.1016/j.nima.2022.166952>. URL: <https://www.sciencedirect.com/science/article/pii/S0168900222003977>.
- [46] N. Taniguchi. “Central Drift Chamber for Belle-II”. In: *Journal of Instrumentation* 12.06 (2017), p. C06014. DOI: 10.1088/1748-0221/12/06/C06014. URL: <https://dx.doi.org/10.1088/1748-0221/12/06/C06014>.
- [47] Yosuke Yusa. “The ARICH detector at Belle II experiment”. In: *PoS EPS-HEP2013* (2013), p. 556. DOI: 10.22323/1.180.0556.
- [48] Yasuyuki Horii. “TOP Detector for Particle Identification at the Belle II Experiment”. In: *PoS EPS-HEP2013* (2013), p. 500. DOI: 10.22323/1.180.0500.
- [49] A. Kuzmin. “Electromagnetic calorimeter of Belle II”. In: *Nuclear Instruments and Methods in Physics Research Section A: Accelerators, Spectrometers, Detectors and Associated Equipment* 958 (2020). Proceedings of the Vienna Conference on Instrumentation 2019, p. 162235. ISSN: 0168-9002. DOI: <https://doi.org/10.1016/j.nima.2019.05.076>. URL: <https://www.sciencedirect.com/science/article/pii/S0168900219307405>.
- [50] Leo Piilonen and II Belle Collaboration. “The upgraded KLM detector at Belle II”. In: *APS April Meeting Abstracts*. Vol. 2016. APS Meeting Abstracts. Mar. 2016, R17.007, R17.007.
- [51] T. Kuhr et al. “The Belle II Core Software”. In: *Computing and Software for Big Science* 3.1 (Nov. 2018). DOI: 10.1007/s41781-018-0017-9. URL: <https://doi.org/10.1007/s41781-018-0017-9>.
- [52] S. Agostinelli et al.. “Geant4—a simulation toolkit”. In: *Nuclear Instruments and Methods in Physics Research Section A: Accelerators, Spectrometers, Detectors and Associated Equipment* 506.3 (2003), pp. 250–303. ISSN: 0168-9002. DOI: [https://doi.org/10.1016/S0168-9002\(03\)01368-8](https://doi.org/10.1016/S0168-9002(03)01368-8). URL: <https://www.sciencedirect.com/science/article/pii/S0168900203013688>.
- [53] Valerio Bertacchi et al.. “Track finding at Belle II”. In: *Computer Physics Communications* 259 (2021), p. 107610. ISSN: 0010-4655. DOI: <https://doi.org/10.1016/j.cpc.2020.107610>. URL: <https://www.sciencedirect.com/science/article/pii/S0010465520302861>.
- [54] Tadeas Bilka et al. *Implementation of GENFIT2 as an experiment independent track-fitting framework*. 2019. arXiv: 1902.04405 [physics.data-an].

-
- [55] Jonas Eschle et al. “zfit: Scalable pythonic fitting”. In: *SoftwareX* 11 (Jan. 2020), p. 100508. DOI: 10.1016/j.softx.2020.100508. URL: <https://doi.org/10.1016%2Fj.softx.2020.100508>.
- [56] Virtanen et al. “SciPy 1.0: Fundamental Algorithms for Scientific Computing in Python”. In: *Nature Methods* 17 (2020), pp. 261–272. DOI: 10.1038/s41592-019-0686-2.
- [57] Thomas Keck. *FastBDT: A speed-optimized and cache-friendly implementation of stochastic gradient-boosted decision trees for multivariate classification*. 2016. arXiv: 1609.06119 [cs.LG].
- [58] Garmash et al. “Amplitude analysis of $e^+e^- \rightarrow \Upsilon(nS)\pi^+\pi^-$ at $\sqrt{s} = 10.866$ GeV”. In: *Phys. Rev. D* 91 (7 2015), p. 072003. DOI: 10.1103/PhysRevD.91.072003. URL: <https://link.aps.org/doi/10.1103/PhysRevD.91.072003>.

Appendix A

Results of the simultaneous fits for the $D_0 \rightarrow K^- \pi^+ \pi^0$ channel

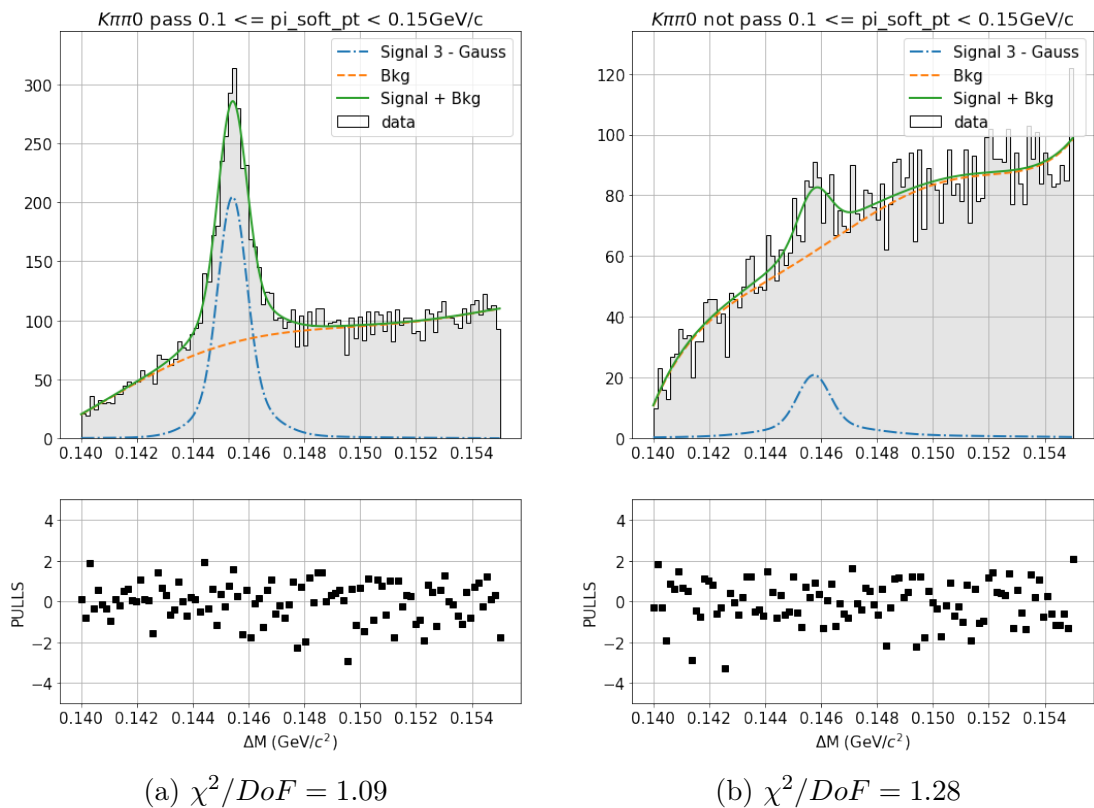


Figure A.1: Distribution of ΔM for data events that pass (a) and do not pass (b) the track selection cuts. grey histogram represents the data points, green solid line is the combined fit function, blue dotted line is the signal fit function, orange dotted line is the background fit function. Corresponding interval of p_t is shown above the plot.

valid	converged	param at limit	edm	min value
True	True	False	0.00025	-2880.766

```

Parameters
name          value (rounded)      hesse      at limit
-----
eff           0.866676 +/- 0.031      False
yield_sig    2502.24 +/- 1.2e+02     False
yieldCheb_pass 8071.64 +/- 1.1e+02     False
delta_mu_pass -1.33233e-05 +/- 2.2e-05 False
sigma_conv_pass -1.03984e-06 +/- 9.6e-05 False
a            0.530587 +/- 0.022      False
b            -0.163665 +/- 0.024     False
c            0.0662835 +/- 0.021     False
d            0.0131587 +/- 0.02      False
e            -0.0115423 +/- 0.021    False
yieldCheb_not_pass 6643.12 +/- 1.2e+02     False
delta_mu_not_pass 0.000305781 +/- 0.00015 False
sigma_conv_not_pass -4.49497e-06 +/- 0.00038 False
ka           0.610295 +/- 0.024     False
ki           -0.137475 +/- 0.027     False
ku           0.0414795 +/- 0.023     False
ke           -0.00475626 +/- 0.022   False
ko           0.0399976 +/- 0.022     False
*****

```

Figure A.2: Parameters of function from the simultaneous fit in the $(0.1 \leq p_t < 0.15 \text{ GeV}/c)$ bin. Functions have their parameters labelled as "pass" or "not pass" depending the data the function describes, [a, b, c, d, e] are the parameters of the "pass background function"; [ka, ki, ku, ke, ko] are the parameters of the "not pass" background function.

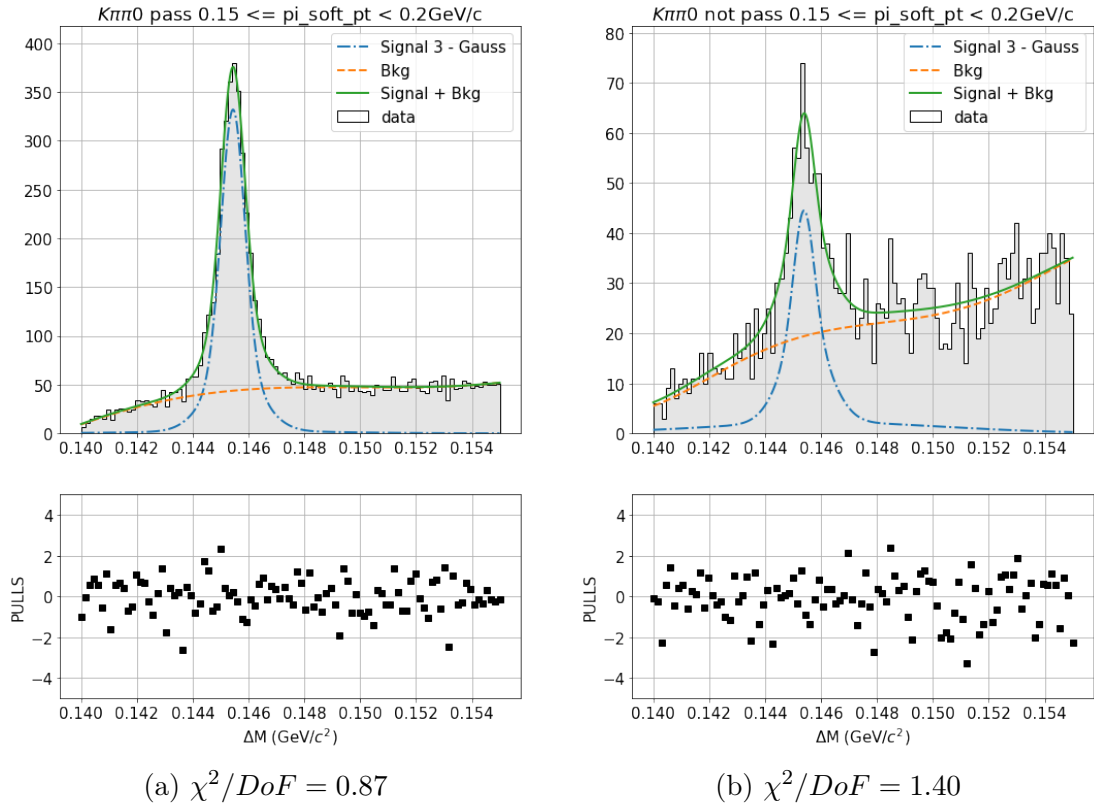


Figure A.3: Distribution of ΔM for data events that pass (a) and do not pass (b) the track selection cuts. grey histogram represents the data points, green solid line is the combined fit function, blue dotted line is the signal fit function, orange dotted line is the background fit function. Corresponding interval of p_t is shown above the plot.

valid	converged	param at limit	edm	min value
True	True	False	0.00074	-554.0961

Parameters name	value (rounded)	hesse	at limit
eff	0.847958	+/- 0.015	False
yield sig	3480.58	+/- 1e+02	False
yieldCheb_pass	4107.05	+/- 91	False
delta_mu_pass	5.93204e-06	+/- 1.3e-05	False
sigma_conv_pass	-0.00013565	+/- 4.4e-05	False
a	0.458268	+/- 0.033	False
b	-0.213823	+/- 0.036	False
c	0.103391	+/- 0.03	False
d	0.0105498	+/- 0.028	False
e	-0.00399064	+/- 0.033	False
yieldCheb_not_pass	2074.39	+/- 71	False
delta_mu_not_pass	-4.07751e-05	+/- 5.3e-05	False
sigma_conv_not_pass	-0.00016649	+/- 0.00013	False
ka	0.649491	+/- 0.049	False
ki	-0.0360424	+/- 0.051	False
ku	0.0892386	+/- 0.044	False
ke	0.0181348	+/- 0.039	False
ko	-0.0234464	+/- 0.044	False

Figure A.4: Parameters of function from the simultaneous fit in the $(0.15 \leq p_t < 0.2 \text{ GeV}/c)$ bin. Functions have their parameters labelled as "pass" or "not pass" depending the data the function describes, [a, b, c, d, e] are the parameters of the "pass background function"; [ka, ki, ku, ke, ko] are the parameters of the "not pass" background function.

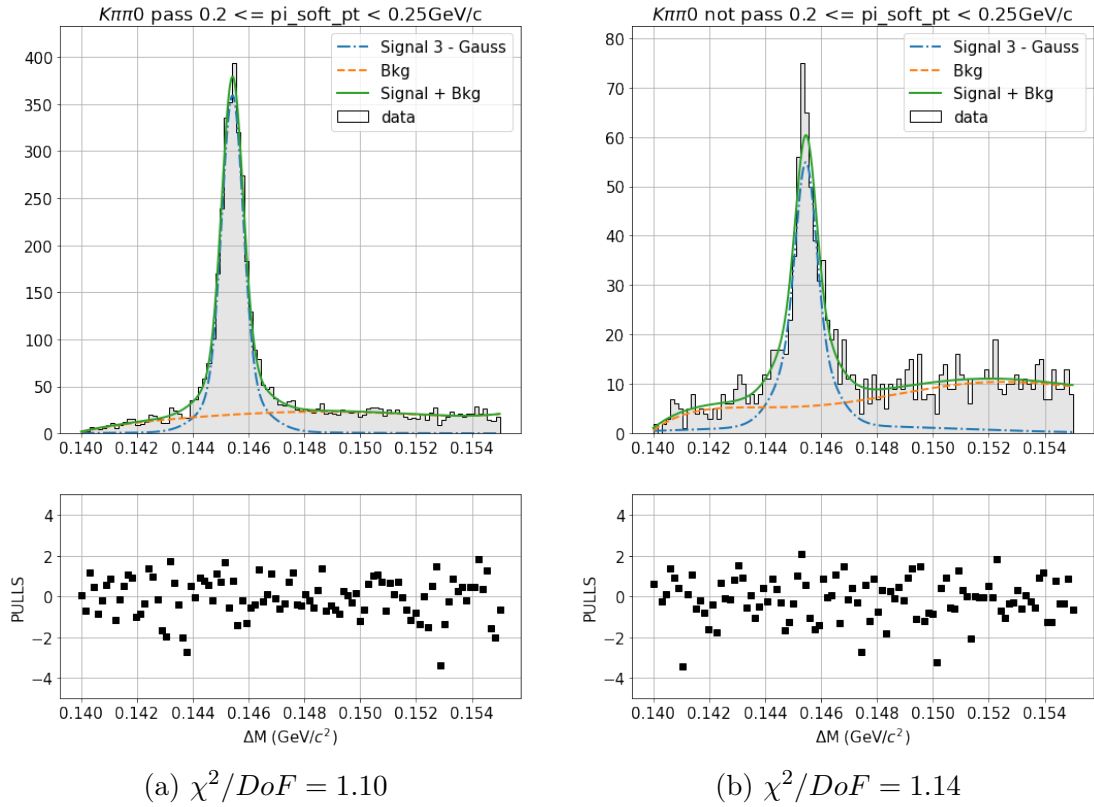


Figure A.5: Distribution of ΔM for data events that pass (a) and do not pass (b) the track selection cuts. grey histogram represents the data points, green solid line is the combined fit function, blue dotted line is the signal fit function, orange dotted line is the background fit function. Corresponding interval of p_t is shown above the plot.

valid	converged	param at limit	edm	min value
True	True	False	0.00074	-554.0961

```

Parameters
name          value (rounded)      hesse      at limit
-----
eff           0.847958 +/- 0.015    False
yield sig    3480.58 +/- 1e+02     False
yieldCheb_pass 4107.05 +/- 91        False
delta_mu_pass 5.93204e-06 +/- 1.3e-05 False
sigma_conv_pass -0.00013565 +/- 4.4e-05 False
a             0.458268 +/- 0.033    False
b            -0.213823 +/- 0.036    False
c             0.103391 +/- 0.03      False
d             0.0105498 +/- 0.028   False
e            -0.00399064 +/- 0.033  False
yieldCheb_not_pass 2074.39 +/- 71        False
delta_mu_not_pass -4.07751e-05 +/- 5.3e-05 False
sigma_conv_not_pass -0.00016649 +/- 0.00013 False
ka           0.649491 +/- 0.049    False
ki          -0.0360424 +/- 0.051   False
ku           0.0892386 +/- 0.044    False
ke           0.0181348 +/- 0.039    False
ko          -0.0234464 +/- 0.044    False
*****

```

Figure A.6: Parameters of function from the simultaneous fit in the $(0.2 \leq p_t < 0.25 \text{ GeV}/c)$ bin. Functions have their parameters labelled as "pass" or "not pass" depending the data the function describes, [a, b, c, d, e] are the parameters of the "pass background function"; [ka, ki, ku, ke, ko] are the parameters of the "not pass" background function.

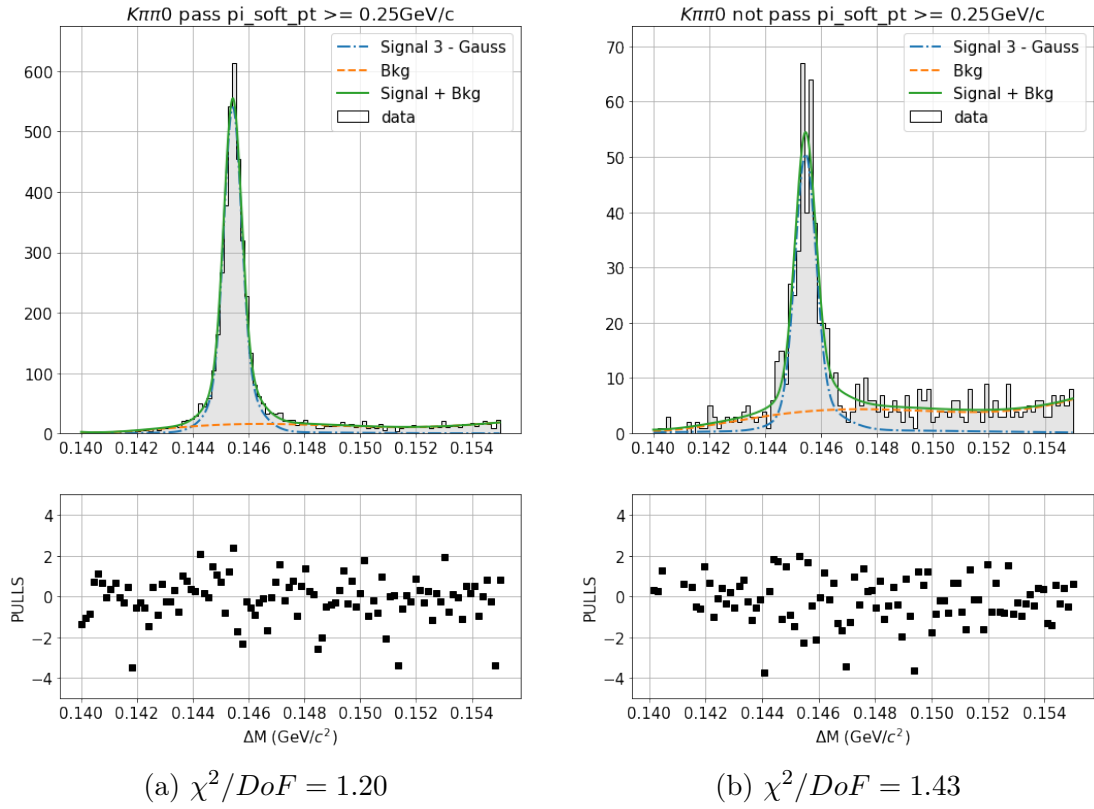


Figure A.7: Distribution of ΔM for data events that pass (a) and do not pass (b) the track selection cuts. grey histogram represents the data points, green solid line is the combined fit function, blue dotted line is the signal fit function, orange dotted line is the background fit function. Corresponding interval of p_t is shown above the plot.

valid	converged	param at limit	edm	min value
True	True	False	7.1e-05	-7969.328

```

Parameters
name          value (rounded)      hesse      at limit
-----
eff           0.899222 +/- 0.0013      False
yield sig    3884.72 +/- 27           False
yieldCheb_pass 1115.01 +/- 36          False
delta_mu_pass -2.42761e-06 +/- 6.4e-06 False
sigma_conv_pass 0 +/- 4e-05             False
a             0.592229 +/- 0.0094      False
b            -0.239045 +/- 0.011       False
c             0.274053 +/- 0.011       False
d             0.20704 +/- 0.011        False
e            -0.10477 +/- 0.012       False
yieldCheb_not_pass 350.5 +/- 39           False
delta_mu_not_pass 2.62611e-05 +/- 1.1e-05 False
sigma_conv_not_pass 0 +/- 0.029            False
ka           0.687015 +/- 0.0087      False
ki           -0.157387 +/- 0.012      False
ku           0.18658 +/- 0.012       False
ke           0.143776 +/- 0.012      False
ko           -0.0313583 +/- 0.012    False
*****

```

Figure A.8: Parameters of function from the simultaneous fit in the ($p_t > 0.25\text{GeV}/c$) bin. Functions have their parameters labelled as "pass" or "not pass" depending the data the function describes, [a, b, c, d, e] are the parameters of the "pass background function"; [ka, ki, ku, ke, ko] are the parameters of the "not pass" background function.

Appendix B

Results of the simultaneous fits for the $D_0 \rightarrow K^- \pi^+$ channel

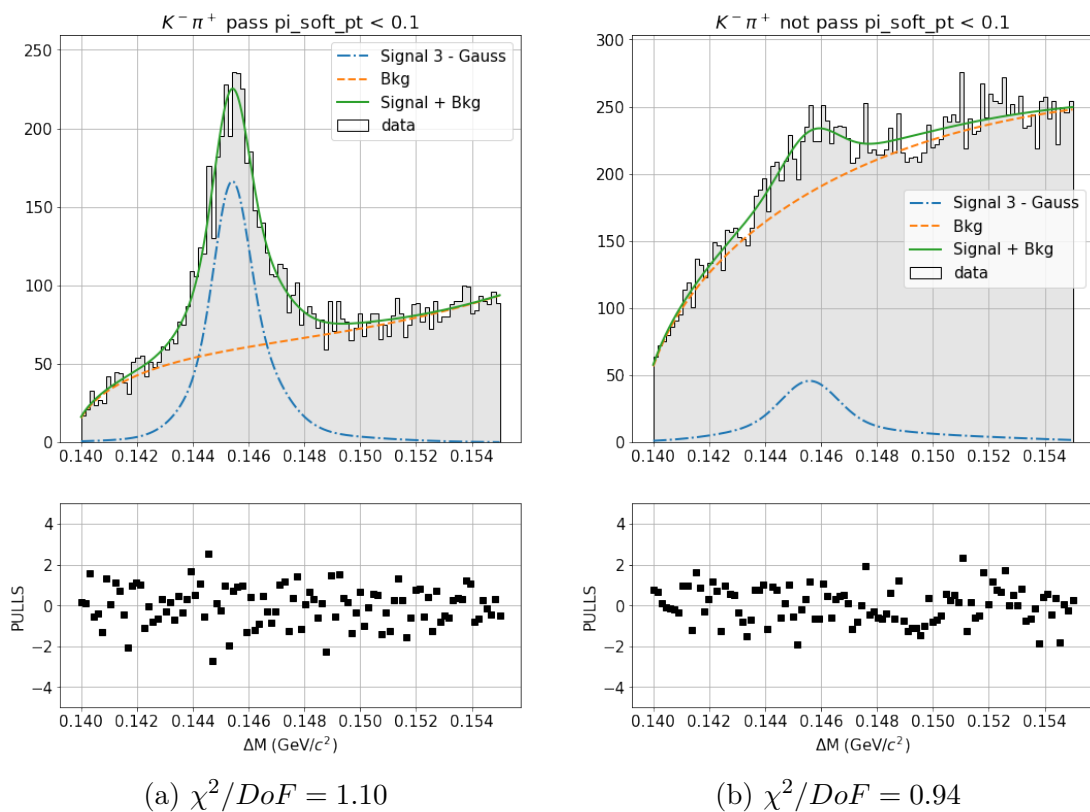


Figure B.1: Distribution of ΔM for data events that pass (a) and do not pass (b) the track selection cuts. grey histogram represents the data points, green solid line is the combined fit function, blue dotted line is the signal fit function, orange dotted line is the background fit function. Corresponding interval of p_t is shown above the plot.

valid	converged	param at limit	edm	min value
True	True	False	0.00011	1008.585

Parameters name	value (rounded)	hesse	at limit
eff	0.679719	+/- 0.045	False
yield_sig	3921.73	+/- 2.7e+02	False
background_yield_pass	6350.34	+/- 1.2e+02	False
delta_mu_pass	5.77535e-06	+/- 3.1e-05	False
sigma_conv_pass	-0.000153391	+/- 0.00015	False
a1_pass	0.0536209	+/- 0.0022	False
b1_pass	-0.644014	+/- 0.024	False
c1_pass	1.57134	+/- 0.11	False
d1_pass	2.49574	+/- 0.42	False
MIN_pass	0.139754	+/- 0.00015	False
background_yield_not_pass	19150.9	+/- 2.9e+02	False
delta_mu_not_pass	0.000140004	+/- 0.00017	False
sigma_conv_not_pass	-0.000396068	+/- 0.00046	False
a1_not_pass	0.541528	+/- 0.26	False
b1_not_pass	-2.3088	+/- 1.4	False
c1_not_pass	-2.84012	+/- 8.3	False
d1_not_pass	4.96351	+/- 3.9	False
MIN_not_pass	0.139534	+/- 0.00012	False

Figure B.2: Parameters of function from the simultaneous fit in the ($p_t < 0.1\text{GeV}/c$) bin. Functions have their parameters labelled as "pass" or "not pass" depending the data the function describes.

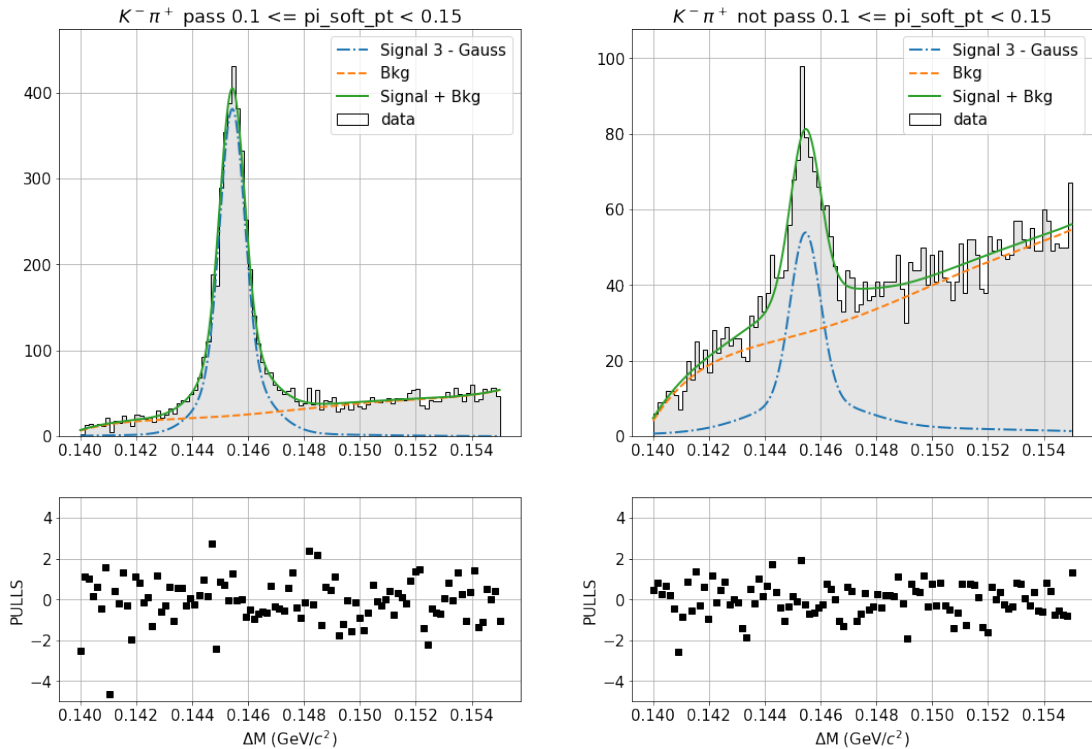


Figure B.3: Distribution of ΔM for data events that pass (a) and do not pass (b) the track selection cuts. grey histogram represents the data points, green solid line is the combined fit function, blue dotted line is the signal fit function, orange dotted line is the background fit function. Corresponding interval of p_t is shown above the plot.

valid	converged	param at limit	edm	min value
True	True	False	0.00086	-632.1028

```

Parameters
name          value (rounded)      hesse      at limit
-----
eff           0.820349 +/- 0.014      False
yield_sig    4516.53 +/- 1.1e+02     False
yieldCheb_pass 3084.23 +/- 80         False
delta_mu_pass -8.47192e-07 +/- 1.2e-05 False
sigma_conv_pass 2.19294e-06 +/- 7.5e-05 False
a             0.68877 +/- 0.038      False
b            -0.00110229 +/- 0.041   False
c             0.0316724 +/- 0.036    False
d            -0.015472 +/- 0.033    False
e             0.0478923 +/- 0.037    False
yieldCheb_not_pass 3300.39 +/- 90         False
delta_mu_not_pass 3.89212e-05 +/- 5.2e-05 False
sigma_conv_not_pass -1.40408e-06 +/- 0.00032 False
ka           0.703344 +/- 0.035     False
ki           -0.0437789 +/- 0.039   False
ku           0.0558316 +/- 0.034    False
ke           -0.0491288 +/- 0.032   False
ko           0.0209446 +/- 0.032    False
*****

```

Figure B.4: Parameters of function from the simultaneous fit in the $(0.1 \leq p_t < 0.15 \text{ GeV}/c)$ bin. Functions have their parameters labelled as "pass" or "not pass" depending the data the function describes, [a, b, c, d, e] are the parameters of the "pass background function"; [ka, ki, ku, ke, ko] are the parameters of the "not pass" background function.

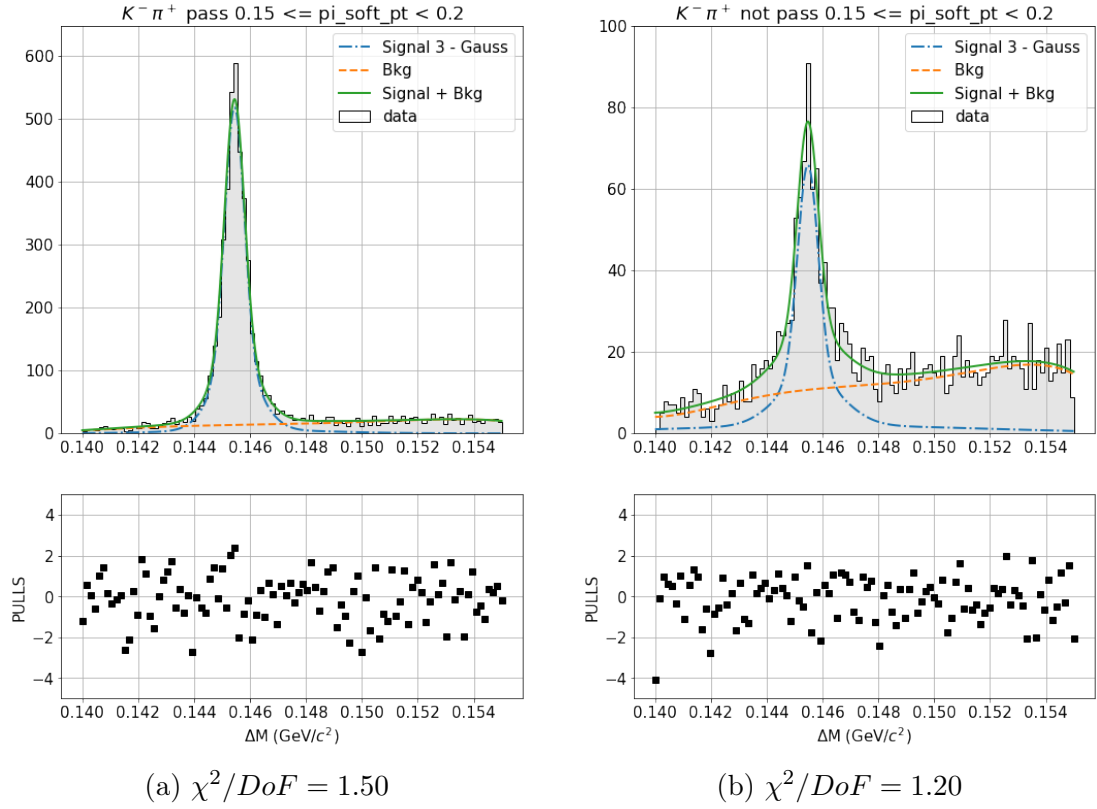


Figure B.5: Distribution of ΔM for data events that pass (a) and do not pass (b) the track selection cuts. grey histogram represents the data points, green solid line is the combined fit function, blue dotted line is the signal fit function, orange dotted line is the background fit function. Corresponding interval of p_t is shown above the plot.

valid	converged	param at limit	edm	min value
True	True	False	0.00011	138.6877

```

Parameters
name          value (rounded)      hesse      at limit
-----
eff           0.853262 +/- 0.0098   False
yield_sig    4692.91 +/- 92        False
yieldCheb_pass 1530.74 +/- 56        False
delta_mu_pass 1.99307e-05 +/- 8.4e-06 False
sigma_conv_pass -1.28678e-11 +/- 3.6e-05 False
a             0.564802 +/- 0.055    False
b            -0.097083 +/- 0.057    False
c            -0.0198204 +/- 0.052   False
d            -0.0718132 +/- 0.049   False
e            -0.0319466 +/- 0.055    False
yieldCheb_not_pass 1157.4 +/- 57        False
delta_mu_not_pass 3.77214e-05 +/- 3.2e-05 False
sigma_conv_not_pass -3.19441e-05 +/- 0.0004 False
ka           0.555042 +/- 0.071    False
ki           -0.113736 +/- 0.068    False
ku           -0.0240784 +/- 0.063   False
ke           -0.0482884 +/- 0.058   False
ko           -0.0575534 +/- 0.065   False
*****

```

Figure B.6: Parameters of function from the simultaneous fit in the $(0.15 \leq p_t < 0.2 \text{ GeV}/c)$ bin. Functions have their parameters labelled as "pass" or "not pass" depending the data the function describes, [a, b, c, d, e] are the parameters of the "pass background function"; [ka, ki, ku, ke, ko] are the parameters of the "not pass" background function.

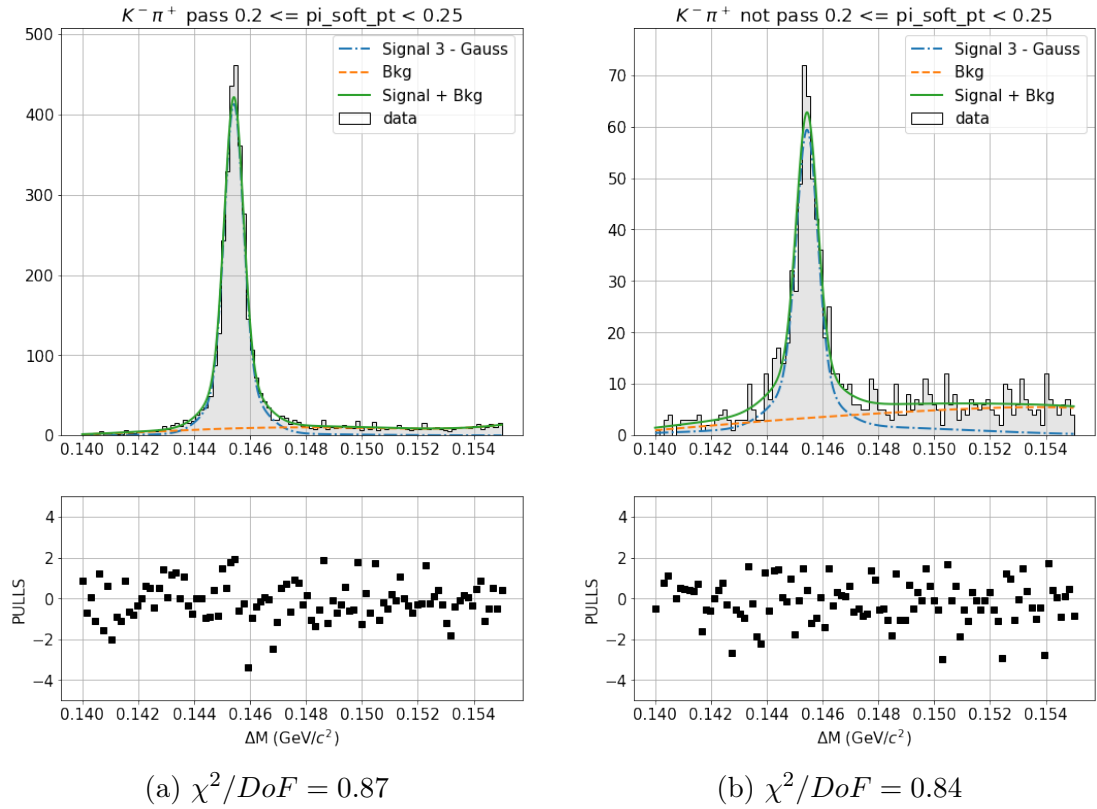


Figure B.7: Distribution of ΔM for data events that pass (a) and do not pass (b) the track selection cuts. grey histogram represents the data points, green solid line is the combined fit function, blue dotted line is the signal fit function, orange dotted line is the background fit function. Corresponding interval of p_t is shown above the plot.

valid	converged	param at limit	edm	min value
True	True	False	0.00024	703.5171

```

Parameters
name          value (rounded)      hesse      at limit
-----
eff           0.837222 +/- 0.0098   False
yield_sig    3509.49 +/- 73        False
yieldCheb_pass 790.81 +/- 41         False
delta_mu_pass 3.54606e-06 +/- 8.8e-06 False
sigma_conv_pass -4.40017e-11 +/- 2.7e-05 False
a             0.604993 +/- 0.071    False
b            -0.183977 +/- 0.083    False
c             0.177714 +/- 0.066    False
d             0.148509 +/- 0.063    False
e             0.0181963 +/- 0.072   False
yieldCheb_not_pass 384.746 +/- 37        False
delta_mu_not_pass 4.51756e-06 +/- 2.9e-05 False
sigma_conv_not_pass -2.60485e-05 +/- 0.00051 False
ka            0.622885 +/- 0.13     False
ki           -0.125112 +/- 0.13     False
ku           -0.0280749 +/- 0.12    False
ke           -0.0115513 +/- 0.11    False
ko           -0.00534313 +/- 0.12   False
*****

```

Figure B.8: Parameters of function from the simultaneous fit in the $(0.2 \leq p_t < 0.25 \text{ GeV}/c)$ bin. Functions have their parameters labelled as "pass" or "not pass" depending the data the function describes, [a, b, c, d, e] are the parameters of the "pass background function"; [ka, ki, ku, ke, ko] are the parameters of the "not pass" background function.